Doctoral Dissertation

博士論文

Quantitative evaluation of inhibitory potency of inhibitors for

Formyl Peptide Receptor 1 and elucidation of the inhibition

mechanism using fluorescence microscopy techniques

(FPR1 阻害剤の阻害能定量評価と蛍光顕微鏡法を用いた

阻害機序の解明)

Department of Chemistry, Graduate School of Science,

The University of Tokyo

東京大学大学院理学系研究科

化学専攻

Tomoki Nishiguchi

西口　知輝

Abstract

G protein-coupled receptors (GPCRs) are involved in a wide range of diseases with their high ligand specificity. Almost half of the commercial drugs are designed to target at GPCRs. Aiming to develop a novel drug for a severe drug eruption, Stevens Johnson Syndrome, I established two high-throughput assay systems and identified ten potential inhibitors for an inflammation-related GPCR, Formyl Peptide Receptor 1 (FPR1), in the thesis of my master degree. However, elucidation of various signal events, in addition to the two signal pathways, is essential for efficient drug discovery. Thus, the first aim of the doctor thesis was to establish additional assay systems for FPR1 to quantify ligand binding, G protein activation, β-arrestin binding and cAMP signaling. In addition, recent studies have suggested that oligomer formation of FPR1 might be involved in their activation, but assessment of the oligomeric patterns of FPR1 in living cells is still challenging because the oligomer formation is dynamic and heterologous. To reveal the full spectrum of the signal cascades triggered by the newly found inhibitors, I developed analytical methods to quantify the frequency and the duration of interactions among GPCRs and G proteins by using live-cell imaging techniques.

 I established four assay systems in total to measure the signal transduction efficacy of chemical compounds for FPR1. The direct binding of inhibitors to FPR1 was confirmed by competitive inhibition of fluorescent FPR1 ligand, detected with flow cytometry. The interaction of FPR1 with β-arrestin was measured with a split bioluminescence probe. The cAMP signaling was quantified with a bioluminescence probe. The G protein signaling was assessed by monitoring structural changes of G proteins with a FRET probe. The results demonstrated that an FPR1 specific agonist activated FPR1 with different efficacy and temporal patterns dependent on the signal transduction events, indicating the importance of measuring the signal efficacy with multiple methods with temporal information.

 Single molecule dynamics of FPR1 and G protein were investigated with Total Internal Reflection Fluorescence (TIRF) microscopy. FPR1 and G protein were genetically fused with SNAP-tag and Halo-tag to label with fluorescent dyes. Based on the fluorescence intensity, the fluorescent spots of FPR1 were categorized as either small or large oligomers and their populations were quantified. The result showed that the large oligomer fraction was increased after ligand stimulation, suggesting that the ligand stabilized the large oligomers of FPR1. Interactions between FPR1 and G protein were assessed by monitoring duration of colocalization events of the spots. Cumulative probability curves of the duration of the colocalization events showed that the colocalization duration between FPR1 and G protein was significantly increased by ligand stimulation. To clarify the relation between the large oligomer formation of FPR1 and the elongation of the G protein interaction upon ligand stimulation, the colocalization duration of the small and large oligomers of FPR1 was quantified. The small FPR1 oligomers showed more transient interactions with G proteins than the large oligomers both in the presence and absence

of the ligand. The effect of the ligand stimulation was only found in an increased interaction time of the large oligomer fraction with G protein. Therefore, the results suggested that FPR1 activation caused an elongation of the interacting time between G protein and oligomeric FPR1.

I established ligand binding assay, β-arrstin split luciferase assay, bioluminescence cAMP assay, and G protein FRET assay system for quantitative assessment of signaling patterns of FPR1 activation. The efficacy and kinetics of ligand stimulation were determined in the same cell type. Moreover, I developed a single molecule imaging system to reveal the stoichiometry of FPR1 and its interaction with G proteins in living cells during ligand stimulation. An increase in the large oligomer fraction of FPR1 and an elongation of the interaction with G protein were detected in response to the ligand stimulation. Further analysis suggested that the stable interaction was mainly caused by the large oligomer of FPR1. Therefore, the large oligomer fraction of FPR1 and their interaction kinetics with G protein would be novel indicators of FPR1 activation. Taken the present results all together, understanding of the dynamic and heterogenous signal transduction of GPCRs will accelerate the development of target specific pharmaceutical drugs.

Table of Contents

Abbreviations

A_1R	(adenosine) A_1 receptor
$A_{2A}R$	(adenosine) A_{2A} receptor
AC	adenylyl cyclase
ANOVA	analysis of variance
AP	(clathrin) adaptor protein
BG	O^6-Benzylguanine
BRET	bioluminescence resonance energy transfer
cAMP	cyclic adenosine monophosphate
cAR	cyclic AMP receptor
CCL-27	C-C motif chemokine ligand 27
CD8	cluster of differentiation 8
cpV	circular permutated Venus
cryo-EM	cryo-electron microscopy
CysH	cyclosporin H
CytoD	cytochalasin D
D_2R	(dopamine) D2 receptor
DAG	diacylglycerol
DM	dichroic mirror
DMF	N,N-dimethylformamide
DMEM	Dulbecco's Modified Eagle Medium
DMSO	dimethyl sulfoxide
Dyngo	Dyngo 4a
EC50	half maximal effective concentration
Eluc	Emerald Luc luciferase
Em.	emission wavelength
EMCCD	electron-multiplying charge-coupled device
ERK	extracellular signal-regulated kinase
Ex.	excitation wavelength
FBS	fetal bovine serum
FITC	fluorescein isothiocyanate
fMLP	formyl-methionyl-leucyl-phenylalanine
fNLFNYK	formyl-Nle-Leu-Phe-Nle-Tyr-Lys (Nle: norleucine)
FPR1	formyl peptide receptor 1
FPR2	formyl peptide receptor 2

FPR3	formyl peptide receptor 3
FRET	Förster resonance energy transfer
GDP	guanosine diphosphate
GFP	green fluorescent protein
Gi3 (=Gαi3)	G protein subunit α_{i3}
G protein	guanine nucleotide-binding protein
GPCR	G protein-coupled receptor
GRK	G protein-coupled receptor kinase
GTP	guanosine triphosphate
hAGT	human O^6-alkylguanine-DNA alkyltransferase
HBSS	Hank's balanced salt solution
HEK293	human embryonic kidney 293 cell
HEPES	4-(2-hydroxyethyl)-1-piperazineethanesulfonic acid
HLA	human leukocyte antigen
IC50	half maximal inhibitory concentration
IL-5	interleukin-15
IP$_3$	inositol trisphosphate
IVIG	intravenous immunoglobulin
MB6	methionine benzimidazole 6
MβCD	methyl-β-cyclodextrin
MSD	(2D) mean square displacement
mTq2	mTurquoise2
NA	numerical aperture
NHS	N-hydroxysuccinimide
N.S.	not significant
OXE-R	oxoeicosanoid (OXE) receptor
PAGE	poly-acrylamide gel electrophoresis
PBS	phosphate-buffered saline
PDB	Protein Data Bank
PEG	polyethylene glycol
Pen Strep	penicillin streptomycin
pERK	phosphorylated ERK
PIP$_2$	phosphatidylinositol 4,5-bisphosphate
PKA	protein kinase A
PLC	phospholipase C
PM	plasma membrane

PMT	photomultiplier tube
PTX	pertussis toxin
PVDF membrane	polyvinylidene difluoride membrane
RhoA	Ras homolog family member A
RIP3	receptor-interacting serine/threonine-protein kinase 3
ROS	reactive oxygen species
s.d.	standard deviation
SDS	sodium dodecyl sulfate
s.e.m.	standard error of the mean
SJS/TEN	Stevens-Johnson syndrome/ toxic epidermal necrolysis
S/N	signal to noise ratio
TBST	tris-buffered saline supplemented with Tween 20
TEA	triethylamine
TGFα	transforming growth factor alpha
TIRF(M)	total internal reflection fluorescence (microscopy)
TLC	thin-layer chromatography
TMR	tetramethylrhodamine
UV	ultraviolet
WKYMVm	Trp-Lys-Tyr-Met-Val-D-Met-NH$_2$
WT	wildtype

Chapter 1

General Introduction

1-1. G protein coupled receptor (GPCR)

G protein coupled receptors (GPCRs) are membrane-localized proteins, which are involved in various kinds of signaling, such as visual perception, metabolism, inflammation, and neurotransmission. Each GPCR has its own ligand specificity toward a diverse set of extracellular stimuli, such as peptides, hormones, organic molecules, and photons. By designing small molecules that specifically bind to certain GPCRs, one can control downstream signals and following biological phenomena. Hence, GPCRs are widely recognized as promising targets for drug discovery. Nearly a half of the commercially available pharmaceutical drugs have been designed to target to GPCRs. To understand the signal transduction mechanisms and to develop efficient ligands for GPCRs, massive efforts have been made to obtain 3D structural information of GPCRs[1]. Recently emerged cryo-EM structural analysis has accelerated the understanding of activation mechanisms of GPCRs by revealing 3D structures of ligand- and G protein-bound GPCRs[2] (**Fig. 1-1**).
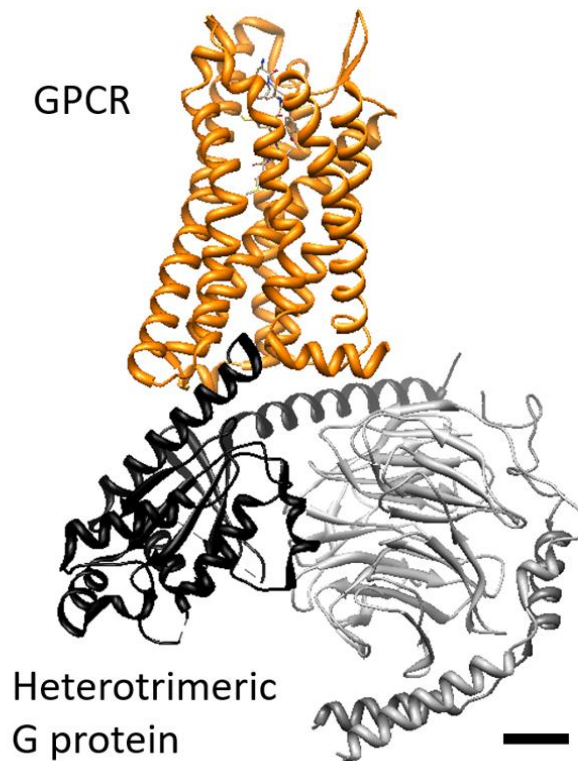

Fig. 1-1. 3D protein structures of a GPCR and a signal transduction mediator, G protein (PDB: 6OMM[3]). GPCR is shown in orange, G protein α-subunit is shown in black, and βγ-subunits are shown in gray. GPCRs has seven α-helical structures embedded in cell membrane, whereas G protein binds to the internal side of the cell membrane by lipid modifications. Scale bar: 10 Å.

1-2. Signal transduction of GPCR

Signal transduction of GPCRs involves various molecules and proteins in the cells[4,5] (**Fig. 1-2**). A canonical model of GPCR activation has described that ligand binding causes structural changes of GPCRs, promoting an interaction with heterotrimeric cytosolic proteins called Guanine nucleotide binding protein (G protein). The heterotrimeric G protein consist of α, β, and γ subunits, which have lipid modifications to localize at cell membrane[6]. Upon GPCR-G protein interaction, Gα subunit dissociates from GDP and binds to cytosolic GTP, resulting in the dissociation of the Gα subunit from Gβγ heterodimer. The free Gα subunits diffuse on the cell membrane to interact with and activate effector proteins. Subsequently, the effector proteins enzymatically increase or decrease the concentrations of signaling molecules. The signal cascade, including G protein dissociation and effector activation, is repeated until GPCRs are quenched by a scaffold protein called β-arrestin. The β-arrestin recruitment induces an accumulation of adaptor proteins (AP) and clathrins, resulting in the internalization of GPCRs by endocytosis. The desensitized GPCRs are partly recycled back to the plasma membrane, whereas others are sorted into lysosome to digestion. The cycle of activation, desensitization, and resensitization are a common character for GPCRs.
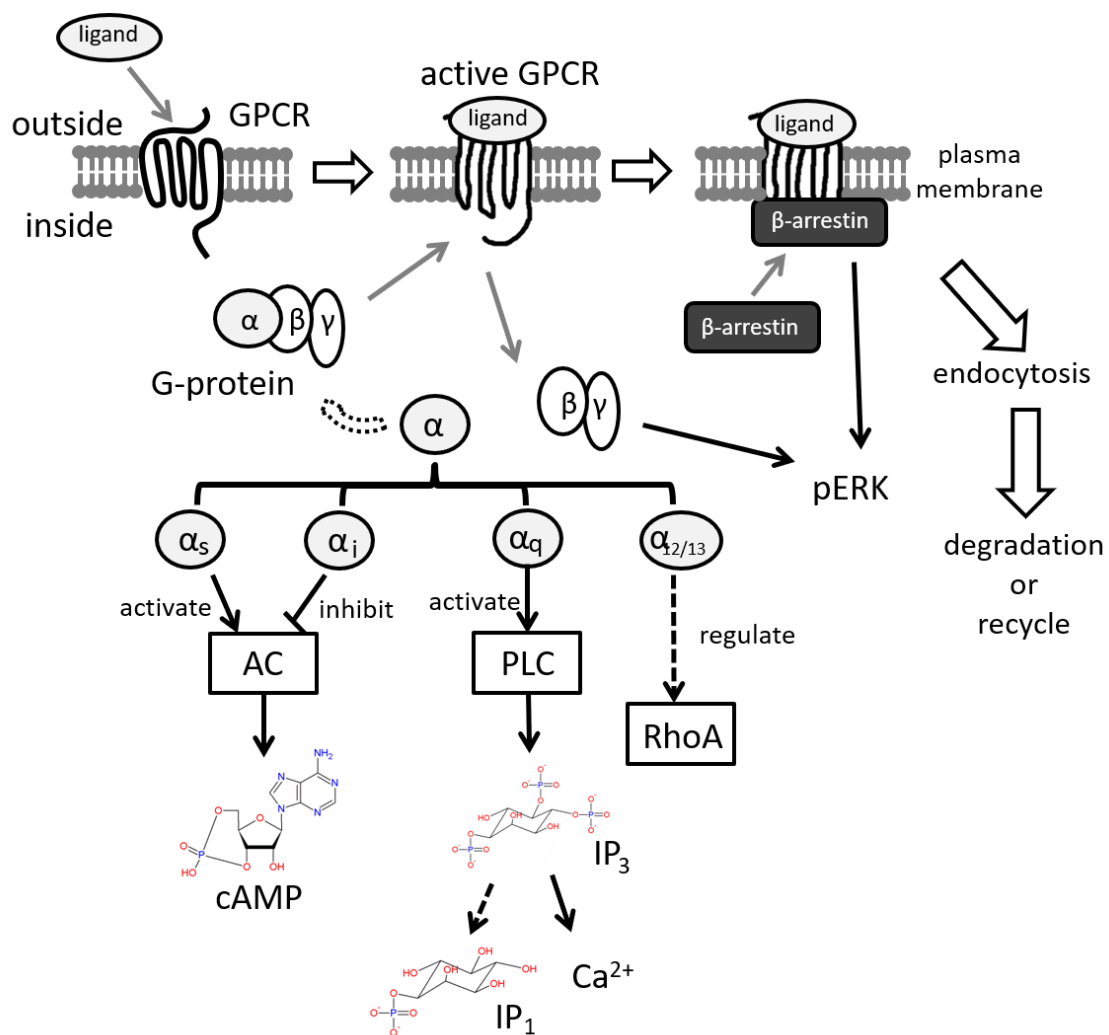
Fig. 1-2. Overview of GPCR signal transductions. Upon ligand stimulation, GPCRs interact with and dissociate the heterotrimeric G proteins into α-subunit (Gα) and the others. Four subtypes of Gα, Gs, Gi, Gq, and $G_{12/13}$ interact with their own downstream effector proteins to regulate cell functions. The free Gβγ has also effector proteins. After G protein activation, GPCRs form a stable interaction with β-arrestin, triggering downstream signal transduction and endocytosis of the receptor.

GPCRs transduce different patterns of signaling by coupling to different sets of G proteins[7], by transducing signals through Gβγ subunits[8], by interacting to β-arrestin with different conformations[9], by localizing in endosomes[10], and by forming homo- and hetero-oligomers[5] (**Figs. 1-2 and 1-3**). Understanding of the complicated mechanism of GPCR signal transduction has provided fruitful information for pharmaceutical drug development with more specificity and less side effects[11,12].
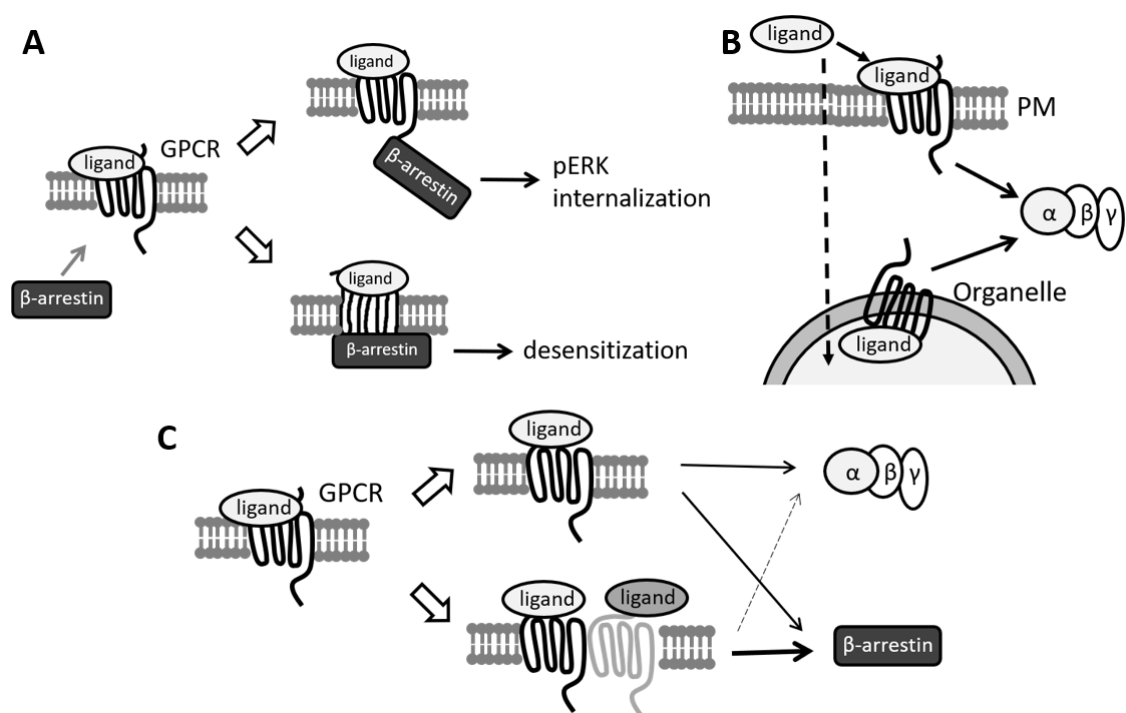
Fig. 1-3. Recently revealed heterogenous signal transduction mechanisms. (A) Functionally distinct two modes of β-arrestin binding to GPCRs. "Tail" conformation triggers β-arrestin signaling and interalization, but "core" conformation is required to inhibit G protein activation. (B) Location bias of GPCRs in the cells. GPCRs are localized on both plasma membrane (PM) and other membrane of internal organelles, such as endosome and golgi apparutus. The GPCRs inside the cells can display unique features in ligand recognition patterns, protein complex formation, and downstream signal transdutions. (C) Typical view of the signal bias induced by homo- and hetero-oligomerization. Many GPCRs can function as monomers, but they are also capable of interacting with other GPCRs. Some GPCRs transactivate, override, or quench the activity of the adjacent GPCRs[13].

Mammalian cells express 16 types of Gα subunits, being categorized in four groups, Gi/o, Gs, Gq, $G_{12/13}$, based on their cognate effector proteins[14] (**Fig. 1-2**). Gi/o interacts with adenylyl cyclases to inhibit the production of cyclic adenosine monophosphate (cAMP). In contrast, Gs stimulates adenylyl cyclases and increases the cAMP production. Gq mainly activates phospholipase C (PLCs), which decomposes PIP_2 into DAG and IP_1. The soluble IP_1 diffuses in cytosol and activates ER-localized ion channel, leading to Ca^{2+} efflux. $G_{12/13}$ couples to small G protein, RhoA, and further activates actin polymerization[15]. The soluble small molecules, such as cAMP and Ca^{2+}, are called second messengers, being long utilized as markers for the G protein activations. Each GPCR has different specificities for G protein binding, resulting in the different downstream signal transduction. Studies have solved crystal structures of the GPCR-G protein interface[16] and revealed a common molecular mechanism in the allosteric reaction of GDP release during the G protein activation[17]. Comprehensive analyses on

available crystallography data have revealed that the selectivity of G protein coupling is achieved by multiple key interactions between GPCRs and G protein interfaces[18]. The study has demonstrated that the presence of multiple recognition sites enabled the specific interactions of divergent structures of GPCRs with a certain set of G protein. The G protein selectivity of GPCRs strongly diversifies the downstream signaling.

The signal transmitter is not limited to the G protein α-subunits. Gβγ subunits and β-arrestins can activate downstream signals, such as Ca^{2+} efflux and pERK production (**Fig. 1-2**). Although the signal transduction from the Gβγ-subunits have not been fully elucidated, the activation mechanisms of β-arrestins have been intensively investigated. Cryo-EM structures have revealed two conformations of β-arrestin binding to GPCRs[9] (**Fig. 1-3A**). A later study has revealed the relevance of the two conformations with two biologically distinct functions, desensitization of G protein signals and downstream signal activation of β-arrestin[19]. Artificial β-arrestin recruitment to GPCRs by using light-dependent dimerizers have triggered a unique signal transduction pattern, suggesting the importance of conformational changes of β-arrestin for the physiological signal transductions[20]. Interestingly, β-arrestin has been shown to be functional as a signal transducer even after dissociating from GPCRs by interacting with membrane lipids[21,22]. These reports suggest that GPCRs catalytically activate three types of proteins, Gα, Gβγ, and β-arrestin, during the signal transduction.

Although GPCRs localize and function mainly on the cell membrane, GPCRs in the endosomes also exhibit functional responses for ligands (**Fig. 1-3B**). For example, β1-adrenergic receptor triggers local cAMP signals on the Golgi apparatus[23]. Peptide ligands activate exclusively the cell-membrane-localized μ opioid receptors, whereas synthetic drugs additionally activate μ opioid receptors in the somatic Golgi apparatus[24]. Other researchers have revealed that the membrane-residency time of ligand-stimulated μ opioid receptor has been correlated with phosphorylated ERK (pERK) levels[25]. These studies have demonstrated that localization of GPCRs affect the signal transduction patterns. Upon ligand stimulation, β2-adrenergic receptors formed two subpopulations, GRK-phosphorylated receptors that internalize as monomers and PKA-phosphorylated receptors that stay on the cell membrane as dimers[26]. These results indicate that functionality of GPCRs are fine-tuned by the trafficking of GPCRs.

The signal transductions of GPCRs are also controlled by adjacent GPCRs by forming oligomers (**Fig. 1-3C**). Representative example of heterooligomer formation is observed between one subtype of adenosine receptors, $A_{2A}R$, and one subtype of dopamine receptors, D_2R, in nerve cells[12,27]. Dopamine activates Gαi-coupled D_2R to decrease the cytosolic cAMP level, whereas adenosine counteracts the D_2R response by activating Gαs-coupled $A_{2A}R$ to increase the cAMP level. In addition to the signal competition at the G protein level, activation of $A_{2A}R$ directly alter the conformation of D_2R in the heterooligomers, reducing the ligand binding affinity of D_2R.

1-3. Ligand bias and non-equilibrium activation

Various methods have been developed to evaluate the potency of chemical compounds to activate or inhibit GPCRs. TGFα shedding assay has been developed for orphan GPCRs[28], and label-free methods using surface plasmon resonance has enabled the observation under near physiological conditions[29,30]. Including these assays, most pharmacological assays for the GPCR activity have been conducted based on the assumption that GPCRs are in a simple two-state equilibrium between an active state and an inactive state. Agonists induce the active conformation of GPCRs, whereas inhibitors induce the inactive conformation (inverse agonists) or block the equilibrium shift (neutral antagonists). This simple activation model is useful in narrowing down drug candidates from a huge number of chemical compounds. However, growing numbers of studies have suggested that GPCRs have multiple types of active conformations[31–33]. The balance of the active structures is tightly regulated by bound ligands and reaction kinetics of signal transduction (**Fig. 1-4**).
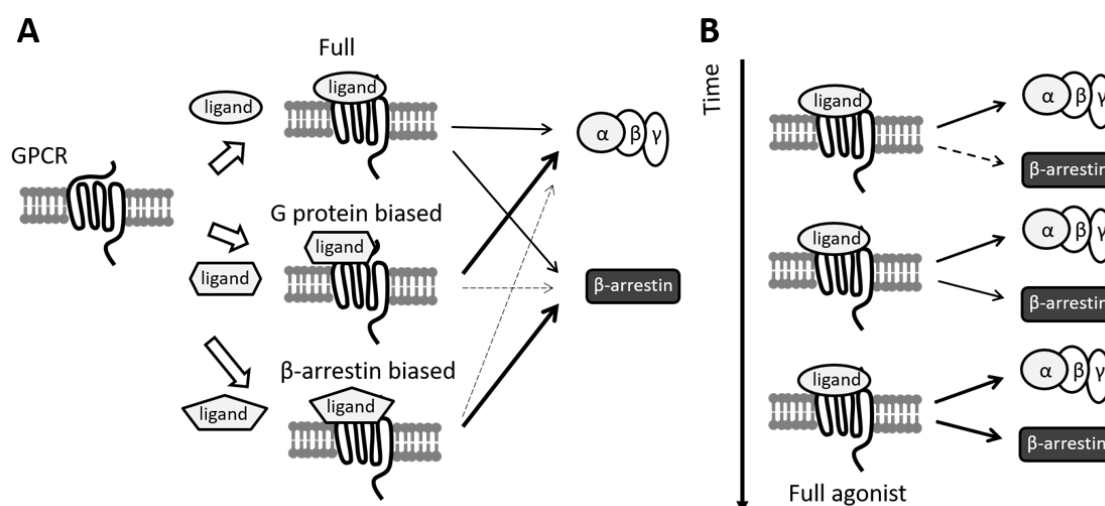
Fig. 1-4. Biased signal transduction. (A) Schematic diagram of ligand biases. Full agonists trigger all the downstream signaling pathways, whereas G protein biased and β-arrestin biased agonists selectively activate one of the signaling pathways. (B) Interference of temporal patterns of signal transduction in ligand bias. If one signal pathway reaches an equilibrium in an early time point (G protein pathway in the figure), the ligand is apparently detected as biased in the early time point, but the same ligand can be categorized as a full ligand in the late time points.

Some of clinical trials suffer from severe side effects. Agonists for adenosine A1 receptor, A_1R, have been expected to promote tissue protection and tissue repair under conditions of cellular stress, especially in the case of ischemia-reperfusion injury[34]. However, the same agonist activation to A_1R has induced severe heart damages, including reduced heart rate. This unwanted effect has been mediated by G protein activation, whereas the therapeutic effect has been provided by the downstream

signaling of β-arresin. Atypical A_1R agonists, VCP746 and capadenoson, have retained the cytoprotective ability without causing the heart damage. Biochemical analysis has revealed that VCP746 had a significant bias away from G protein signals[34]. Therefore, development of biased agonists is highly expected for signal specific pharmaceutical drugs (**Fig. 1-4A**). Among the clinically approved drugs, one of μ-opioid receptor agonists, TRV130, has been reported to have signal bias of activating Gαi proteins selectively with weak β-arrestin recruitment[35]. Only few biased antagonists have been reported, including the one for 5-oxo-6E, 8Z, 11Z, 14Z-eicosatetranoic acid (5-oxo-ETE) receptor (OXE-R)[36]. Gue1654, a biased antagonist for OXE-R, does not interfere with Gα signaling but inhibit OXE-R-induced Gβγ signaling and β-arrestin recruitment. These growing numbers of researches demonstrate that biased ligands are promising and efficient tools to manipulate a selected part of the pluridimensional functions of GPCRs.

Mathematical models have been proposed to quantify the magnitude of the ligand bias[37], but it is important to detect the activation states of GPCRs over time (**Fig. 1-4B**). Concentration dependence curves of G protein activation have been shifted within a few seconds after ligand stimulation, suggesting that the signal transduction reactions proceed in non-equilibrium states[38]. Theoretical analysis suggested that slow dissociation kinetics with downstream effector proteins may affect the upstream equilibrium of G protein dissociation reaction[39]. Hence, ligand bias should be dictated with temporal information.

1-4. Formyl Peptide Receptor 1 (FPR1): A key mediator of severe drug eruptions

Formyl Peptide Receptors, including FPR1, FPR2, and FPR3, are ones of the prototypical GPCRs. FPRs are mainly expressed by phagocytic leukocytes and are involved in host defense and inflammation. From the pathological roles, FPRs are also recognized as one of patten recognition receptors, in which Toll-like receptors are the best studied[40]. Both FPR1 and FPR2 recognize bacterially and mitochondrially derived formyl peptides, but they cause different inflammatory responses[41]. FPR1 activation causes chemotaxis of neutrophils towards injured sights and initiates inflammatory responses including superoxide generation, degranulation, and finally apoptosis of the neutrophils[42] (**Fig.1-5**). High concentrations of formyl peptides or anti-inflammatory lipid mediators can activate FPR2, leading to the resolution of inflammatory reactions. Moreover, FPR1 and FPR2 are involved in virus infection and malignant tumor growth[40]. FPR1 serves as a plague receptor[43] and FPR2 serves as an influenza receptor[44]. Reportedly, expression levels of FPRs have been positively correlated with the severity of malignant tumor cells, but the absence of FPRs has led to an inflammation-associated tumorigenesis[40]. Controlling the contradicting roles of FPRs in tumor growth might be one of the potential targets for cancer treatment.
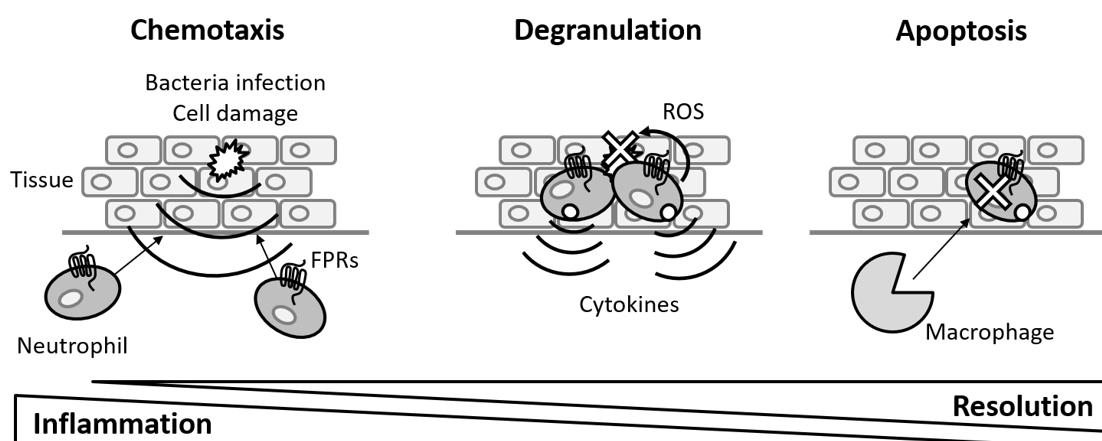
Fig. 1-5. Physiological roles of FPRs in inflammation. Infectious bacteria and damaged cells produce formyl peptides, inducing neutrophil infiltration into the damaged tissues by activating FPRs. FPR activation triggers degranulation to release proinflammatory cytokines, which amplify the immune responses. At the same time, FPR activated neutrophils produce reactive oxygen species (ROS) to kill and remove the pathogens. After the inflammation process, tissue homeostasis is recovered by the apoptosis of the infiltrated neutrophils.

FPR1 is also involved in the progression of severe drug eruption, Stevens-Johnson Syndrome (SJS) and toxic epidermal necrolysis (TEN)[45] (**Fig. 1-6**). They are rare but life-threatening conditions as a result of adverse drug reactions. When occurring, SJS and TEN patients suffer from skin eruptions on their whole body within a few hours. The overall incidences of SJS and TEN have been estimated at

1 to 6 cases per million person each year and 0.4 to 1.2 per million person each year, respectively. The mortality rate is up to 25 % for TEN, which is characterized by greater than 30 % of skin detachment. As for the survivals, the inflammation can spread over the buccal and ocular mucosa and cause severe consequences such as loss of sight. Recent studies have suggested that the occurrence of the diseases might be decreased by human leukocyte antigen (HLA) screening and that the diseases might be diagnosed at the onset by monitoring biomarkers, such as CCL-27, IL-15, galectin-7, and RIP3[46]. Currently, several treatments for SJS/TEN have been proposed, such as the intravenous immunoglobulin (IVIG) therapy, and the use of corticosteroids or anti-tumor necrosis facter-α, although the effectiveness of the treatments is still controversial. This lack of information is due to the low occurrence rate of the diseases. The low occurrence rate has also discouraged pharmaceutical companies to develop new drugs for SJS/TEN because of the small market in spite of the need of huge research investments.
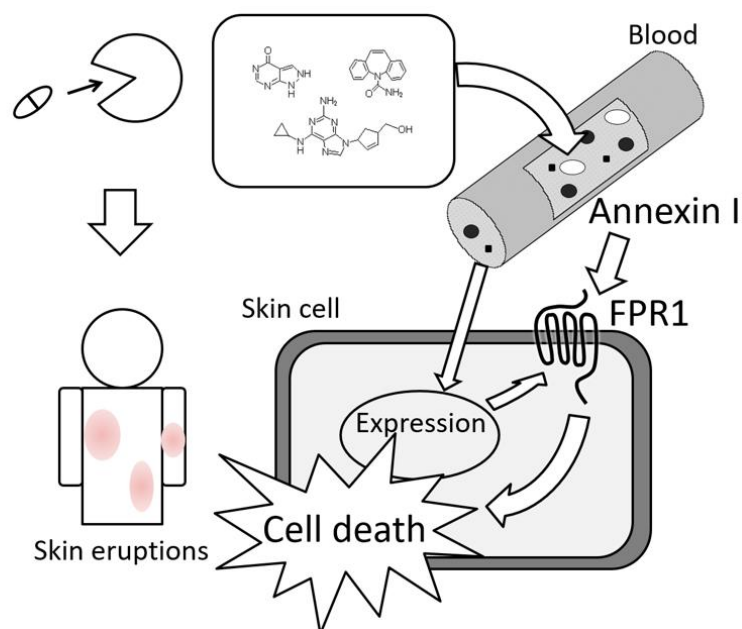
Fig. 1-6. Molecular mechanisms of Stevens Johnson Syndrome (SJS) and Toxic Epidermal Necrolysis (TEN). In SJS/TEN patients, causative drug intake induces rapid skin eruptions and mucosal erosions on their whole body. This drug reaction is mediated by many types of leukocytes and skin cells. Previous investigations have revealed that drug-specific CD8^{+} T cells induce FPR1 expression on keratinocytes (skin cells). Monocytes from the SJS/TEN patients produce Annexin AI peptides, which trigger necroptosis of the FPR1-expressing keratinocytes. The finding indicates that inhibition of FPR1 with chemical compounds serve as a potential therapeutics for SJS/TEN.

Several groups have tried to develop agonists and antagonists for FPRs as pharmaceutical drugs. For example, 5 million chemical compounds have been screened against FPR1 and FPR2, providing highly

specific agonists and antagonists for each receptor with the dissociation constants of the order of 1 nM[47]. Many screening campaigns have revealed that FPR1 binds to diverse structures of chemicals, including peptides, chromones, coumarins, quinones, lignans[48] (**Fig. 1-7**). Despite of the growing repertoire of the agonists and antagonists, none is approved as pharmaceutical drugs probably due to the lack of binding affinity, poor biophysical properties *in vivo*, and poor signal selectivity. Based on computational simulations and site-directed mutagenesis, key residues of FPR1 and key structures of ligands for the efficient ligand-receptor binding have been identified[49,50]. Recently, an exciting report has solved a cryo-EM structure of FPR2 binding to a ligand and a G protein (**Fig. 1-1**). The structure revealed the mechanism for the difference in the ligand recognition patterns between FPR1 and FPR2[3]. This information will accelerate the development of an efficient drug that targets to FPR1 and FPR2.
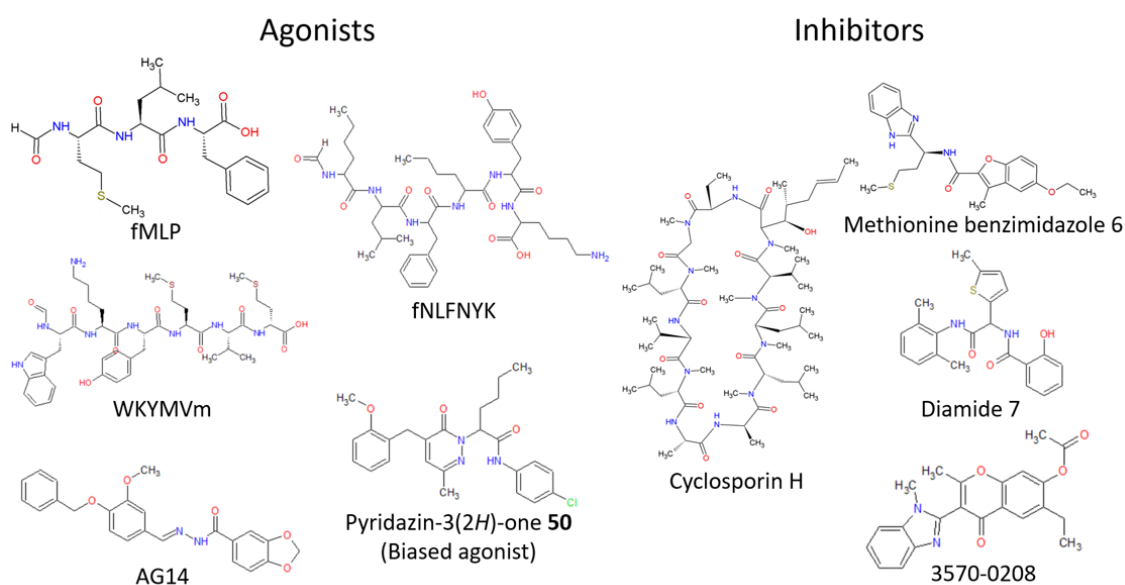
Fig. 1-7. Specific agonists and inhibitors for FPR1. fMLP and Cyclosporin H are naturally occurring agonist and antagonist, respectively. fNLFNYK[51] was rationally designed as a formyl peptide agonist containing a free amine group. WKYMVm[52], AG14[53], Pyridazin-3(2*H*)-one **50**[54,55], methionine benzimidazole 6[56], diamide 7[56], and 3570-0208[57] have been identified and improved by high throughput screening and chemical modifications.

To obtain novel drug candidates for SJS/TEN, I performed a chemical library screening for FPR1 inhibitors as my Master course research. In brief, two independent high-throughput assay systems, calcium assay and arrestin assay, were established based on fluorescence and bioluminescence probes, respectively. A pilot screening was conducted with the established systems on a 9,600-compound library, from which 1% of the compounds were extracted as Hit compounds. Following experiments to confirm reproducibility and specificity of the inhibitions of the Hit compounds finally identified 10 drug candidates with high inhibition capacity for FPR1 (unpublished data). The most efficient Hit

compound inhibited the FPR1 activation as effectively as the already established peptide inhibitor for FPR1 called cyclosporin H. The results confirmed the potency of the Hit compound to inhibit the calcium signaling and arrestin signaling, but more detailed investigation of signal controlling capacity will be desired to obtain highly specific drugs for SJS/TEN.

1-5. Fluorescence-based techniques for detection of fast and dynamic signal transduction

1-5-1. Basic characteristic of fluorescence and bioluminescence proteins

The best-known fluorescent protein is the green fluorescent protein (GFP) derived from a jelly fish, *Aequorea victoria*. GFP is composed of 238 natural amino acids, exhibiting bright green fluorescence upon blue light excitation[58]. After proper folding of β-barrel structure of GFP, cyclization reactions are induced at Ser65-Tyr66-Gly67 residues, forming a chromophore of 4-(*p*-hydroxibenzylidene)imidazolidine-5-one (**Fig. 1-8A**). Although proteins generally have UV fluorescence originated from tyrosine and tryptophan, the fluorescence from the GFP chromophore is in a range of visible light, providing an outstanding property for visualization of specific proteins in living cells[59]. Intensive mutation studies have developed color variants ranging from ultramaline (424 nm)[60] to yellow (527 nm)[61] or even red (585 nm)[62]. Many other fluorescent proteins have been derived from marine organisms, in which the most famous protein is DsRed from *Discosoma sp.*[63]. DsRed variants have further expanded the color pallet of fluorescent proteins to far-red region (650 nm)[64]. Using the fluorescent proteins, four or more proteins can be simultaneously labeled and detected with fluorescence microscopy and flow cytometry.

Luciferases are naturally occurring proteins that catalytically produce luminescent molecules. Various luciferases were derived from beetles (firefly luciferase, click beetle luciferase)[65], sea pansy (Renilla luciferase)[66], copepod (Gaussia luciferase)[67], and sea shrimp (NanoLuc)[68]. There are several luminogenic substrates, including D-luciferin and coelenterazine. Generally, the luciferases catalyze an oxidative reaction of the substrates. The products are stochastically decomposed into electronically excited molecules and emit luminescence emission (**Fig. 1-8B**)[69]. The luminescence emission is proportional to the amount of the luciferases in a wide concentration range, providing efficient tools for quantification of transcription activity and visualization of protein locations. Compared to fluorescent proteins, experiments with bioluminescent proteins cause low cytotoxicity and low background levels owing to no need for the excitation light. Coelenterazine luciferases, including Renilla luciferase, Gaussia luciferase, and NanoLuc, emit strong blue bioluminescence suitable for luminescence imaging, fast detection, and detection of protein-protein interactions using bioluminescence resonance energy transfer (BRET) technique. In contrast, beetle luciferases offer naturally various color variants from green to red[70,71]. Mutagenesis for the luciferase and chemical modifications for the substrate expanded the color variants from blue to far red[72,73,74]. Temporally

sustained luminescence emission of the beetle luciferases is also attractive for *in vivo* imaging and long-term observation, such as circadian rhythm[75].
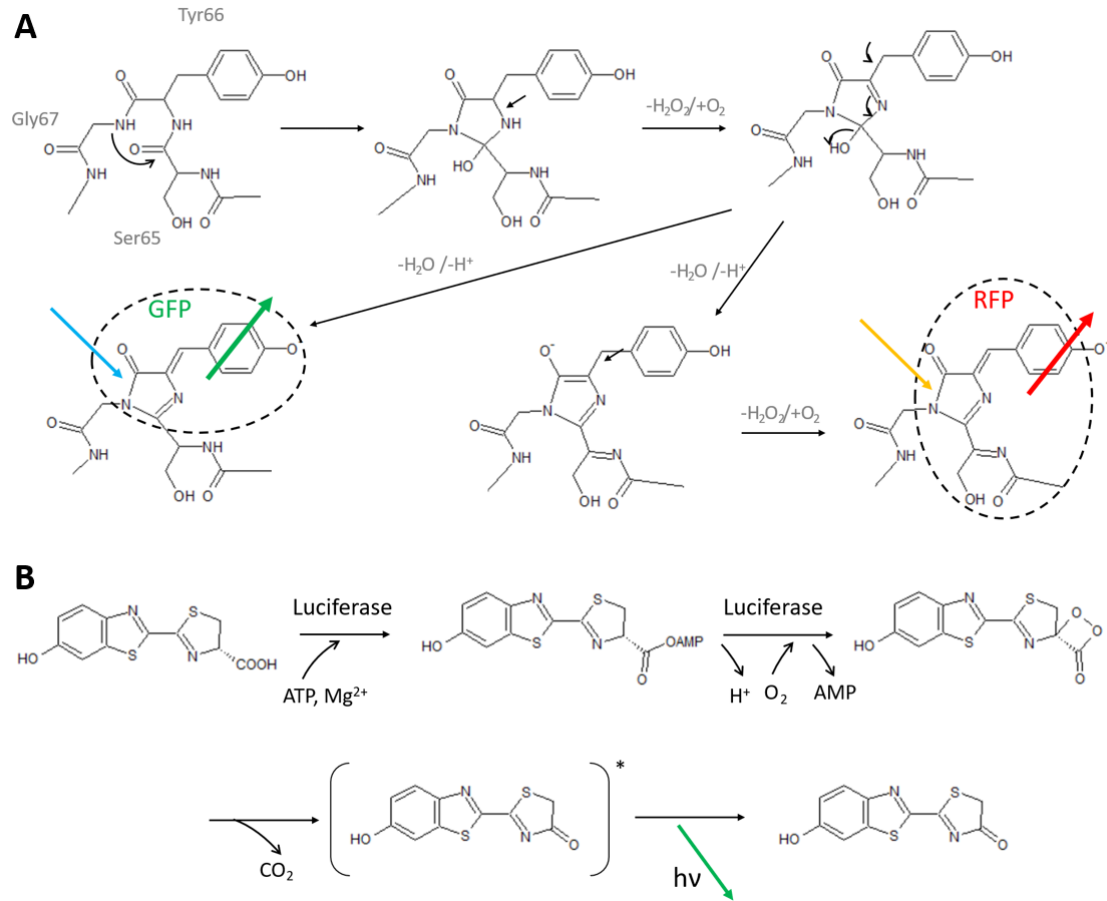
Fig. 1-8. Chemical reactions of fluorescent proteins and bioluminescence proteins. (A) Formation of fluorophore in GFP and RFP at the three amino acid sequences. After cyclization reaction, oxidation reaction produces conjugated phenol group at the original Tyr66 in GFP. The conjugation system is elongated to the backbone of Ser65 in RFP, resulting in a red-shift of fluorescence emission. The fluorophores are highlighted with dotted circles. Amino acid mutations into GFP and RFP change the structure of chromophore and the fluorescent color. (B) Formation of an electronically excited molecule by enzymatic reactions of firefly luciferases. The substrate, D-luciferin, is converted into oxyluciferin in the binding pocket of the firefly luciferases. Local hydrophobic interactions with the binding pocket of firefly luciferases change bioluminescence colors.

1-5-2. Basic characteristic of fluorescence protein tags.

Fluorescent proteins have enabled the detection of proteins of interest existing in living cells in real time. Although tremendous amounts of GFP and RFP variants have been developed, they have limitations in fluorescence intensity and photostability. To overcome the limitations, methods have been developed to specifically label the proteins of interest with exogenously added fluorescent dyes with high fluorescence intensity and photostability. The early developed probes have utilized the biotin-avidin interaction[76], and cysteine-arsenic interaction[77]. Following specific protein tags, including SNAP-tag, CLIP-tag, and Halo-tag, have been derived by mutating enzymes. Enzyme-derived protein tags can be expressed in living cells, have high ligand specificity, and allow the dye labeling reaction to proceed under physiological conditions. These features are suitable for multi-color labeling in living cells.

The first candidate, SNAP-tag, has been derived from O^6-alkylguanine-DNA alkyltransferase (hAGT)[78] (**Fig. 1-9A**). hAGT have an original feature of recognizing alkylguanine-DNA to transfer the alkyl group of the DNA to one of cysteine residues in hAGT itself. This bonding formation is utilized to covalently label the proteins of interest with exogenously added molecules. To visualize proteins of interest with SNAP-tag, the target proteins are fused with the SNAP-tag (hAGT with one mutation of G160W), and the fluorescent dye is chemically fused with benzylguanine moiety (**Fig. 1-9A**). When two components are mixed in physiological buffer, the reaction proceeds in an order of ten minutes and produces an irreversible covalent bond between SNAP-tag and the dye with a biproduct of guanine molecule. The typical reaction rate is 3,000 $M^{-1}s^{-1}$ [78]. The protein size of SNAP-tag is smaller than GFP (20 kDa vs. 27 kDa). CLIP-tag is a mutant SNAP-tag developed for the orthogonal labeling with SNAP-tag[79]. Introduction of eight mutations have changed the ligand recognition of SNAP-tag from benzylguanine to benzylcytosine (**Fig. 1-9B**). The reaction rate of CLIP-tag was slightly decreased to 1,200 $M^{-1}s^{-1}$.

Another protein tag, Halo-tag, has been developed from bacterial haloalkane dehalogenase[80] (**Fig. 1-9C**). This enzyme originally removes halides from aliphatic hydrocarbons and produces alcohol by subsequent hydrolysis. By mutating histidine at position 272, the reaction is stopped in the intermediate state before the hydrolysis. Trapping the intermediate structure enables irreversible binding of the haloalkanes with the mutant protein. The binding reaction of an improved mutant of the haloalkane dehalogenase, Halo-tag, is fast (2.7×10^6 $M^{-1}s^{-1}$) and highly specific because the bacterial enzyme utilizes an enzymatic reaction foreign to mammalian systems[80]. The protein size of Halo-tag is slightly larger than GFP (33 kDa vs. 27 kDa), but fusion of Halo-tag is tolerant for many proteins to function.

Growing number of protein labeling tags have been reported. BL-tag[81] and PYP-tag[82] utilize fluorogenic dyes. The fluorescence emission is quenched by maleimide groups or nitrobenzene group in the dye molecules. After bonding formation with protein tags, the quenching groups are removed,

and the dyes become fluorescent. These techniques enable no-wash labeling of the proteins and real time detection of the labeling reaction. Y-FAST, developed form PYP-tag, forms a reversible covalent bond with fluorescent dyes[83]. The binding of the dyes to Y-FAST red-shifts the absorption spectra of the fluorescent dyes, enabling the specific detection of bound molecules. The rapid and reversible bonding formation is beneficial for long time observation because photobleached fluorescent dyes can be replaced to new dyes abundant in the solution. Future works will clarify and improve advantages and limitations of these methods, such as cell toxicity, dependence on local cell environment, reaction rate, signal to background ratio, and color variations.
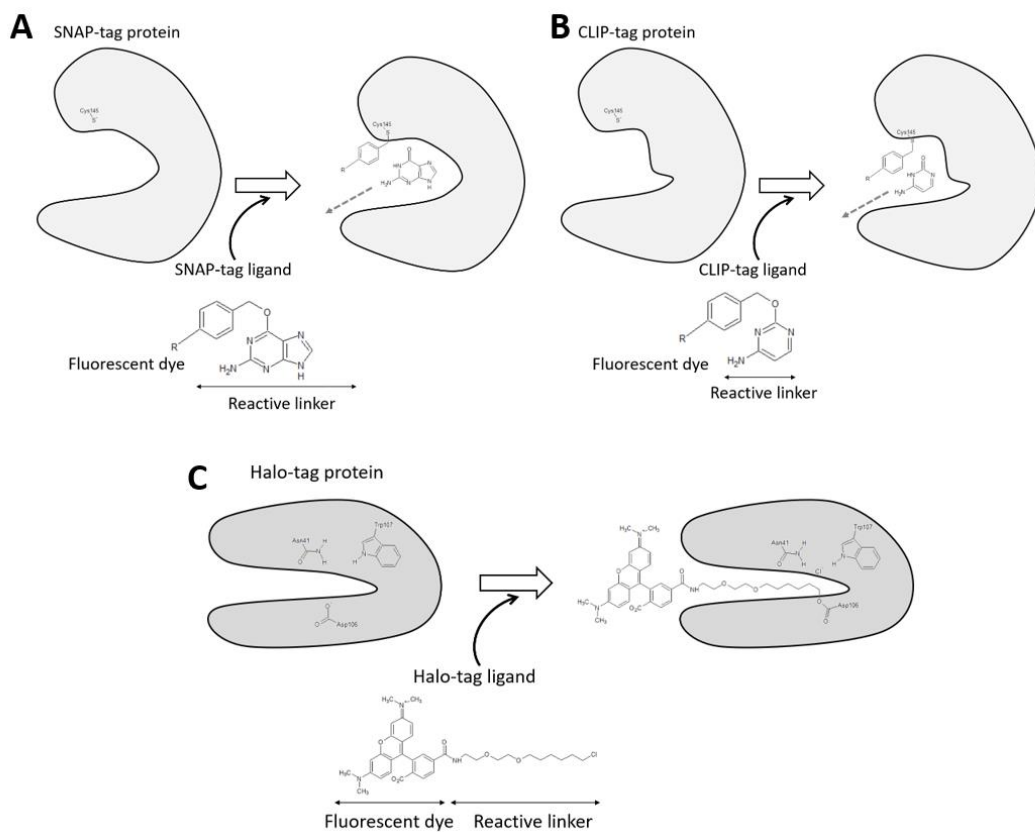
Fig. 1-9. Principle of covalent bonding formation of exogenously added fluorescent molecules with protein tags. (A) SNAP-tag recognizing O^6-benzylguanine groups to form covalent bonding at the cysteine residue. (B) CLIP-tag, developed by mutagenesis of SNAP-tag, recognizing O^2-benzylcytosine groups to form covalent bonding at the cysteine residue. (C) Halo-tag recognizing chloroalkane groups to form covalent bonding at the aspartic acid residue.

1-5-3. Basic principle of objective-type single molecule imaging

1-5-3-a. Optical setup: Total internal reflection fluorescence microscopy

Fluorescent proteins and fluorescent molecules can be visualized with fluorescence microscopy. Conventional fluorescence microscopy includes epi-fluorescence microscopy and confocal microscopy. Under epi-fluorescence microscopy, the cell specimen is irradiated by penetrating light, exciting all the fluorophore in the cells (**Fig. 1-10A**). Under confocal microscopy, very small volume (200×200×1000 nm) of the cells are excited at a time (**Fig. 1-10B**). By scanning the excitation region, images of optical section of the cells are obtained. To achieve single molecule imaging, the background fluorescence must be reduced to less than the fluorescence intensity of single molecule of the dyes. Total internal reflection fluorescence microscopy (TIRF-M) enables even thinner irradiation of the bottom surface of the cells than the other techniques (**Figs. 1-10A, B**). Total internal reflection is an optical phenomenon that occur when incident light hits the interface between two optical media of different refractive indices at an angle greater than the critical angle. Beyond the angle, the incident light is totally reflected at the interface, but the electromagnetic field extends into the second media, which is called evanescent wave. Under TIRF microscopy, fluorophores on the cell surface less than 200 nm away from the glass surface are exclusively excited by the evanescent wave. This very shallow but wide field detection (20,000×20,000×200 nm) of fluorescent molecules is advantageous for real-time single molecule tracking in living cells. I achieved the TIRF observation with a homemade optical setup, where the angle of the incident light into the glass surface can be manually modulated from epi-fluorescence mode to TIRF mode (**Fig. 1-10C**).
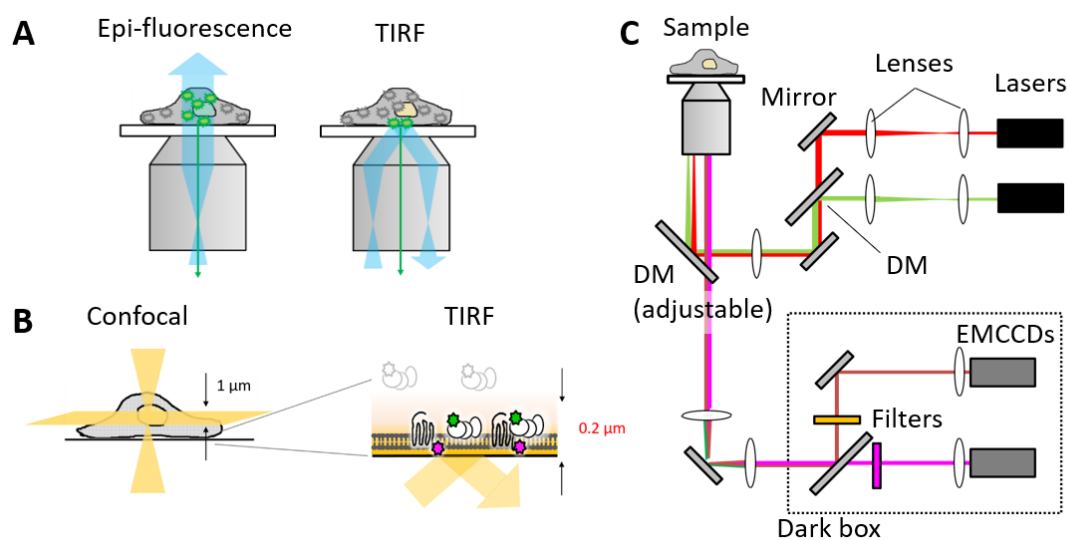
Fig. 1-10. Optical setup of TIRF microscopy compared to conventional microscopies such as confocal microscopy and epi-fluorescence microscopy. (A) Difference in light paths for epi-fluorescence microscopy and TIRF microscopy. (B) Difference in excitation volumes for confocal microscopy and TIRF microscopy. (C) An optical setup for TIRF microscopy. DM: Dichroic Mirror.

1-5-3-b. Automated single particle detection

Image analysis is a big challenge in single molecule imaging. Hundreds to thousands of fluorescent molecules have to be identified and followed over time in each movie. The typical S/N ratios of fluorescent intensity at the spots are low (sometimes less than 3), meaning that fluorescent particles might transiently disappear only because of a random fluctuation of the fluorescence intensity. To solve the problem, Jaqaman et al. has proposed a basic algorithm for particle detection and particle tracking[84]. Based on the theory, open software of single molecule tracking has developed, such as U-track[84] and TrackMate[85]. General protocols include noise reduction, segmentation, position determination, tracking, and statistical analysis of single molecule characteristics[86]. First, the raw data typically containing a few hundred frames of 256×256-pixel images with intensity values of 0-65535 were recorded by TIRF observation (**Fig. 1-11A**). Considering that images of single molecules are detected as diffraction limited spots with the diameter of λ/2NA (λ: wavelength of the incident light, NA: numerical aperture of the objective), shot noises are removed by filtering the images with 2D Gaussian curves with the diameter of λ/2NA (**Fig. 1-11B**). Then areas where fluorescence intensity is higher than a fixed threshold value are selected as spot candidates if the size is larger than the expected size of the diffraction limited spot (**Fig. 1-11C**). The spot candidates which are present near in the consecutive frames are connected to form single molecule tracks (**Fig. 1-11D**). Finally, too short single molecule tracks (typically less than 3 frames) are rejected and the spot information is collected (**Fig. 1-11E**).
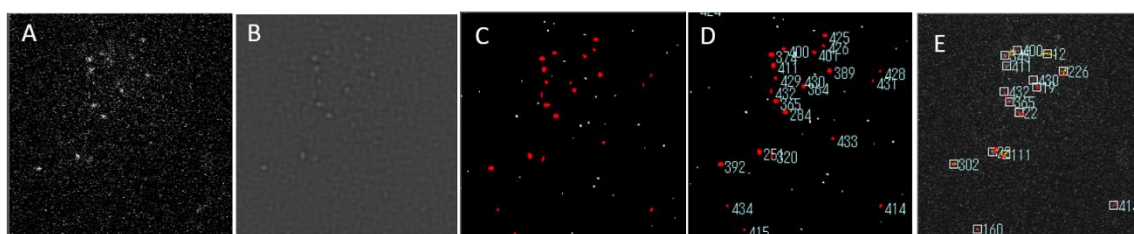
Fig. 1-11. Representative results of single molecule tracking. (A) A raw image sequence. (B) Noise reduction. (C) Spot identification based on the fluorescence intensity and the area. (D) Particle tracking. (E) Quantification of spot characteristics such as the fluorescence intensity, location, and duration.

1-6. Purpose of the present study.

FPR1 is a potential target for drug discovery of SJS/TEN and other inflammatory diseases. Many researchers have developed agonists and inhibitors for FPR1. However, the compounds have not shown satisfactory biological responses. Recent studies have demonstrated that the signal transduction patterns of GPCRs can be modulated temporally and spatially by many factors, including ligand bias and oligomer formation. To control the signal transduction of FPR1 specifically in physiological conditions, deeper understanding of molecular mechanisms of FPR1 signal transduction would be required. Here, I established assay systems to quantify multiple signaling pathways, including G protein and β-arresin, with temporal information. The experimental conditions were carefully optimized to obtain the efficacy and kinetics information that can be directly compared with each other. In addition, I visualized oligomerization states of FPR1 with bulk and single molecule microscopy techniques to reveal the functional roles of oligomer and cluster formation of FPR1. It was the first research to demonstrate the distribution of the functional heterogeneity of FPR1 dependent on the complex size in living cells. Oligomerization-induced signal control may provide a new approach for designing signal specific drug discovery.

1-7. References

(1)   Isberg, V.; Mordalski, S.; Munk, C.; Rataj, K.; Harpsøe, K.; Hauser, A. S.; Vroling, B.; Bojarski, A. J.; Vriend, G.; Gloriam, D. E. GPCRdb: An Information System for G Protein-Coupled Receptors. *Nucleic Acids Res.* **2016**, *44* (D1), D356–D364. https://doi.org/10.1093/nar/gkv1178.

(2)   García-Nafría, J.; Tate, C. G. Cryo-EM Structures of GPCRs Coupled to G s , G i and G O. *Mol. Cell. Endocrinol.* **2019**, *488* (October 2018), 1–13. https://doi.org/10.1016/j.mce.2019.02.006.

(3)   Zhuang, Y.; Liu, H.; Edward Zhou, X.; Kumar Verma, R.; de Waal, P. W.; Jang, W.; Xu, T. H.; Wang, L.; Meng, X.; Zhao, G.; et al. Structure of Formylpeptide Receptor 2-Gi Complex Reveals Insights into Ligand Recognition and Signaling. *Nat. Commun.* **2020**, *11* (1), 1–12. https://doi.org/10.1038/s41467-020-14728-9.

(4)   McCudden, C. R.; Hains, M. D.; Kimple, R. J.; Siderovski, D. P.; Willard, F. S. G-Protein Signaling: Back to the Future. *Cell. Mol. Life Sci.* **2005**, *62*, 551–577. https://doi.org/10.1007/s00018-004-4462-3.

(5)   Gurevich, V. V.; Gurevich, E. V. GPCRs and Signal Transducers: Interaction Stoichiometry. *Trends Pharmacol. Sci.* **2018**, *39* (7), 672–684. https://doi.org/10.1016/j.tips.2018.04.002.

(6)   Aicart-Ramos, C.; Valero, R. A.; Rodriguez-Crespo, I. Protein Palmitoylation and Subcellular Trafficking. *Biochim. Biophys. Acta - Biomembr.* **2011**, *1808* (12), 2981–2994. https://doi.org/10.1016/j.bbamem.2011.07.009.

(7)   Inoue, A.; Raimondi, F.; Kadji, F. M. N.; Singh, G.; Kishi, T.; Uwamizu, A.; Ono, Y.; Shinjo, Y.; Ishida, S.; Arang, N.; et al. Illuminating G-Protein-Coupling Selectivity of GPCRs. *Cell* **2019**, *177* (7), 1933—1947.e25. https://doi.org/10.1016/j.cell.2019.04.044.

(8)   Lehmann, D. M.; Seneviratne, A. M. P. B.; Smrcka, A. V. Small Molecule Disruption of G Protein Beta Gamma Subunit Signaling Inhibits Neutrophil Chemotaxis and Inflammation. *Mol. Pharmacol.* **2008**, *73* (2), 410–418. https://doi.org/10.1124/mol.107.041780.

(9)   Shukla, A. K.; Westfield, G. H.; Xiao, K.; Reis, R. I.; Huang, L.-Y.; Tripathi-Shukla, P.; Qian, J.; Li, S.; Blanc, A.; Oleskie, A. N.; et al. Visualization of Arrestin Recruitment by a G-Protein-Coupled Receptor. *Nature* **2014**, *512* (7513), 218–222. https://doi.org/10.1038/nature13430.

(10)   Tsvetanova, N. G.; Irannejad, R.; von Zastrow, M. G Protein-Coupled Receptor (GPCR) Signaling via Heterotrimeric G Proteins from Endosomes. *J. Biol. Chem.* **2015**, *290* (11), 6689–6696. https://doi.org/10.1074/jbc.R114.617951.

(11)   Shonberg, J.; Lopez, L.; Scammells, P. J.; Christopoulos, A.; Capuano, B.; Lane, J. R. Biased Agonism at G Protein-Coupled Receptors: The Promise and the Challenges--a Medicinal Chemistry Perspective. *Med. Res. Rev.* **2014**, *34* (6), 1286–1330. https://doi.org/10.1002/med.21318.

(12)   Ferré, S. The GPCR Heterotetramer: Challenging Classical Pharmacology. *Trends Pharmacol. Sci.* **2015**, *36* (3), 145–152. https://doi.org/10.1016/j.tips.2015.01.002.

(13)   Gomes, I.; Ayoub, M. A.; Fujita, W.; Jaeger, W. C.; Pfleger, K. D. G.; Devi, L. A. G Protein-
         Coupled Receptor Heteromers. *Annu. Rev. Pharmacol. Toxicol.* **2016**, *56*, 403–425.
         https://doi.org/10.1146/annurev-pharmtox-011613-135952.

(14)   Wettschureck, N.; Offermanns, S. Mammalian G Proteins and Their Cell Type Specific
         Functions. *Physiol. Rev.* **2005**, *85* (4), 1159–1204. https://doi.org/10.1152/physrev.00003.2005.

(15)   Denis, C.; Sauliere, A.; Galandrin, S.; Senard, J.-M.; Gales, C. Probing Heterotrimeric G Protein
         Activation: Applications to Biased Ligands. *Curr. Pharm. Des.* **2012**, *18* (2), 128–144.
         https://doi.org/10.2174/138161212799040466.

(16)   Rasmussen, S. G. F.; DeVree, B. T.; Zou, Y.; Kruse, A. C.; Chung, K. Y.; Kobilka, T. S.; Thian,
         F. S.; Chae, P. S.; Pardon, E.; Calinski, D.; et al. Crystal Structure of the B2 Adrenergic Receptor-
         Gs Protein Complex. *Nature* **2011**, *477* (7366), 549–555. https://doi.org/10.1038/nature10361.

(17)   Flock, T.; Ravarani, C. N. J.; Sun, D.; Venkatakrishnan, A. J.; Kayikci, M.; Tate, C. G.;
         Veprintsev, D. B.; Babu, M. M. Universal Allosteric Mechanism for Gα Activation by GPCRs.
         Nature **2015**, *524* (7564), 173–179. https://doi.org/10.1038/nature14663.

(18)   Flock, T.; Hauser, A. S.; Lund, N.; Gloriam, D. E.; Balaji, S.; Babu, M. M. Selectivity
         Determinants of GPCR-G-Protein Binding. *Nature* **2017**, *545* (7654), 317–322.
         https://doi.org/10.1038/nature22070.

(19)   Cahill, T. J. 3rd; Thomsen, A. R. B.; Tarrasch, J. T.; Plouffe, B.; Nguyen, A. H.; Yang, F.;
         Huang, L.-Y.; Kahsai, A. W.; Bassoni, D. L.; Gavino, B. J.; et al. Distinct Conformations of
         GPCR-β-Arrestin Complexes Mediate Desensitization, Signaling, and Endocytosis. *Proc. Natl.
         Acad. Sci. U. S. A.* **2017**, *114* (10), 2562–2567. https://doi.org/10.1073/pnas.1701529114.

(20)   Takenouchi, O.; Yoshimura, H.; Ozawa, T. Unique Roles of β-Arrestin in GPCR Trafficking
         Revealed by Photoinducible Dimerizers. *Sci. Rep.* **2018**, *8* (1), 677.
         https://doi.org/10.1038/s41598-017-19130-y.

(21)   Eichel, K.; Jullié, D.; von Zastrow, M. β-Arrestin Drives MAP Kinase Signalling from Clathrin-
         Coated Structures after GPCR Dissociation. *Nat. Cell Biol.* **2016**, *18* (3), 303–310.
         https://doi.org/10.1038/ncb3307.

(22)   Eichel, K.; Jullié, D.; Barsi-Rhyne, B.; Latorraca, N. R.; Masureel, M.; Sibarita, J.-B.; Dror, R.
         O.; von Zastrow, M. Catalytic Activation of β-Arrestin by GPCRs. *Nature* **2018**, *557* (7705),
         381–386. https://doi.org/10.1038/s41586-018-0079-1.

(23)   Tamman, H.; Van Nerom, K.; Takada, H.; Vandenberk, N.; Scholl, D.; Polikanov, Y.; Hofkens,
         J.; Talavera, A.; Hauryliuk, V.; Hendrix, J.; et al. A Nucleotide-Switch Mechanism Mediates
         Opposing Catalytic Activities of Rel Enzymes. *Nat. Chem. Biol.* **2020**, *16* (8), 834–840.
         https://doi.org/10.1038/s41589-020-0520-2.

(24)   Stoeber, M.; Jullié, D.; Lobingier, B. T.; Laeremans, T.; Steyaert, J.; Schiller, P. W.; Manglik, A.;
         von Zastrow, M. A Genetically Encoded Biosensor Reveals Location Bias of Opioid Drug

Action. *Neuron* **2018**, *98* (5), 963-976.e5. https://doi.org/10.1016/j.neuron.2018.04.021.

(25)   Weinberg, Z. Y.; Zajac, A. S.; Phan, T.; Shiwarski, D. J.; Puthenveedu, M. A. Sequence-Specific
       Regulation of Endocytic Lifetimes Modulates Arrestin-Mediated Signaling at the µ Opioid
       Receptor. *Mol. Pharmacol.* **2017**, *91* (4), 416–427. https://doi.org/10.1124/mol.116.106633.

(26)   Shen, A.; Nieves-Cintron, M.; Deng, Y.; Shi, Q.; Chowdhury, D.; Qi, J.; Hell, J. W.; Navedo, M.
       F.; Xiang, Y. K. Functionally Distinct and Selectively Phosphorylated GPCR Subpopulations Co-
       Exist in a Single Cell. *Nat. Commun.* **2018**, *9* (1), 1050. https://doi.org/10.1038/s41467-018-
       03459-7.

(27)   Ferré, S.; Bonaventura, J.; Zhu, W.; Hatcher-Solis, C.; Taura, J.; Quiroz, C.; Cai, N.-S.; Moreno,
       E.; Casadó-Anguera, V.; Kravitz, A. V; et al. Essential Control of the Function of the
       Striatopallidal Neuron by Pre-Coupled Complexes of Adenosine A(2A)-Dopamine D(2) Receptor
       Heterotetramers and Adenylyl Cyclase. *Front. Pharmacol.* **2018**, *9*, 243.
       https://doi.org/10.3389/fphar.2018.00243.

(28)   Inoue, A.; Ishiguro, J.; Kitamura, H.; Arima, N.; Okutani, M.; Shuto, A.; Higashiyama, S.;
       Ohwada, T.; Arai, H.; Makide, K.; et al. TGFα Shedding Assay: An Accurate and Versatile
       Method for Detecting GPCR Activation. *Nat. Methods* **2012**, *9* (10), 1021–1029.
       https://doi.org/10.1038/nmeth.2172.

(29)   Lieb, S.; Michaelis, S.; Plank, N.; Bernhardt, G.; Buschauer, A.; Wegener, J. Label-Free Analysis
       of GPCR-Stimulation: The Critical Impact of Cell Adhesion. *Pharmacol. Res.* **2016**, *108*, 65–74.
       https://doi.org/10.1016/j.phrs.2016.04.026.

(30)   Bourassa, P.; Tudashki, H. B.; Pineyro, G.; Grandbois, M.; Gendron, L.; Physiologie, D. De;
       Pharmacologie, H. B. T.; Psychiatrie, G. P.; De, C. Label-Free Monitoring of m -Opioid Receptor
       – Mediated Signaling. **2014**, No. August, 138–149.

(31)   Liu, J. J.; Horst, R.; Katritch, V.; Stevens, R. C.; Wuthrich, K. Biased Signaling Pathways in   2-
       Adrenergic Receptor Characterized by 19F-NMR. *Science (80-.).* **2012**, *335* (2012), 1106–1110.
       https://doi.org/10.1126/science.1215802.

(32)   Ye, L.; Van Eps, N.; Zimmer, M.; Ernst, O. P.; Prosser, R. S. Activation of the A2A Adenosine
       G-Protein-Coupled Receptor by Conformational Selection. *Nature* **2016**, *533* (7602), 265–268.
       https://doi.org/10.1038/nature17668.

(33)   Schönegge, A.-M.; Gallion, J.; Picard, L.-P.; Wilkins, A. D.; Le Gouill, C.; Audet, M.; Stallaert,
       W.; Lohse, M. J.; Kimmel, M.; Lichtarge, O.; et al. Evolutionary Action and Structural Basis of
       the Allosteric Switch Controlling β(2)AR Functional Selectivity. *Nat. Commun.* **2017**, *8* (1),
       2169. https://doi.org/10.1038/s41467-017-02257-x.

(34)   Baltos, J.-A.; Gregory, K. J.; White, P. J.; Sexton, P. M.; Christopoulos, A.; May, L. T.
       Quantification of Adenosine A(1) Receptor Biased Agonism: Implications for Drug Discovery.
       Biochem. Pharmacol. **2016**, *99*, 101–112. https://doi.org/10.1016/j.bcp.2015.11.013.

(35) Pedersen, M. F.; Wróbel, T. M.; Märcher-Rørsted, E.; Pedersen, D. S.; Møller, T. C.; Gabriele, F.; Pedersen, H.; Matosiuk, D.; Foster, S. R.; Bouvier, M.; et al. Biased Agonism of Clinically Approved μ-Opioid Receptor Agonists and TRV130 Is Not Controlled by Binding and Signaling Kinetics. *Neuropharmacology* **2020**, *166*, 107718. https://doi.org/10.1016/j.neuropharm.2019.107718.

(36) Blättermann, S.; Peters, L.; Ottersbach, P. A.; Bock, A.; Konya, V.; Weaver, C. D.; Gonzalez, A.; Schröder, R.; Tyagi, R.; Luschnig, P.; et al. A Biased Ligand for OXE-R Uncouples Gα and Gβγ Signaling within a Heterotrimer. *Nat. Chem. Biol.* **2012**, *8* (may), 631–638. https://doi.org/10.1038/nchembio.962.

(37) Rajagopal, S.; Ahn, S.; Rominger, D. H.; Gowen-MacDonald, W.; Lam, C. M.; Dewire, S. M.; Violin, J. D.; Lefkowitz, R. J. Quantifying Ligand Bias at Seven-Transmembrane Receptors. *Mol. Pharmacol.* **2011**, *80* (3), 367–377. https://doi.org/10.1124/mol.111.072801.

(38) Ambrosio, M.; Lohse, M. J. Nonequilibrium Activation of a G-Protein-Coupled Receptor. *Mol. Pharmacol.* **2012**, *81* (6), 770–777. https://doi.org/10.1124/mol.112.077693.

(39) Bodmann, E.-L.; Wolters, V.; Bünemann, M. Dynamics of G Protein Effector Interactions and Their Impact on Timing and Sensitivity of G Protein-Mediated Signal Transduction. *Eur. J. Cell Biol.* **2015**, *94* (7–9), 415–419. https://doi.org/10.1016/j.ejcb.2015.06.004.

(40) Weiß, E.; Kretschmer, D. Formyl-Peptide Receptors in Infection, Inflammation, and Cancer. *Trends Immunol.* **2018**, *39* (10), 815–829. https://doi.org/10.1016/j.it.2018.08.005.

(41) Ye, R. D.; Boulay, F.; Wang, J. M.; Dahlgren, C.; Gerard, C.; Parmentier, M.; Serhan, C. N.; Murphy, P. M. International Union of Basic and Clinical Pharmacology. LXXIII. Nomenclature for the Formyl Peptide Receptor (FPR) Family. *Pharmacol. Rev.* **2009**, *61* (2), 119–161. https://doi.org/10.1124/pr.109.001578.

(42) Filep, J. G.; Sekheri, M.; El Kebir, D. Targeting Formyl Peptide Receptors to Facilitate the Resolution of Inflammation. *Eur. J. Pharmacol.* **2018**, *833*, 339–348. https://doi.org/10.1016/j.ejphar.2018.06.025.

(43) Osei-Owusu, P.; Charlton, T. M.; Kim, H. K.; Missiakas, D.; Schneewind, O. FPR1 Is the Plague Receptor on Host Immune Cells. *Nature* **2019**, *574* (7776), 57–62. https://doi.org/10.1038/s41586-019-1570-z.

(44) Alessi, M.-C.; Cenac, N.; Si-Tahar, M.; Riteau, B. FPR2: A Novel Promising Target for the Treatment of Influenza. *Front. Microbiol.* **2017**, *8*, 1719. https://doi.org/10.3389/fmicb.2017.01719.

(45) Saito, N.; Qiao, H.; Yanagi, T.; Shinkuma, S.; Nishimura, K.; Suto, A.; Fujita, Y.; Suzuki, S.; Nomura, T.; Nakamura, H.; et al. An Annexin A1-FPR1 Interaction Contributes to Necroptosis of Keratinocytes in Severe Cutaneous Adverse Drug Reactions. *Sci. Transl. Med.* **2014**, *6*, 245ra95. https://doi.org/10.1126/scitranslmed.3008227.

(46)   Hasegawa, A.; Abe, R. Recent Advances in Managing and Understanding Stevens-Johnson Syndrome and Toxic Epidermal Necrolysis. *F1000Research* **2020**, *9*. https://doi.org/10.12688/f1000research.24748.1.

(47)   Pinilla, C.; Edwards, B. S.; Appel, J. R.; Yates-Gibbins, T.; Giulianotti, M. a; Medina-Franco, J. L.; Young, S. M.; Santos, R. G.; Sklar, L. a; Houghten, R. a. Selective Agonists and Antagonists of Formylpeptide Receptors: Duplex Flow Cytometry and Mixture-Based Positional Scanning Libraries. *Mol. Pharmacol.* **2013**, *84*, 314–324. https://doi.org/10.1124/mol.113.086595.

(48)   Schepetkin, I. A.; Khlebnikov, A. I.; Kirpotina, L. N.; Quinn, M. T. Antagonism of Human Formyl Peptide Receptor 1 with Natural Compounds and Their Synthetic Derivatives. *Int. Immunopharmacol.* **2016**, *37*, 43–58. https://doi.org/10.1016/j.intimp.2015.08.036.

(49)   Schepetkin, I. A.; Kirpotina, L. N.; Khlebnikov, A. I.; Cheng, N.; Ye, R. D.; Quinn, M. T. Antagonism of Human Formyl Peptide Receptor 1 (FPR1) by Chromones and Related Isoflavones. *Biochem. Pharmacol.* **2014**, *1*. https://doi.org/10.1016/j.bcp.2014.09.027.

(50)   He, H.-Q.; Ye, R. D. The Formyl Peptide Receptors: Diversity of Ligands and Mechanism for Recognition. *Molecules* **2017**, *22* (3). https://doi.org/10.3390/molecules22030455.

(51)   Ye, R. D.; Cavanagh, S. L.; Quehenberger, O.; Prossnitz, E. R.; Cochrane, C. G. Isolation of a CDNA That Encodes a Novel Granulocyte N-Formyl Peptide Receptor. *Biochem. Biophys. Res. Commun.* **1992**, *184*, 582–589. https://doi.org/10.1016/0006-291X(92)90629-Y.

(52)   Baek, S. H.; Seo, J. K.; Chae, C. B.; Suh, P. G.; Ryu, S. H. Identification of the Peptides That Stimulate the Phosphoinositide Hydrolysis in Lymphocyte Cell Lines from Peptide Libraries. *J. Biol. Chem.* **1996**, *271* (14), 8170–8175. https://doi.org/10.1074/jbc.271.14.8170.

(53)   Schepetkin, I. a; Kirpotina, L. N.; Khlebnikov, A. I.; Quinn, M. T. High-Throughput Screening for Small-Molecule Activators of Neutrophils: Identification of Novel N-Formyl Peptide Receptor Agonists. *Mol. Pharmacol.* **2007**, *71* (4), 1061–1074. https://doi.org/10.1124/mol.106.033100.

(54)   Deora, G. S.; Qin, C. X.; Vecchio, E. A.; Debono, A. J.; Priebbenow, D. L.; Brady, R. M.; Beveridge, J.; Teguh, S. C.; Deo, M.; May, L. T.; et al. Substituted Pyridazin-3(2 H)-Ones as Highly Potent and Biased Formyl Peptide Receptor Agonists. *J. Med. Chem.* **2019**, *62* (10), 5242–5248. https://doi.org/10.1021/acs.jmedchem.8b01912.

(55)   Cilibrizzi, A.; Quinn, M. T.; Kirpotina, L. N.; Schepetkin, I. A.; Holderness, J.; Ye, R. D.; Rabiet, M.-J.; Biancalani, C.; Cesari, N.; Graziano, A.; et al. 6-Methyl-2,4-Disubstituted Pyridazin-3(2H)-Ones: A Novel Class of Small-Molecule Agonists for Formyl Peptide Receptors. *J. Med. Chem.* **2009**, *52* (16), 5044–5057. https://doi.org/10.1021/jm900592h.

(56)   Unitt, J.; Fagura, M.; Phillips, T.; King, S.; Perry, M.; Morley, A.; MacDonald, C.; Weaver, R.; Christie, J.; Barber, S.; et al. Discovery of Small Molecule Human FPR1 Receptor Antagonists. *Bioorg. Med. Chem. Lett.* **2011**, *21* (10), 2991–2997. https://doi.org/10.1016/j.bmcl.2011.03.049.

(57)   Arterburn, J. B.; Oprea, T. I.; Prossnitz, E. R.; Edwards, B. S.; Sklar, L. A. Discovery of Selective
Probes and Antagonists for G-Protein-Coupled Receptors FPR/FPRL1 and GPR30. *Curr. Top.
Med. Chem.* **2009**, *9* (13), 1227–1236. https://doi.org/10.2174/156802609789753608.

(58)   Prasher, D. C.; Eckenrode, V. K.; Ward, W. W.; Prendergast, F. G.; Cormier, M. J. Primary
Structure of the Aequorea Victoria Green-Fluorescent Protein. *Gene* **1992**, *111* (2), 229–233.
https://doi.org/10.1016/0378-1119(92)90691-h.

(59)   Tsien, R. Y. The Green Fluorescent Protein. *Annu. Rev. Biochem.* **1998**, *67*, 509–544.
https://doi.org/10.1146/annurev.biochem.67.1.509.

(60)   Tomosugi, W.; Matsuda, T.; Tani, T.; Nemoto, T.; Kotera, I.; Saito, K.; Horikawa, K.; Nagai, T.
An Ultramarine Fluorescent Protein with Increased Photostability and PH Insensitivity. *Nat.
Methods* **2009**, *6* (5), 351–353. https://doi.org/10.1038/nmeth.1317.

(61)   Ormö, M.; Cubitt, A. B.; Kallio, K.; Gross, L. A.; Tsien, R. Y.; Remington, S. J. Crystal Structure
of the Aequorea Victoria Green Fluorescent Protein. *Science* **1996**, *273* (5280), 1392–1395.
https://doi.org/10.1126/science.273.5280.1392.

(62)   Mishin, A. S.; Subach, F. V; Yampolsky, I. V; King, W.; Lukyanov, K. A.; Verkhusha, V. V. The
First Mutant of the Aequorea Victoria Green Fluorescent Protein That Forms a Red
Chromophore. *Biochemistry* **2008**, *47* (16), 4666–4673. https://doi.org/10.1021/bi702130s.

(63)   Miyawaki, A.; Shcherbakova, D. M.; Verkhusha, V. V. Red Fluorescent Proteins: Chromophore
Formation and Cellular Applications. *Curr. Opin. Struct. Biol.* **2012**, *22* (5), 679–688.
https://doi.org/10.1016/j.sbi.2012.09.002.

(64)   Pakhomov, A. A.; Martynov, V. I. GFP Family: Structural Insights into Spectral Tuning. *Chem.
Biol.* **2008**, *15* (8), 755–764. https://doi.org/10.1016/j.chembiol.2008.07.009.

(65)   de Wet, J. R.; Wood, K. V; Helinski, D. R.; DeLuca, M. Cloning of Firefly Luciferase CDNA and
the Expression of Active Luciferase in Escherichia Coli. *Proc. Natl. Acad. Sci. U. S. A.* **1985**, *82*
(23), 7870–7873. https://doi.org/10.1073/pnas.82.23.7870.

(66)   Matthews, J. C.; Hori, K.; Cormier, M. J. Purification and Properties of Renilla Reniformis
Luciferase. *Biochemistry* **1977**, *16* (1), 85–91. https://doi.org/10.1021/bi00620a014.

(67)   Chopra, A. Gaussia Princeps Luciferase. In *Molecular Imaging and Contrast Agent Database
(MICAD). Bethesda (MD)*; Bethesda (MD), 2004; p PMID: 20641352.

(68)   Hall, M. P.; Unch, J.; Binkowski, B. F.; Valley, M. P.; Butler, B. L.; Wood, M. G.; Otto, P.;
Zimmerman, K.; Vidugiris, G.; Machleidt, T.; et al. Engineered Luciferase Reporter from a Deep
Sea Shrimp Utilizing a Novel Imidazopyrazinone Substrate. *ACS Chem. Biol.* **2012**, *7* (11), 1848–
1857. https://doi.org/10.1021/cb3002478.

(69)   Rowe, L.; Dikici, E.; Daunert, S. Engineering Bioluminescent Proteins: Expanding Their
Analytical Potential. *Anal. Chem.* **2009**, *81* (21), 8662–8668. https://doi.org/10.1021/ac9007286.

(70)   Viviani, V. R.; Silva, A. C.; Perez, G. L.; Santelli, R. V; Bechara, E. J.; Reinach, F. C. Cloning

and Molecular Characterization of the CDNA for the Brazilian Larval Click-Beetle Pyrearinus Termitilluminans Luciferase. *Photochem. Photobiol.* **1999**, *70* (2), 254–260. https://doi.org/10.1562/0031-8655(1999)070<0254:camcot>2.3.co;2.

(71)   Ugarova, N. N.; Brovko, L. Y. Protein Structure and Bioluminescent Spectra for Firefly Bioluminescence. *Luminescence* **2002**, *17* (5), 321–330. https://doi.org/10.1002/bio.688.

(72)   McCutcheon, D. C.; Paley, M. A.; Steinhardt, R. C.; Prescher, J. A. Expedient Synthesis of Electronically Modified Luciferins for Bioluminescence Imaging. *J. Am. Chem. Soc.* **2012**, *134* (18), 7604–7607. https://doi.org/10.1021/ja301493d.

(73)   Nishiguchi, T.; Yamada, T.; Nasu, Y.; Ito, M.; Yoshimura, H.; Ozawa, T. Development of Red-Shifted Mutants Derived from Luciferase of Brazilian Click Beetle Pyrearinus Termitilluminans. *J. Biomed. Opt.* **2015**, *20* (10), 101205. https://doi.org/10.1117/1.JBO.20.10.101205.

(74)   Kuchimaru, T.; Iwano, S.; Kiyama, M.; Mitsumata, S.; Kadonosono, T.; Niwa, H.; Maki, S.; Kizaka-Kondoh, S. A Luciferin Analogue Generating Near-Infrared Bioluminescence Achieves Highly Sensitive Deep-Tissue Imaging. *Nat. Commun.* **2016**, *7*, 11856. https://doi.org/10.1038/ncomms11856.

(75)   Kawamura, G.; Hattori, M.; Takamatsu, K.; Tsukada, T.; Ninomiya, Y.; Benjamin, I.; Sassone-Corsi, P.; Ozawa, T.; Tamaru, T. Cooperative Interaction among BMAL1, HSF1, and P53 Protects Mammalian Cells from UV Stress. *Commun. Biol.* **2018**, *1*, 204. https://doi.org/10.1038/s42003-018-0209-1.

(76)   Cronan, J. E. J. Biotination of Proteins in Vivo. A Post-Translational Modification to Label, Purify, and Study Proteins. *J. Biol. Chem.* **1990**, *265* (18), 10327–10333.

(77)   Griffin, B. A.; Adams, S. R.; Tsien, R. Y. Specific Covalent Labeling of Recombinant Protein Molecules inside Live Cells. *Science* **1998**, *281* (5374), 269–272. https://doi.org/10.1126/science.281.5374.269.

(78)   Keppler, A.; Gendreizig, S.; Gronemeyer, T.; Pick, H.; Vogel, H.; Johnsson, K. A General Method for the Covalent Labeling of Fusion Proteins with Small Molecules in Vivo. *Nat. Biotechnol.* **2003**, *21* (1), 86–89. https://doi.org/10.1038/nbt765.

(79)   Gautier, A.; Juillerat, A.; Heinis, C.; Corrêa, I. R. J.; Kindermann, M.; Beaufils, F.; Johnsson, K. An Engineered Protein Tag for Multiprotein Labeling in Living Cells. *Chem. Biol.* **2008**, *15* (2), 128–136. https://doi.org/10.1016/j.chembiol.2008.01.007.

(80)   Los, G. V.; Encell, L. P.; McDougall, M. G.; Hartzell, D. D.; Karassina, N.; Zimprich, C.; Wood, M. G.; Learish, R.; Ohana, R. F.; Urh, M.; et al. HaloTag: A Novel Protein Labeling Technology for Cell Imaging and Protein Analysis. *ACS Chem. Biol.* **2008**, *3* (6), 373–382. https://doi.org/10.1021/cb800025k.

(81)   Chen, Y.; Clouthier, C. M.; Tsao, K.; Strmiskova, M.; Lachance, H.; Keillor, J. W. Coumarin-Based Fluorogenic Probes for No-Wash Protein Labeling. *Angew. Chem. Int. Ed. Engl.* **2014**, *53*

(50), 13785–13788. https://doi.org/10.1002/anie.201408015.

(82)   Hirayama, S.; Hori, Y.; Benedek, Z.; Suzuki, T.; Kikuchi, K. Fluorogenic Probes Reveal a Role of GLUT4 N-Glycosylation in Intracellular Trafficking. *Nat. Chem. Biol.* **2016**, *12* (10), 853–859. https://doi.org/10.1038/nchembio.2156.

(83)   Plamont, M.-A.; Billon-Denis, E.; Maurin, S.; Gauron, C.; Pimenta, F. M.; Specht, C. G.; Shi, J.; Quérard, J.; Pan, B.; Rossignol, J.; et al. Small Fluorescence-Activating and Absorption-Shifting Tag for Tunable Protein Imaging in Vivo. *Proc. Natl. Acad. Sci. U. S. A.* **2016**, *113* (3), 497–502. https://doi.org/10.1073/pnas.1513094113.

(84)   Jaqaman, K.; Loerke, D.; Mettlen, M.; Kuwata, H.; Grinstein, S.; Schmid, S. L.; Danuser, G. Robust Single-Particle Tracking in Live-Cell Time-Lapse Sequences. *Nat. Methods* **2008**, *5* (8), 695–702. https://doi.org/10.1038/nmeth.1237.

(85)   Tinevez, J.-Y.; Perry, N.; Schindelin, J.; Hoopes, G. M.; Reynolds, G. D.; Laplantine, E.; Bednarek, S. Y.; Shorte, S. L.; Eliceiri, K. W. TrackMate: An Open and Extensible Platform for Single-Particle Tracking. *Methods* **2017**, *115*, 80–90. https://doi.org/10.1016/j.ymeth.2016.09.016.

(86)   Fujiwara, T.; Ritchie, K.; Murakoshi, H.; Jacobson, K.; Kusumi, A. Phospholipids Undergo Hop Diffusion in Compartmentalized Cell Membrane. *J. Cell Biol.* **2002**, *157* (6), 1071–1081. https://doi.org/10.1083/jcb.200202050.

Chapter 2

Quantitative evaluation of time dependent FPR1 signaling

2-1. Introduction

FPR1 is mainly expressed in neutrophils and involved in inflammatory responses. Activation of FPR1 triggers clearance of pathogens, and induces apoptosis of malignant tumor cells[1]. However, abnormal activation of FPR1 triggers necroptotic cell deaths of healthy skin cells, causing severe drug eruption[2]. Activation of the related receptor, FPR2, induces both pro- and anti-inflammatory responses dependent on ligands and following conformational changes of FPR2[3]. These bi-directional functions of formyl peptide receptors suggest the need for subtype-specific and signal-specific drug developments. To avoid unwanted side effects, biased ligands are desired[4], but only two biased agonists have been reported for FPR1 to date[5,6]. Another characteristic of FPR1 is the slow ligand binding and dissociation rate[7]. Chemoattractant receptors, including FPR1 and cAMP receptors (cARs), sense wide concentration ranges of ligands to induce cell polarization and migration[8,9]. The slow ligand binding reaction may enable the responses for the wide concentration ranges by dynamically changing apparent sensitivity[10]. To understand the signal transduction of FPR1, the kinetics of signal transductions for each signal pathway, including G protein and β-arrestin pathways, should be assessed.

  Here, I established live-cell quantitative and real-time assays for monitoring FPR1 signal transduction events. The signal events observed in the present study included ligand binding, G protein activation, cAMP signals, and β-arrestin recruitment (**Fig. 2-1**). The presently established assay systems for FPR1 would be useful to identify FPR1 specific ligands and evaluate its agonistic or inhibitory effects on FPR1 quantitatively.
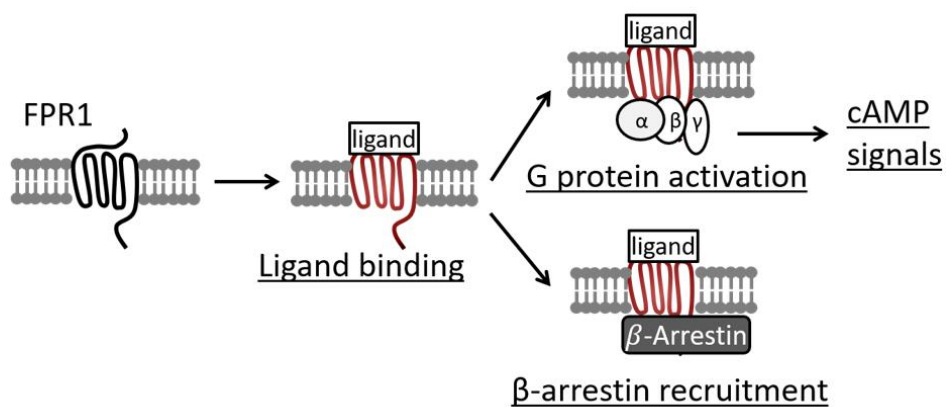

Fig. 2-1. Schematic diagram of signal transduction events after ligand stimulation of FPR1.

2-2. Materials and Methods

2-2-1. Materials

Dulbecco's Modified Eagle Medium (DMEM) and Trypsin were purchased from Nacalai Tesque Inc. Fetal bovine serum (FBS), reduced serum medium (Opti-MEM ^{TM}), penicillin streptomycin (Pen Strep), phosphate buffered saline (PBS(-)), and Hank's balanced salt solution (HBSS) were from Gibco Inds. Inc. G418 sulfate, Zeocin^{TM}, and Formyl-Nle-Leu-Phe-Nle-Tyr-Lys fluorescein derivative (fNLFNYK-FITC) were purchased from Invitrogen Corp. *Trans*IT®-LT1 was from Mirus Bio LLC. Formyl-methionyl-leucyl-phenylalanine (fMLP), cyclosporin H (CysH), and WKYMVm trifluoroacetate salt (WKYMVm) were purchased from Sigma-Aldrich Corp. Methionine benzimidazole 6 (N-[1-[1-(1H-benzimidazol-2-yl)-3-methylsulfanylpropyl]-5-ethoxy-3-methyl-1-benzofuran-2-carboxamide) was purchased from Enamine Ltd. DMSO, D-luciferin potassium salt, HEPES, and forskolin were purchased from Fujifilm – Wako Pure Chemical Corp. 96 well polystyrene assay plate (white) was purchased from Coster®.

2-2-2. Plasmid constructs

FRET-based G protein probe (Gβ-2A-cpV-Gγ2-IRES-Gαi3-mTq2[11]) was purchased from Addgene. A yellow fluorescent protein, circular permutated Venus (cpV), and a cyan fluorescent protein, mTurquoise2 (mTq2), were attached respectively to G protein γ2 and αi3 subunits. Luminescence-based cAMP probe (GloSensor) was purchased from Promega Corporation. The other probe plasmids were constructed on mammalian expression vectors, pcDNA3.1 myc/His(B) and pcDNA4 V5/His(B). The vectors, pcDNA3.1 and pcDNA4, respectively, have epitope tags of a myc-tag and a V5 tag at the C-terminus. In the binding assay, FPR1 in pcDNA4 was stably transfected in HEK293 cells. In β-arrestin assay, FPR1-ElucC in pcDNA4 and ElucN-ARRB1 in pcDNA3.1 were stably transfected in HEK293 cells. FPR1 was fused at its C-terminus with the C-terminal fragment of a click beetle-derived luciferase, Eluc, with 20 amino acids of a GS linker, whereas β-arrestin was fused at its N-terminus with the N-terminal fragment of Eluc with 4 amino acids of a GS linker. As previously reported, the ElucC fragment starts at the 394th residue of the original luciferase and the ElucN ends at the 415th residue[12,13]. In the cAMP assay, the FPR1 in pcDNA4 and the GloSensor were stably transfected in HEK293 cells. In the FRET assay, the FPR1 in pcDNA4, SNAP-FPR1 or Halo-FPR1 in pc DNA4 were transiently co-transfected with the FRET-based G protein probe in HEK293 cells. The probe design of SNAP-FPR1 is described in detail in Chapter 3. All the plasmids were verified using DNA sequencing (Eurofins Sequencing Service).

2-2-3. Cell culture

HEK293 cells were grown in DMEM supplemented with 10% FBS, 100 μg/mL streptomycin and 100 U/mL penicillin at 37°C in 5% CO_2 unless otherwise mentioned. Stable cell lines were cultured in the

medium supplemented with appropriate combinations of antibiotics; FPR1 (pcDNA4) with 0.05 mg/mL Zeocin, FPR1×GloSensor with 0.05 mg/mL Zeocin and 0.2 mg/mL Hygromycin, FPR1-ElucC×ElucN-ARRB1 with 0.8 mg/mL G418 and 0.05 mg/mL Zeocin. Transfection of the cells were performed with *Trans*IT-LT following the manufacturer's protocol. In brief, plasmid vectors (1 μg each) were diluted with 200 μL reduced serum medium (Opti-MEM). Into the mix, 6 μL transfection reagent (*Trans*IT-LT) was gently injected. The reaction mix incubated at room temperature for 15 min was added to the cells on a cell culture dish (φ6 cm) cultured with 4 mL of the medium. The amount of the mixture was arranged in proportion to the total amount of the medium.

2-2-4. Flow cytometry

FPR1 (pcDNA4) in HEK293 cells cultured on 10 cm dishes were stripped with Versene (PBS(-) supplemented with 0.5 mM EDTA(Na$_4$)), collected as a pellet by centrifugation, and resuspended in PBS(-). Note that trypsin treatment was avoided not to digest the membrane localized FPR1. Aliquots of the cells ($0.3–1.0 \times 10^6$ cells in 1 mL PBS(-)) were treated with the test compounds for ten minutes. After the addition of fNLFNYK-FITC (2 nM final), the sample solution was analyzed with a flow cytometry (EPICS ALTRA Cell Sorter, Beckman Coulter). Viability of the cells were assessed by the signals of FC (front scattering) and PMT1 (side scattering). Fluorescence signals of fNLFNYK-FITC from 10,000 cells were collected with a blue excitation laser (Ex. 488 nm). All the procedures were performed within 60 min after the cell collection to prevent from cell damage and cell death.

2-2-5. Arrestin binding assay

Luminescence measurements on 96-well white plates were performed according to previous reports with some modifications[14,15]. HEK293 cells stably expressing FPR1-ElucC and ElucN-ARRB1, FPR1-ElucC×ElucN-ARRB1 cells, were seeded with a cell density of 2.0×10^4 cells/well. After 48-hour incubation at 37°C in 5% CO$_2$, the medium was replaced to phenol red free DMEM containing 1% FBS and an inhibitor or DMSO. The cells incubated for 30 min at 37°C in 5% CO$_2$ were stimulated with the phenol red free medium containing 1% FBS and a ligand for 60 min at 37°C in 5% CO$_2$. The medium was removed and 100 μL of luminescence reagents, Emerald Luciferase assay reagent NEO (TOYOBO Co., Ltd.), were added in each well. Luminescence measurements were performed with a luminescence microtiter plate reader at room temperature (TriStar LB941, Berthold Japan Co., ltd.). The plates were first gently shaken for 5 min, and then luminescence emission from each well was measured every two seconds sequentially.

2-2-6. cAMP assay

FPR1×GloSensor in HEK293 cells were dispensed in a 96-well white plate with the concentration of 2.0×10^4 cells/well. After two days of incubation at 37°C with 5% CO$_2$, the medium was replaced with

100 µL of Locke's buffer[16] [154 mM NaCl, 1.3 mM CaCl$_2$, 5.6 mM KCl, 1 mM MgCl$_2$, 3.6 mM NaHCO$_3$, 5.6 mM Glucose, 20 mM HEPES] supplemented with 0.5 mM D-luciferin, 20 µM forskolin, 20 nM fMLP and test compounds. In the case of time-lapse monitoring, the cells were first incubated with 50 µL Locke's buffer containing 0.5 mM D-luciferin, 20 µM forskolin, and inhibitors, followed by addition of another 50 µL Locke's buffer containing 0.5 mM D-luciferin, 40 nM fMLP (20 nM final). Time dependent changes of luminescence intensity were detected with the microplate reader at room temperature (TriStar LB941). Luminescence emission from each well was measured every second sequentially. The values of maximum luminescence intensity (usually reached within 10 min) were used as the luminescence signals of the cAMP assay.

2-2-7. FRET measurement

Ratiometric FRET responses in HEK293 cells were taken at 25°C using an inverted epi-fluorescence microscope (Axiovert 200; Carl Zeiss Inc.), following the protocol published earlier[11]. The microscope was equipped with an oil immersion 63× objective lens, a dual-emission photometric system and a light source (Polychrome IV; Till Photonics GmbH). Single cells transiently transfected with the Gαi3-FRET probe and FPR1 were irradiated with 436 nm light at a frequency of 10 Hz. Fluorescence emissions from cpVenus and mTurquoise2 were separated using a DCLP 505 nm beam splitter and pass-through appropriate emission filters (535/30 nm for cpV and 480/40 nm for mTq2). The fluorescence signals were detected with photodiodes and an analogue-digital converter (Digidata 1440A, Axon Instruments). During the continuous FRET observations, the cells were superfused with measuring buffer or ligand solutions using a perfusion system (ALA-VM8; ALA Scientific Instruments). Every FRET measurement was followed by an observation of the FRET response against a transient 10 µM fMLP stimulation. Using the fMLP responses as normalization standards, relative FRET changes were recorded to minimize the effects of photobleaching.

2-2-8. Analysis

To determine EC50 and IC50 values, dose-dependent curves were fitted to a Hill equation; *output signals = bottom + (top-bottom) / (1 + ([ligand] / IC50) ^ n)*, where the four parameters, *top*, *bottom*, *IC50*, and *n* are fitting parameters.

2-3. Results

2-3-1. Ligand binding assay

Direct binding of chemical compounds to FPR1 was examined with fluorescence-based ligand binding assay (**Fig. 2-2A**). HEK293 cells stably expressing wild type FPR1 were treated with a fluorescent ligand, fNLFNYK-FITC. The amount of cell bound ligands was detected with flow cytometry. **Fig. 2-2B** shows fluorescence signals from the fluorescent-ligand-labeled cells. The fluorescence intensity increased rapidly from 0 to 6 nM, gradually from 6 to 60 nM, and increased linearly above 60 nM, suggesting the presence of specific and non-specific binding of the fluorescent ligand. Under the low concentrations, the ligand binding exhibited a concentration response following the Michaelis-Menten equation with saturating binding. Under the high concentration, non-specific fluorescence signals proportional to the ligand concentrations were detected. From these considerations, the dose-dependent curve was fitted to a sum of the two equations: $y = 12.05x/(x+0.60) + 0.24x + 3.14$ (**Fig. 2-2B**). The dose–response curve subtracting the nonspecific binding ($y = 0.24x$) showed a clear Michaelis-Menten curve with a rapid increase at intermediate concentration and a plateau at high concentration (**Fig. 2-2C**). The dissociation constant for the fluorescent ligand was calculated to be 0.6 nM, consistent with previous reports (Kd = 0.6 nM)[17]. From the dose–response curve, an optimal concentration of the fluorescent ligand for following experiments was determined to be 2 nM, where a high level of binding was observed but the binding was not fully saturated. The binding of chemical compounds for FPR1 was measured by competitive binding inhibition against the fixed concentration of the fluorescent ligand. The competitive binding inhibition of inhibitors, cyclosporin H (CysH) and Methionine Benzimidazole 6 (MB6), was examined (**Figs. 2-2D–F**). As expected, 10 nM CysH did not affect the fluorescent ligand binding, whereas 10 μM CysH almost completely abolished the fluorescent ligand binding. The dose–response curve of CysH showed a sigmoidal curve with an IC50 value of 0.38 ± 0.05 μM (**Fig. 2-2E**), consistent with previous reports (IC50 = 0.7 μM)[18]. Also, MB6 showed a clear competitive binding inhibition curve with an IC50 value of 0.55 ± 0.21 μM (**Fig. 2-2F**), consistent with previous reports (IC50 = 0.5 μM)[19]. The binding of an endogenous ligand, fMLP, was also examined in the assay. The decrease in fluorescence intensity demonstrated the IC50 value of 0.11 ± 0.02 μM (**Fig. 2-2G**), consistent with previous report (Ki = 0.1 μM)[20]. Therefore, the direct interaction between FPR1 and chemical compounds in living cells was investigated quantitatively using the fluorescence-based binding assay.
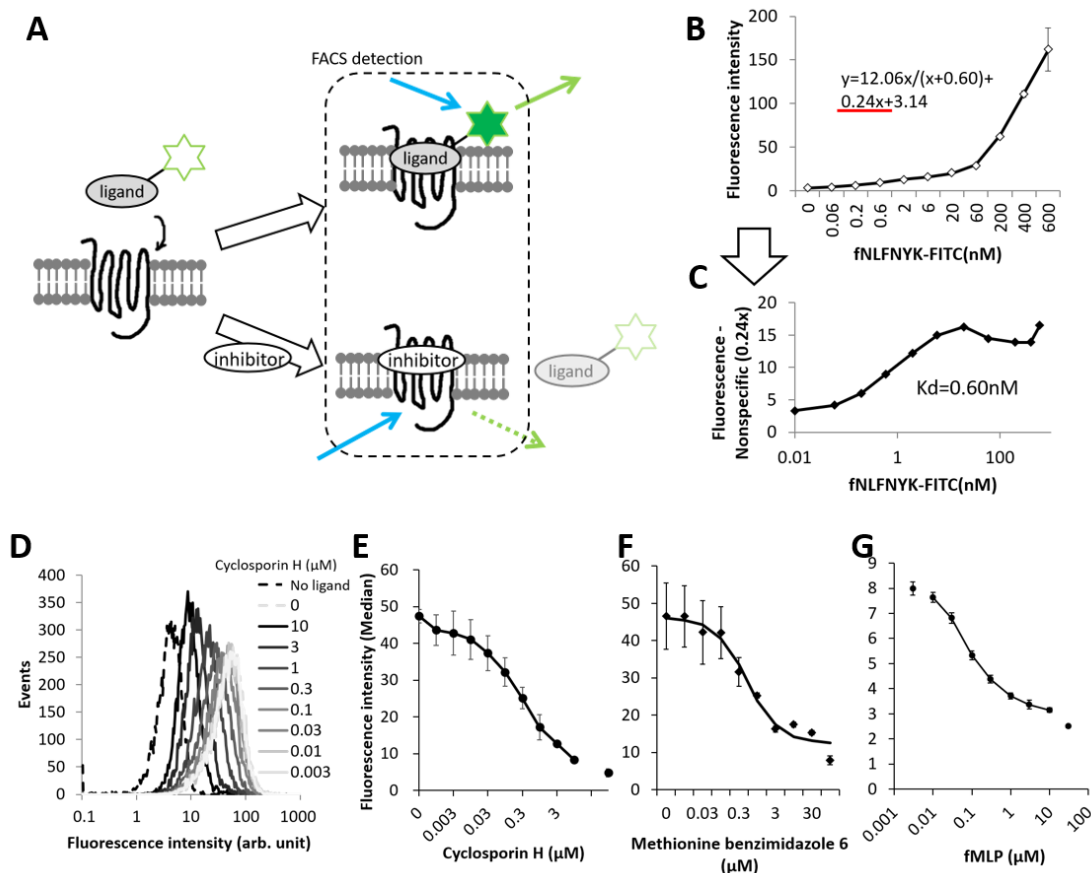
,

Fig. 2-2. Quantitative measurement of ligand binding to FPR1 using flow cytometry. (A) Schematic diagram of fluorescent ligand binding assay. HEK293 cells harboring FPR1 were stained with the fluorescent ligand, fNLFNYK-FITC. The cell-bound fluorescent ligand was detected by flow cytometry. Specific inhibitors for FPR1 would reduce the binding of the fluorescent ligand, and thus reduce the fluorescence emission from the cells. (B) Fluorescence emission from the FPR1-expressing cells treated with a wide concentration range of fNLFNYK-FITC. The concentration-dependent curve shows a sigmoidal curve at low ligand concentrations and a linear increase at high ligand concentrations. (C) Fluorescence emission induced by the specific binding of the ligand to FPR1. I subtracted the nonspecific fluorescence emission ($y=0.24x$) from the total fluorescence emission shown in B to obtain the fluorescence emission caused by the specific ligand binding. (D) Raw data of flow cytometry measurements for the cells treated with the fluorescent ligand and an inhibitor, Cyclosporin H. The data were shown in histograms with the horizontal axis as the fluorescence intensity of the cells. Dotted black and gray lines, respectively, indicated the cells without any treatment and the cells only treated with the fluorescent ligand. Solid line histograms indicated the cells treated with both fluorescent ligand and inhibitor. Addition of the inhibitor left-shifted the histograms, suggesting the competitive binding inhibition. (E, F, G) Mean fluorescence intensities of the cells treated with the fluorescent ligand and specific inhibitors, Cyclosporin H (E) or Methionine

33

Benzimidazole 6 (F), or specific agonist, fMLP (G). All the measurements were duplicated. The results were shown as mean ± s.d.

The time course of the ligand binding was assessed using the established assay system. I observed the stable fluorescence signals just after the addition of the fluorescent ligand, suggesting very fast on-rate of the ligand binding (reaching to the equilibrium within a few seconds). To obtain off-rates of the binding, the cells were stained with the fluorescent ligand, fNLFNYK-FITC, were centrifuged, and were re-suspended in ligand-free medium. I prepared two controls: positive control with the fluorescent ligand in re-suspended medium and negative control with no staining. Both controls showed gradual increases in fluorescence intensity over time (**Fig. 2-3A**). Using the temporal changes of the controls, the time-course of fluorescence intensity of the ligand-depleted cells were normalized (**Fig. 2-3B**). The normalized fluorescence intensity decreased from 0.5 to a plateau at 0.3 in 30 min. When the curve was fitted to a one-component exponential function, the time constant of the dissociation reaction was calculated to be 10.2 ± 0.9 min. Previous reports have demonstrated that the dissociation time constants of the ligands for FPR1 varied dependent on the association periods. The time constant observed in the present study was consistent with the dissociation time of the ligands associating to FPR1 for a short time period[17]. Incomplete staining ($0.5 < 1$) at the initial time point may be due to the ligand unbinding during the centrifugation and the resuspension processes. Residual staining ($0.3 > 0$) at late time points may be due to the presence of a low concentration of the fluorescent ligand and an irreversible intake of ligands into the cells caused by the activation of FPR1. The result suggests that dynamics of the ligand unbinding can be measured if reactions take in an order of minutes.
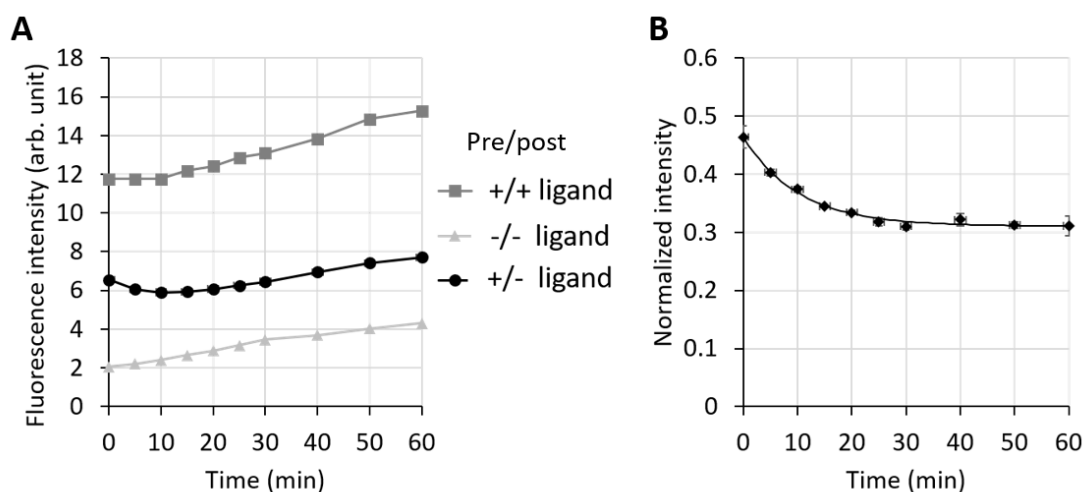

Fig. 2-3. Fluorescence intensity after washing out the fluorescent ligand. (A) The temporal changes in fluorescence intensity. The cells were pretreated (+) or not treated (-) with the fluorescent ligand, were centrifuged, and were resuspended in the medium containing the fluorescent ligand (+) or not (-). (B)

Normalized temporal changes of fluorescence intensity of the cells pretreated with the fluorescent ligand and washed with the ligand-free medium. $n = 4$. Mean ± s.d. The curve was fitted with a one-component exponential curve to obtain $y = 0.31 + 0.15 \exp(- x / 10.2)$.

2-3-2. Arrestin split-luciferase assay

Ligand activation triggers conformational changes of FPR1, leading to recruitments of G proteins and β-arrestins. Here, I detected the β-arrestin-recruitment to FPR1 using a split luciferase technique[15] (**Fig. 2-4**). The C-terminal fragment of a green light emitting luciferase, Eluc, was fused to FPR1 at its C-terminus. The N-terminal fragment of Eluc was fused to β-arrestin 1 at its N-terminal end. The split Eluc fragments do not emit luminescence by their own, but they recover their original protein structure and emit green bioluminescence when the two fragments were placed close together by the β-arrestin recruitment to FPR1 (**Fig. 2-4A**). **Fig. 2-4B** shows a dose–response curve of the luminescence intensity for the ligand stimulation. Although the signal was not saturated even at the highest concentration (3 μM), the steep increase at intermediate concentration (30–100 nM) suggested the Michaelis-Menten reaction of the ligand and FPR1. Fitting the curve to a Hill equation revealed the EC50 value to be 104 ± 22 nM. This value was much higher than previously reported value of 0.07 nM[21], which might be due to the differences in the assay systems and cell types. In the presence of 200 nM fMLP, the FPR1 inhibitor, CysH, reduced the luminescence signals dose-dependently (**Fig. 2-4C**). When the dose–response curve of CysH was fitted to a Hill equation, the IC50 value was calculated to 0.57 ± 0.07 μM. This value was consistent with the result of the competitive ligand binding measured by flow cytometry (0.38 μM). Therefore, arrestin split luciferase assay was an efficient technique to detect the ligand-induced arrestin recruitment quantitatively.

Compared to fluorescence or absorption measurements, bioluminescence measurement is superior in time-lapse measurement due to the lack of photobleaching. Time-courses of the luminescence signals were monitored over a wide concentration range of fMLP for 60 min (**Fig. 2-4D**). Luminescence signals were rapidly increased for 15–40 min and gradually decreased. Interestingly, the higher the ligand concentration was, the earlier the luminescence signal reached its maximum. At each time point, I plotted dose–response curves that were normalized by the values of maximum and minimum concentrations of fMLP (**Fig. 2-4E**). Compared to the early time points, the dose–response curves of the late time points were left-shifted, suggesting that the apparent ligand sensitivity of FPR1 was increased over time. Previous mathematical model suggested that the dose–response curves would be temporally altered if the ligand-binding kinetics is slower than downstream signal transduction reactions[10]. Therefore, FPR1 kinetically regulated the β-arrestin recruitment and responded to a wide range of ligand concentrations. The results indicate that time-dependent changes in signal transduction mediated by the interaction of FPR1 with β-arrestin can be detected using arrestin split luciferase assay.
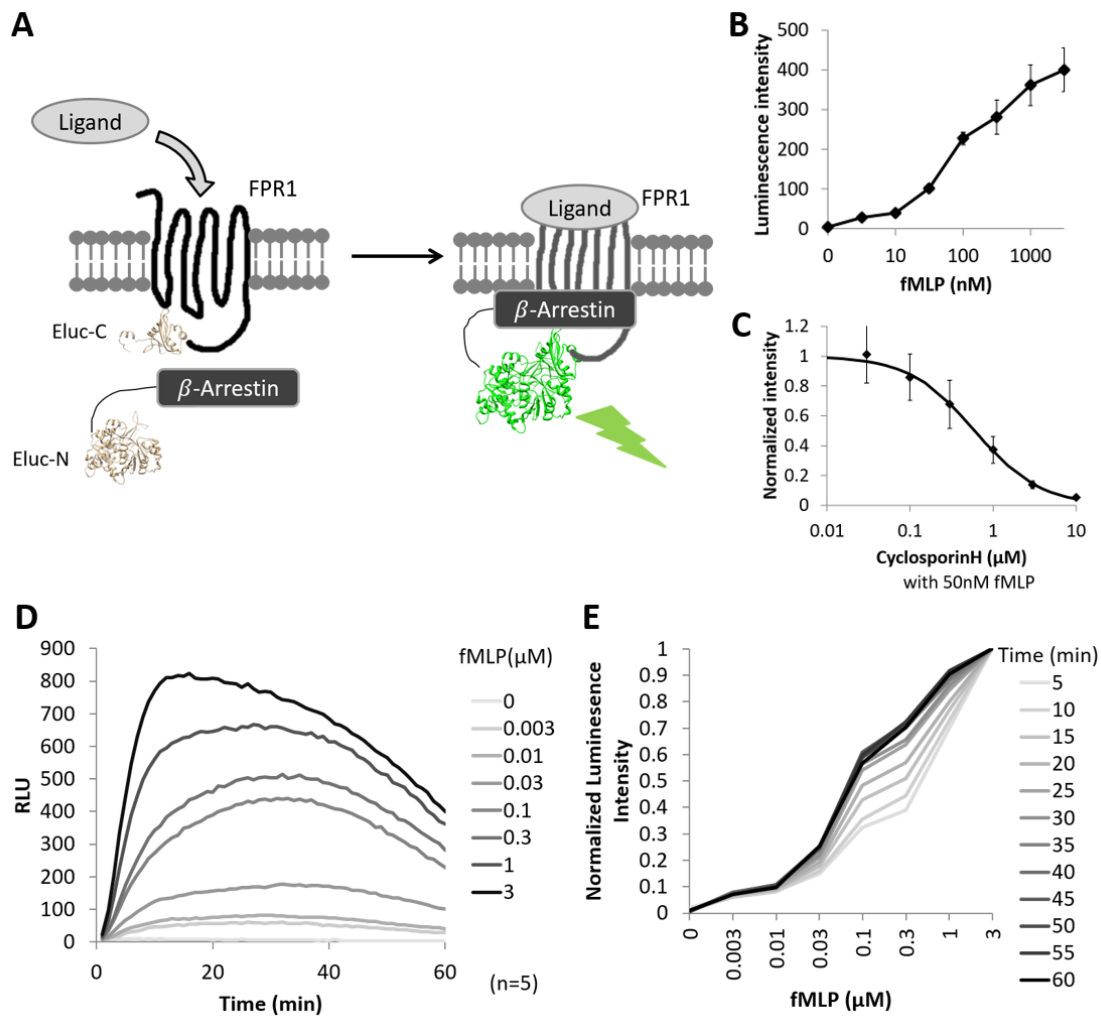
Fig. 2-4. Quantitative time-lapse detection of FPR1 signal transduction with β-arrestin split luciferase assay. (A) Schematic diagram of the β-arrestin split luciferase assay. FPR1 and β-arrestin, respectively, fused with split fragments of a bioluminescent protein, Eluc. Upon ligand stimulation, activated FPR1 induces a recruitment of β-arrestin, leading to the complementation of Eluc and the recovery of bioluminescence emission. (B) Bioluminescence signals of the cells treated with the FPR1 specific ligand, fMLP. $n = 5$. Mean ± s.d. The curve was fitted to a Hill equation to obtain $y = 2 + 414 / (1+ (x/104)^{0.86})$. (C) Bioluminescence signals of the cells treated with 50 nM fMLP and an inhibitor, Cyclosporin H. $n = 6$. Mean ± s.d. The dose-dependent curve was fitted to a Hill equation to obtain $y = 1.018 + 1.012 / (1+(x/0.57)^{1.07})$.

2-3-3. cAMP assay

Next, downstream signaling of G protein pathway was investigated with cAMP assay. There are four types of G proteins, Gi, Gq, Gs, and $G_{12/13}$, and they have different signaling outputs. FPR1 exclusively activates Gi proteins that inhibit adenylyl cyclase (AC) activities, resulting in a decrease in the concentration of cytosolic cAMP. In the cAMP assay, the changes in the cAMP concentration was monitored with a commercially available bioluminescence probe (GloSensor) (**Fig. 2-5A**)[22]. Due to a low basal activity of ACs in HEK293 cells, ACs were preactivated by forskolin and the following Gi-mediated decrease of cAMP production was measured. As expected, forskolin treatment increased the background luminescence signals, and additional fMLP treatment reduced the luminescence increases (**Figs. 2-5B, C**). The concentrations of forskolin and fMLP were optimized to 20 µM and 20 nM, respectively, so that the dose–response curves did not reach plateaus while maximizing the dynamic range of the measurement. A wide concentration range of FPR1 inhibitors was introduced additionally to the cells under the established condition (**Figs. 2-5D, E**). The result showed a dose-dependent increase in the luminescence signals, that is, an inhibition of the ligand-induced decrease in luminescence intensity. The IC50 values for CysH and MB6 were 2.0 ± 0.4 µM and 2.93 ± 0.08 µM, respectively. These values were slightly higher than those measured by the other assay systems. Temporal changes in the amount of cAMP were monitored (**Figs. 2-5F, G**). When all the compounds were applied simultaneously, the bioluminescence signals increased initially and then decreased gradually (**Fig. 2-5F**). The ligand and inhibitor for FPR1 did not affect the kinetics but affected the peak height of bioluminescence response, suggesting that the forskolin-induced cAMP production was the rate-limiting step. To observe the kinetics of FPR1-induced inhibition of cAMP production, the cells were first equilibrated with forskolin and MB6 for 60 min, and then fMLP was administrated (**Fig. 2-5G**). Without FPR1 stimulation, forskolin-induced cAMP production was gradually decreased and halved in 16 min. The possible reason of the decrease would include desensitization of ACs, digestions of cAMP by endogenous enzymes, and consumption of the luminescence substrate[16]. fMLP stimulation rapidly reduced the amount of cAMP. The half-life was 3 min. Additional treatment with MB6 restored the temporal changes of forskolin-induced cAMP levels. The result indicated that G protein-mediated inhibition of ACs occurred in an order of a few minutes, which was faster than β-arrestin binding but slower than ligand binding. Consequently, I concluded that the abundance and temporal pattern of the G protein signaling followed by FPR1 activation can be quantified with the luminescence based cAMP assay.
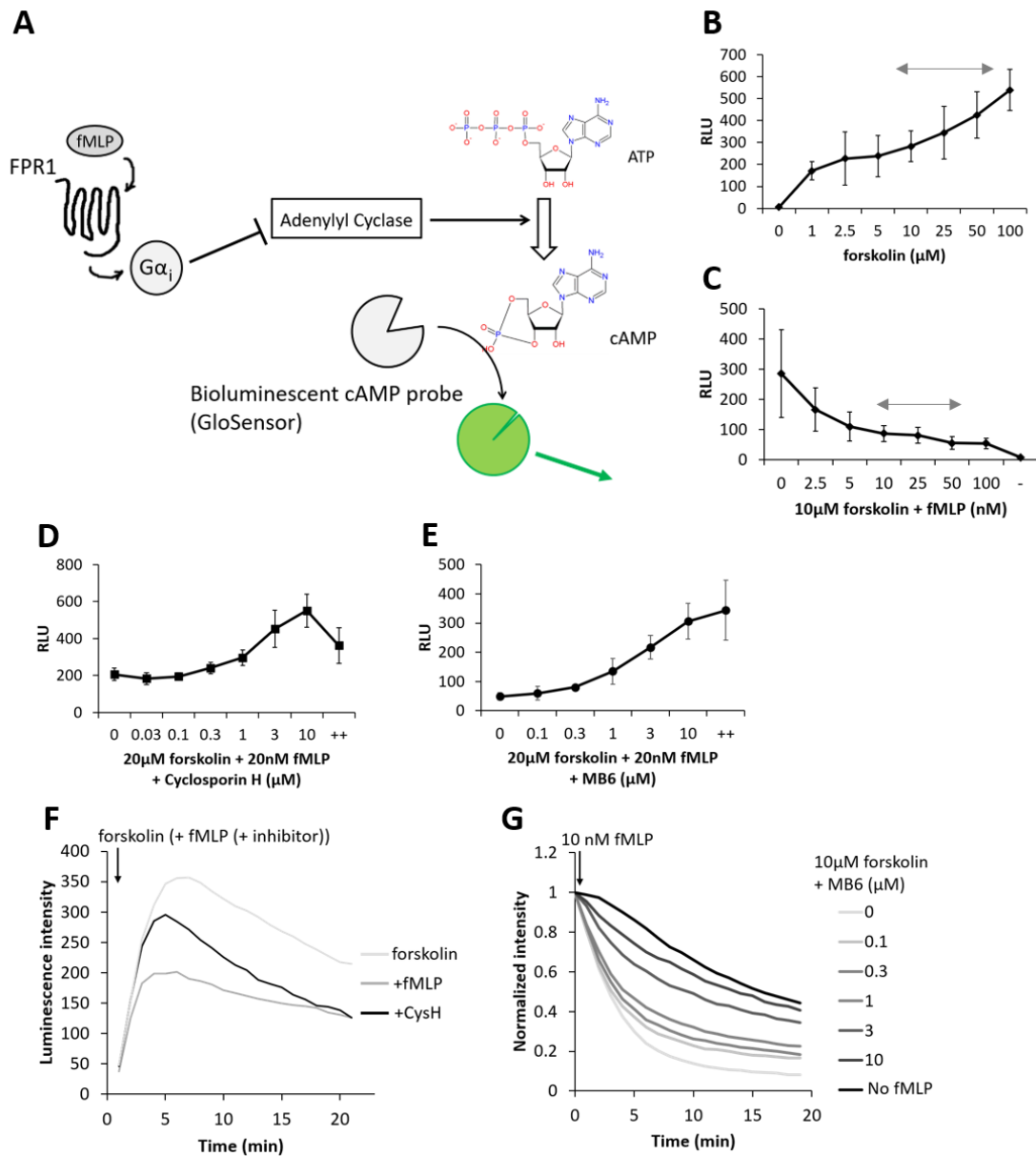
Fig. 2-5. Live-cell detection of FPR1 downstream signal transduction using a bioluminescence cAMP probe. (A) Schematic diagram of FPR1-mediated cAMP signal transduction. Endogenous enzymes, adenylyl cyclases, convert cytosolic ATP into cyclic AMP (cAMP). FPR1-induced Gαi protein activation downregulates the enzyme activity, leading to the reduction of the cytosolic concentrations of cAMP. In the cAMP assay, changes in the cAMP concentration were detected with a cAMP specific bioluminescent protein probe. (B) Bioluminescence signals of the cells treated with an agonist for endogenous adenylyl cyclases, called forskolin. Forskolin increased the background cAMP production dose-dependently. Subsaturating forskolin concentrations (10–50 μM) were used for the following experiments. $n = 6$. Mean ± s.d. (C) Bioluminescence signals of the cells treated with forskolin and an agonist for FPR1, fMLP. (-) denotes the cells treated with no stimulant. fMLP reduced the forskolin-

induced cAMP increase dose-dependently. Subsaturating fMLP concentrations (10–50 nM) were used for the following experiments. $n = 6$. Mean ± s.d. (D, E) Bioluminescence signals of the cells treated with forskolin, fMLP, and inhibitors for FPR1, cyclosporin H (D) or Methionine Benzimidazole 6 (E). (++) denotes the cells treated with only forskolin. The inhibitors compensated the fMLP-induced cAMP decrease. $n = 6$. Mean ± s.d. (F) Temporal changes of the bioluminescence signals after simultaneous treatments with forskolin, fMLP, and CysH. (G) Temporal changes of the bioluminescence signals of the cells pretreated with forskolin and MB6. The cells were treated with fMLP at $t = 0$.

2-3-4. G protein FRET assay

To assess G protein activation itself, I used a G protein FRET system and monitored the dissociation of Gα from Gβγ subunits. The FRET probe consists of a set of heterotrimeric G proteins with a CFP tag at the α subunit and a YFP tag at the γ subunit (**Fig. 2-6A**)[11]. The two fluorescent proteins were designed to locate in a close proximity with each other in the heterotrimeric G protein complex. Excitation of CFP caused a transfer in energy to adjacent YFP, resulting in FRET emission. When G proteins were activated by FPR1 and dissociated into subunits, CFP fluorescence emission was detected without energy transfer to YFP. Therefore, the G protein activity was measured with changes in the FRET efficiency.

The FRET probe was transiently expressed in HEK293 cells, and the changes in the fluorescence intensities were observed with epi-fluorescence microscopy. The ligand for FPR1 was transiently applied on the microscopy with a perfusion system (**Figs. 2-6B, C**). Typical FRET responses are shown in **Fig. 2-6D**. Increases in fluorescence intensity of CFP channel and concomitant decreases in that of YFP channel strongly indicated the presence of FRET changes. The FRET trace showed abrupt decreases upon ligand stimulation and gradual recoveries to the basal line after washing the ligand. The result indicated that the probe detected the ligand-induced dissociation of G protein subunits and their rebinding.

During repeated experiments, the responses were gradually decreased due to the desensitization of FPR1 and the photobleaching of the fluorophores. To obtain less biased results, a control measurement with the fixed concentration of fMLP (10 μM) was performed before each measurement, and the results were reported as normalized values based on each control. The ligand increased normalized FRET signals dose-dependently (**Fig. 2-6E**). When fitting the curve with the Hill equation, EC50 was calculated to 0.8 μM, which was in the same order as the value obtained with arrestin split luciferase assay (**Fig. 2-4B**). Subsequently, responses for N-terminally modified FPR1s (SNAP-FPR1, Halo-FPR1), which were used in the single molecule experiments in Chapter 3, were examined with the probe (**Fig. 2-6E**). Dose–response curves were almost completely overlapped with that of the wild type FPR1, indicating that the N-terminal modifications did not affect the downstream signaling

activity of FPR1. Altogether, the FRET assay system was established to quantify the G protein activity and the functional similarity between wild type and N-terminally labeled FPR1s were revealed.
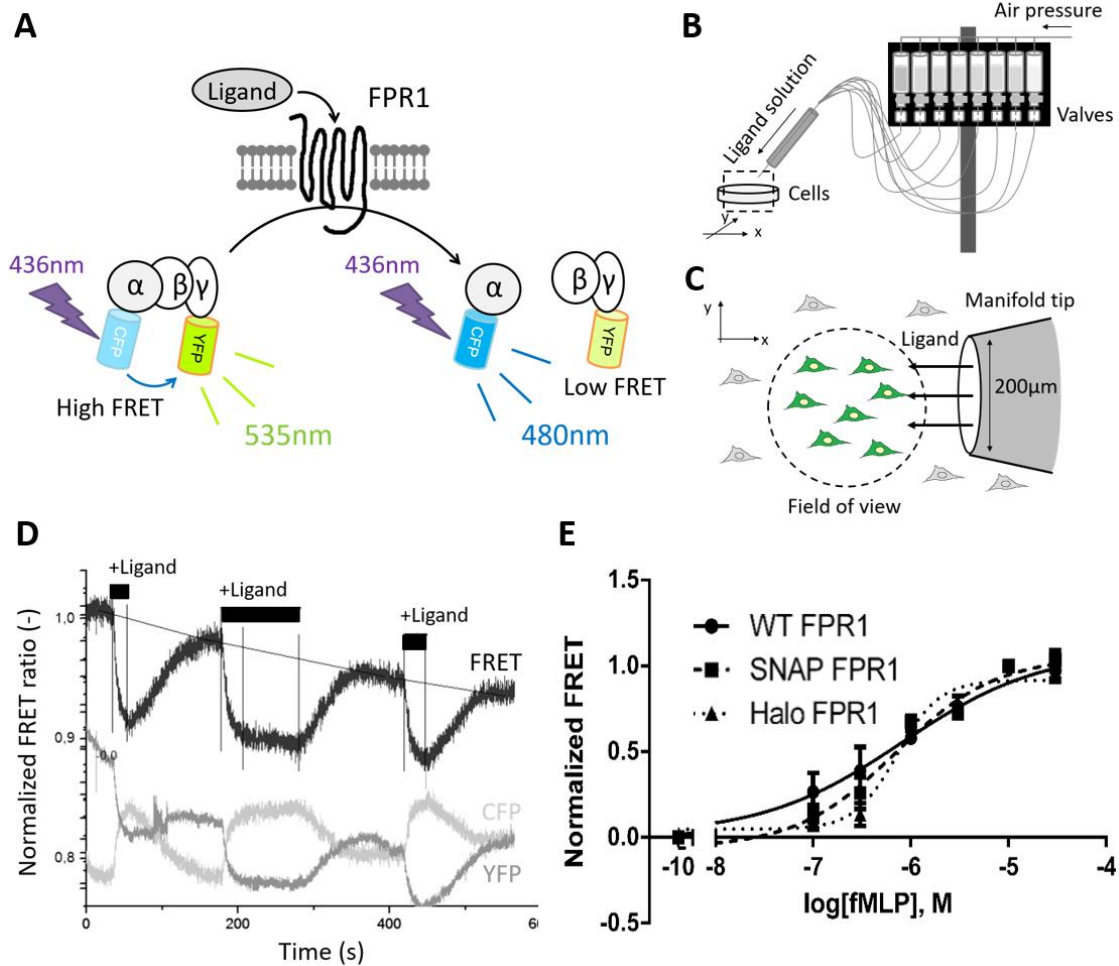

Fig. 2-6. Reversible and repeatable detection of FPR1-induced G protein activation with a FRET probe. (A) Schematic diagram of the principle of the G protein FRET probe. G protein α and γ subunits, respectively, were fused with cyan and yellow fluorescent proteins (CFP and YFP). Without stimulation, G proteins form heterotrimeric complexes, which brought CFP and YFP into close proximity and caused an energy transfer. Ligand stimulation of FPR1 activated and dissociated heterotrimeric G proteins, resulting in a decrease in the energy transfer. (B, C) Schematic diagram of the perfusion system for the ligand administration. Ligand and control solutions, respectively, were put in the syringes (B) and perfused locally on the cells (C). Rapid ligand addition and removal enabled reversible and repeatable measurements for a set of the cells in a field of view of the epi-fluorescence microscopy. (D) A typical FRET response of the cells treated with transient fMLP for three times. Unless indicated, the buffer without the ligand was perfused. Upon ligand application, the fluorescence intensity of the CFP channel increased, whereas that of the YFP channel decreased, indicating the presence of changes in the FRET energy transfer. Vertical lines indicate the start of ligand simulation,

40

the end of ligand stimulation, and the end of ligand-induced FRET change. Diagonally drawn lines indicate basal changes in FRET signals estimated by connecting the FRET values at start and the end of ligand stimulations. (E) Normalized FRET signals of the cells expressing (tagged) FPR1 in response to fMLP. All the FRET measurements were preceded by transient 10 μM fMLP stimulation, and each FRET change was normalized by each FRET response for 10 μM fMLP. The results were fitted with Hill equations to obtain EC50 values of 0.82, 0.70, and 0.72 μM for WT-FPR1, SNAP-FPR1, and Halo-FPR1, respectively. $n = 5$–11. Mean ± s.e.m.

Using the FRET probe, the temporal changes in the G protein activation were assessed. As a control, I monitored the activation and deactivation dynamics of G protein followed by ligand stimulation of another GPCR, α2-adrenergic receptor (α2AR) (**Fig. 2-7A**). Cells were treated with the ligand and washed for three times, exhibiting reproducible fast activation and slow deactivation. The time course of the reaction was quantified by fitting the temporal changes in FRET efficiency with single component exponential curve. The time constant for the α2AR-mediated activation was calculated to be 742 ± 140 ms, consistent with the previously reported value of 887 ms[11]. The deactivation kinetics was 49 ± 19 s. This result indicates that dynamics of G protein activation can be quantified in an order of a second using the FRET probe.

The typical temporal patterns of FRET signals for FPR1 activation are shown in **Fig. 2-6D**. The figure shows the reproducible responses of FRET decreases and increases. Besides, when the cells were stimulated for a long time (such as 1 min), the decreased FRET curve was parallel to the basal line. The following FRET recovery curve was almost the same as that after short time ligand stimulation. These results suggest that FPR1 activation reversibly affected a simple equilibrium of G protein activation states with no secondary slow reactions. The activation time constant of WT-FPR1-induced G protein was calculated to be 7.2 ± 0.9 s (mean ± s.e.m., $n = 33$) by fitting the curve with the single exponential curve. The value was 10 times as slow as that of α2AR, suggesting GPCR dependence of G protein activation kinetics. High concentrations of fMLP (30 μM) caused slightly faster FPR1 activation, whereas low concentrations (1–3 μM) caused slower activation (**Fig. 2-7B**). The N-terminally modified FPR1s (SNAP-FPR1 and Halo-FPR1) exhibited similar activation kinetics to WT FPR1. The results indicated that N-terminal modification did not affect activation dynamics for G protein signal transduction. I could not determine the deactivation constant for FPR1 because the FRET recovery curves could not be fully fitted with single exponential curves. This abnormal deactivation kinetics may be because the ligand dissociation rate of FPR1 (10 s) was as slow as the apparent G protein deactivation rate (40 s).
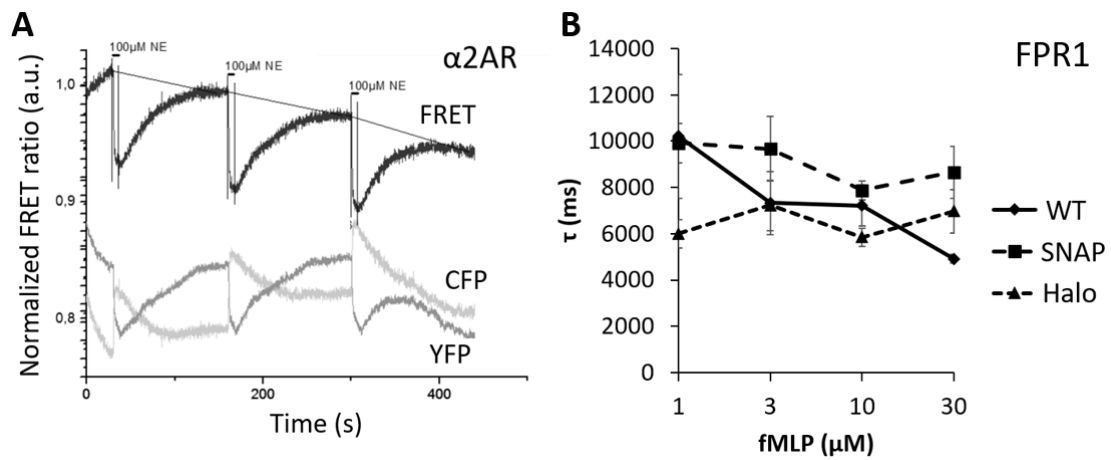
Fig. 2-7. Temporal changes in FRET responses. (A) A control experiment using α2-adrenergic receptor, α2AR, to demonstrate the fast responses of FRET signals. Signal increases of the CFP channel and concomitant decreases of the YFP channel strongly indicated the presence of FRET responses. By fitting the FRET curves to single component exponential curves, I obtained an on-rate of 742 ± 140 ms and an off-rate of 49 ± 19 s (mean ± s.d.). (B) On-rates of the FRET changes of the cells expressing (tagged) FPR1. The on-rates were obtained by fitting the FRET curves, such as shown in Fig. 2−5D, to single component exponential curves; $y = A \times exp\ (\text{-}\ x\ /\ \tau) + C$. n = 3–7. Mean ± s.e.m.

2-4. Discussion

I established four cell-based assays to quantify dose-dependent responses and temporal patterns of signal transductions of FPR1. The assays were validated by observing the ligand specific responses and the following inhibitions by FPR1-specific inhibitors. The specific ligand, fMLP, induced dose-dependent FPR1 activation in all the assays. When I focused on the Kd or EC50 values, 0.6 nM ligand bound to FPR1, 2 nM ligand triggered cAMP decrease, 50 nM ligand induced β-arrestin recruitment, and 1 μM ligand activated G protein (**Fig. 2-8A**). Low concentrations of ligands were enough to equilibrate the ligand-FPR1 binding and cAMP decrease, whereas high concentrations were required for full recruitment of β-arrestin and full activation of G proteins. Previous reports consistently demonstrated that the EC50 values of the FPR1 agonist for cAMP and pERK were approximately 1 nM, being lower than the EC50 value of 20 nM for internalization[23]. This result suggests that the formation of the ligand bound FPR1 was not enough to induce the full activation of downstream signaling. Moreover, FPR1 can induce different downstream signaling patterns dependent on the concentrations of the ligands.

The temporal patterns of ligand-induced signaling events were also varied among assays. The ligand binding reached an equilibrium within a few seconds, the G protein activation took 30 s, the cAMP decrease took 3 min, and the β-arrestin recruitment required 10 min or longer (**Fig. 2-8B**). The conformational changes of luciferases used in the cAMP assay and β-arrestin assay were fast enough to detect the reaction of an order of 1 s in vitro[24] and of an order of 1 min in cells[25]. Hence, the observed time constants did not suffer from technical limitations and reflected the true kinetics of the signal transduction events. The temporal patterns suggest that the ligand bound FPR1 required additional times to activate the downstream signaling events. The result of the arrestin split luciferase assay demonstrated that the dose–response was dependent on the time point after ligand administration (**Fig. 2-4E**). This observation explained a part of the varied dose–responses: The low ligand sensitivity detected with the FRET assay (EC50 = 1 μM) might be partly because the equilibrium time point was early (30 s) compared to β-arrestin assay (60 min) or cAMP assay (10 min). However, ligand binding and cAMP response were early in time point and sensitive to fMLP concentrations compared to β-arrestin assay, indicating that FPR1 activation and following signal transduction were not simply controlled by ligand binding but dynamically regulated by interacting proteins, such as G protein, β-arrestin, and adenylyl cyclases.
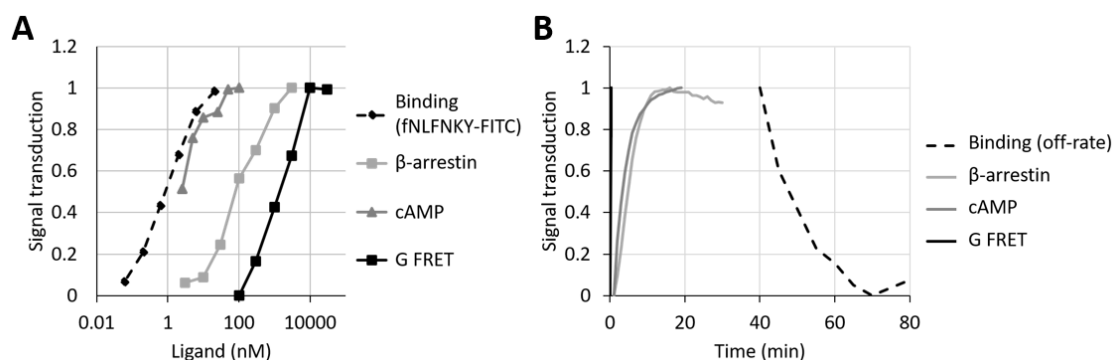
Fig. 2-8. Dose–responses and temporal patterns of FPR1 signal transduction events. (A) The dose–responses obtained by the four assays were summarized. All the results were normalized to the maximum responses and the basal signals. Except for the binding assay, fMLP was used as an agonist for FPR1. (B) The temporal patterns of signal transductions. The increases in the signal transductions after ligand stimulation are shown for the β-arrestin assay, cAMP assay, and G protein FRET assay. The decrease in the FPR1-bounds ligands are shown for the binding assay. For visualization, the first time point for the ligand unbinding process is artificially set to $t = 40$ min.

The presently established set of assay systems enables the evaluation of inhibitory potencies of chemical compounds. I obtained dose–response curves of known inhibitors with cAMP, arrestin, and binding assays. Simultaneous application of 10 µM fMLP and 10 µM Cyclosporin H reduced the FRET change compared to the application of fMLP only (data not shown). Hence, these four assays would be applicable for measuring the dose dependent inhibitions of chemical compounds. The kinetics of the inhibitions would also be measurable. To determine kinetics of signal inhibition by the inhibitors, the incubation times of the ligand and inhibitors will strongly affect the results. In cAMP assay, I observed that simultaneous addition of forskolin and fMLP induced a transient increase in the cAMP concentrations, whose peak height was reduced by CysH (**Fig. 2-5F**). In contrast, pretreatment of forskolin followed by fMLP addition induced a gradual decrease, whose kinetics was decelerated by CysH (**Fig. 2-5G**). The result demonstrated that changing the incubation times for the ligands may result in different temporal patterns and misinterpretations. Both simultaneous administration and pretreatment should be tested for proper understanding of inhibition kinetics. The kinetic information of inhibition would be beneficial for estimating the potential efficacy of chemical compounds as a drug to compete with endogenous ligands and quench the malfunctions of GPCRs in living systems.

2-5. Conclusion

FPR1 dose-dependently binds to ligands, activates G proteins, inhibits cAMP production, and induces β-arrestin recruitment. The temporal patterns of the four activation processes were different among signaling events (**Fig. 2-9**). The formation of ligand-bound FPR1 triggers dynamic interactions with G protein, β-arrestin and other proteins to regulate various downstream signals with temporal precision. Importantly, all the assay systems were developed in the same HEK293 cells, enabling the direct comparison of the efficiency and kinetics among the four signal transduction events. Determination of inhibitory capacities of chemical compounds using the present system would lead to signal specific drug discovery.
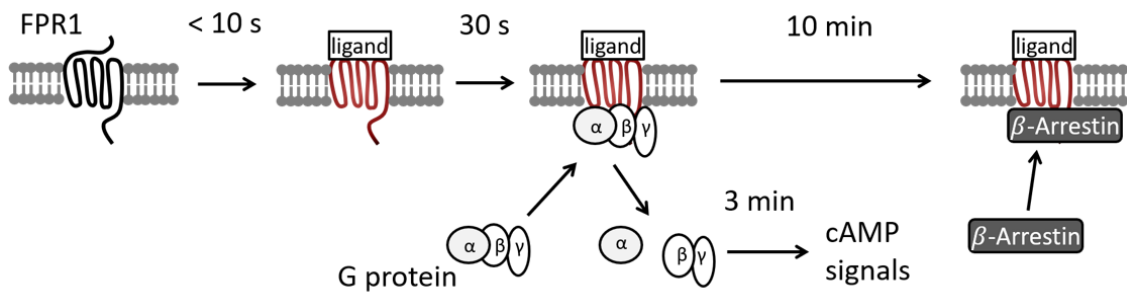

Fig. 2-9. Temporal propagation of FPR1 signal transductions revealed by the four live-cell real-time assay systems.

2-6. References

(1)   Dorward, D. A.; Lucas, C. D.; Chapman, G. B.; Haslett, C.; Dhaliwal, K.; Rossi, A. G. The Role of Formylated Peptides and Formyl Peptide Receptor 1 in Governing Neutrophil Function during Acute Inflammation. *Am. J. Pathol.* **2015**, *185* (5), 1172–1184. https://doi.org/10.1016/j.ajpath.2015.01.020.

(2)   Saito, N.; Qiao, H.; Yanagi, T.; Shinkuma, S.; Nishimura, K.; Suto, A.; Fujita, Y.; Suzuki, S.; Nomura, T.; Nakamura, H.; et al. An Annexin A1-FPR1 Interaction Contributes to Necroptosis of Keratinocytes in Severe Cutaneous Adverse Drug Reactions. *Sci. Transl. Med.* **2014**, *6*, 245ra95. https://doi.org/10.1126/scitranslmed.3008227.

(3)   Zhang, S.; Gong, H.; Ge, Y.; Ye, R. D. Biased Allosteric Modulation of Formyl Peptide Receptor 2 Leads to Distinct Receptor Conformational States for Pro- and Anti-Inflammatory Signaling. *Pharmacol. Res.* **2020**, 105117. https://doi.org/10.1016/j.phrs.2020.105117.

(4)   Raabe, C. A.; Gröper, J.; Rescher, U. Biased Perspectives on Formyl Peptide Receptors. *Biochim. Biophys. Acta - Mol. Cell Res.* **2019**, *1866* (2), 305–316. https://doi.org/10.1016/j.bbamcr.2018.11.015.

(5)   Qin, C. X.; May, L. T.; Li, R.; Cao, N.; Rosli, S.; Deo, M.; Alexander, A. E.; Horlock, D.; Bourke, J. E.; Yang, Y. H.; et al. Small-Molecule-Biased Formyl Peptide Receptor Agonist Compound 17b Protects against Myocardial Ischaemia-Reperfusion Injury in Mice. *Nat. Commun.* **2017**, *8*, 14232. https://doi.org/10.1038/ncomms14232.

(6)   Deora, G. S.; Qin, C. X.; Vecchio, E. A.; Debono, A. J.; Priebbenow, D. L.; Brady, R. M.; Beveridge, J.; Teguh, S. C.; Deo, M.; May, L. T.; et al. Substituted Pyridazin-3(2 H)-Ones as Highly Potent and Biased Formyl Peptide Receptor Agonists. *J. Med. Chem.* **2019**, *62* (10), 5242–5248. https://doi.org/10.1021/acs.jmedchem.8b01912.

(7)   Sklar, L. a; Sayre, J.; McNeil, V. M.; Finney, D. a. Competitive Binding Kinetics in Ligand-Receptor-Competitor Systems. Rate Parameters for Unlabeled Ligands for the Formyl Peptide Receptor. *Mol. Pharmacol.* **1985**, *28*, 323–330.

(8)   Servant, G.; Weiner, O. D.; Herzmark, P.; Balla, T.; Sedat, J. W.; Bourne, H. R. Polarization of Chemoattractant Receptor Signaling during Neutrophil Chemotaxis. *Science* **2000**, *287* (5455), 1037–1040. https://doi.org/10.1126/science.287.5455.1037.

(9)   Janetopoulos, C.; Ma, L.; Devreotes, P. N.; Iglesias, P. A. Chemoattractant-Induced Phosphatidylinositol 3,4,5-Trisphosphate Accumulation Is Spatially Amplified and Adapts, Independent of the Actin Cytoskeleton. *Proc. Natl. Acad. Sci. U. S. A.* **2004**, *101* (24), 8951–8956. https://doi.org/10.1073/pnas.0402152101.

(10)   Ventura, A. C.; Bush, A.; Vasen, G.; Goldín, M. a; Burkinshaw, B.; Bhattacharjee, N.; Folch, A.; Brent, R.; Chernomoretz, A.; Colman-Lerner, A. Utilization of Extracellular Information before Ligand-Receptor Binding Reaches Equilibrium Expands and Shifts the Input Dynamic Range.

Proc Natl Acad Sci U S A **2014**. https://doi.org/10.1073/pnas.1322761111.

(11)   Van Unen, J.; Stumpf, A. D.; Schmid, B.; Reinhard, N. R.; Hordijk, P. L.; Hoffmann, C.; Gadella, T. W. J.; Goedhart, J. A New Generation of FRET Sensors for Robust Measurement of Gαi1, Gαi2 and Gαi3 Activation Kinetics in Single Cells. *PLoS One* **2016**, *11* (1), e0146789. https://doi.org/10.1371/journal.pone.0146789.

(12)   Misawa, N.; Kafi, A. K. M.; Hattori, M.; Miura, K.; Masuda, K.; Ozawa, T. Rapid and High-Sensitivity Cell-Based Assays of Protein-Protein Interactions Using Split Click Beetle Luciferase Complementation: An Approach to the Study of G-Protein-Coupled Receptors. *Anal. Chem.* **2010**, *82* (6), 2552–2560. https://doi.org/10.1021/ac100104q.

(13)   Kafi, A. K. M.; Hattori, M.; Misawa, N.; Ozawa, T. Dual-Color Bioluminescence Analysis for Quantitatively Monitoring G-Protein-Coupled Receptor and β-Arrestin Interactions. *Pharmaceuticals* **2011**, *4* (3), 457–469. https://doi.org/10.3390/ph4030457.

(14)   Yang, L.; Nasu, Y.; Hattori, M.; Yoshimura, H.; Kanno, A.; Ozawa, T. Bioluminescent Probes to Analyze Ligand-Induced Phosphatidylinositol 3,4,5-Trisphosphate Production with Split Luciferase Complementation. *Anal. Chem.* **2013**, *85*, 11352–11359. https://doi.org/10.1021/ac402278f.

(15)   Takakura, H.; Hattori, M.; Takeuchi, M.; Ozawa, T. Visualization and Quantitative Analysis of G Protein-Coupled Receptor-β-Arrestin Interaction in Single Cells and Specific Organs of Living Mice Using Split Luciferase Complementation. *ACS Chem. Biol.* **2012**, *7* (5), 901–910. https://doi.org/10.1021/cb200360z.

(16)   DiRaddo, J. O.; Miller, E. J.; Hathaway, H. A.; Grajkowska, E.; Wroblewska, B.; Wolfe, B. B.; Liotta, D. C.; Wroblewski, J. T. A Real-Time Method for Measuring CAMP Production Modulated by Gαi/o-Coupled Metabotropic Glutamate Receptors. *J. Pharmacol. Exp. Ther.* **2014**, *349* (3), 373–382. https://doi.org/10.1124/jpet.113.211532.

(17)   Sklar, L. A.; Finney, D. A.; Oades, Z. G.; Jesaitis, A. J.; Painter, R. G.; Cochrane, C. G. The Dynamics of Ligand-Receptor Interactions. Real-Time Analyses of Association, Dissociation, and Internalization of an N-Formyl Peptide and Its Receptors on the Human Neutrophil. *J. Biol. Chem.* **1984**, *259* (9), 5661–5669.

(18)   Wenzel-Seifert, K.; Seifert, R. Cyclosporin H Is a Potent and Selective Formyl Peptide Receptor Antagonist. Comparison with N-t-Butoxycarbonyl-L-Phenylalanyl-L-Leucyl-L-Phenylalanyl-L-Leucyl-L-Phenylalanine and Cyclosporins A, B, C, D, and E. *J. Immunol.* **1993**, *150* (10), 4591–4599.

(19)   Unitt, J.; Fagura, M.; Phillips, T.; King, S.; Perry, M.; Morley, A.; MacDonald, C.; Weaver, R.; Christie, J.; Barber, S.; et al. Discovery of Small Molecule Human FPR1 Receptor Antagonists. *Bioorg. Med. Chem. Lett.* **2011**, *21* (10), 2991–2997. https://doi.org/10.1016/j.bmcl.2011.03.049.

(20)   Schneider, E. H.; Weaver, J. D.; Gaur, S. S.; Tripathi, B. K.; Jesaitis, A. J.; Zelenka, P. S.; Gao,

J.-L.; Murphy, P. M. The Leukocyte Chemotactic Receptor FPR1 Is Functionally Expressed on Human Lens Epithelial Cells. *J. Biol. Chem.* **2012**, *287* (48), 40779–40792. https://doi.org/10.1074/jbc.M112.411181.

(21)   Showell, H. J.; Freer, R. J.; Zigmond, S. H.; Schiffmann, E.; Aswanikumar, S.; Corcoran, B.; Becker, E. L. The Structure-Activity Relations of Synthetic Peptides as Chemotactic Factors and Inducers of Lysosomal Secretion for Neutrophils. *J. Exp. Med.* **1976**, *143* (5), 1154–1169. https://doi.org/10.1084/jem.143.5.1154.

(22)   Fan, F.; Binkowski, B. F.; Butler, B. L.; Stecha, P. F.; Lewis, M. K.; Wood, K. V. Novel Genetically Encoded Biosensors Using Firefly Luciferase. *ACS Chem. Biol.* **2008**, *3* (6), 346–351. https://doi.org/10.1021/cb8000414.

(23)   Gröper, J.; König, G. M.; Kostenis, E.; Gerke, V.; Raabe, C. A.; Rescher, U. Exploring Biased Agonism at FPR1 as a Means to Encode Danger Sensing. *Cells* **2020**, *9* (4). https://doi.org/10.3390/cells9041054.

(24)   Ohmuro-Matsuyama, Y.; Chung, C.-I.; Ueda, H. Demonstration of Protein-Fragment Complementation Assay Using Purified Firefly Luciferase Fragments. *BMC Biotechnol.* **2013**, *13*, 31. https://doi.org/10.1186/1472-6750-13-31.

(25)   Hattori, M.; Tanaka, M.; Takakura, H.; Aoki, K.; Miura, K.; Anzai, T.; Ozawa, T. Analysis of Temporal Patterns of GPCR-β-Arrestin Interactions Using Split Luciferase-Fragment Complementation. *Mol. Biosyst.* **2013**, *9*, 957–964. https://doi.org/10.1039/c2mb25443c.

Chapter 3

Oligomer-induced signal enhancement revealed

by single molecule imaging

3-1. Introduction

GPCRs interact with each other to form protein complexes. The size and the temporal dynamics of the protein complexes varied among cells, receptors, and ligands. After ligand stimulation, many GPCRs interacte with β-arrestin and clathrins to form clusters, which are large enough to be detected under fluorescence confocal microscopy[1,2]. Some GPCRs, including rhodopsin, form stochastic clusters without ligand stimulation[3]. Investigation has been intensively done on smaller GPCR complexes, which are called oligomers containing approximately two to ten receptors, using biochemical and biophysical analysis such as native PAGE, co-immunoprecipitation, and Förster resonance energy transfer (FRET)[4–7]. However, the role of GPCR oligomer formation has been left as controversial[8]. In vitro, a monomer form of GPCRs has been fully functional in terms of recognizing specific ligands and activating G protein, suggesting that oligomer formation has been dispensable for signal transduction[9]. Single-molecule imaging studies have yet revealed the presence of GPCR oligomers of various sizes, ranging from monomers to tetramers[10,11], and have revealed monomer–dimer interconversion in living cells[12,13]. In addition, ligand-induced shifts in the oligomerization states of β2 adrenergic receptor[14] and D2 dopamine receptor[15,16] have been reported. These observations indicate that a specific ligand in living cells regulates the amounts of GPCR oligomers, implying the presence of functional roles of oligomer formations. Nevertheless, the function of the transient oligomerization of GPCRs in signal transduction, including G protein-mediated and arrestin-mediated signal transductions, has not been fully revealed.

I investigated small oligomer, large oligomer, and cluster states of a chemoattractant rhodopsin-like class A GPCR, Formyl Peptide Receptor 1 (FPR1), to clarify the role of the transient oligomerization of GPCRs in signal transduction (**Fig. 3-1**). First, ligand-induced cluster formation of FPR1 was observed using ensemble TIRF imaging. Next, using live-cell multi-color single-molecule fluorescence imaging, dynamic interactions of FPR1, G protein and a specific ligand on the plasma membrane were visualized. Ensemble TIRF observation revealed that the full agonist stimulation induced a cluster formation of FPR1 in 2 min. The cluster formation was fully dependent on β-arrestin expression and not on cholesterol enrichment. Single molecule imaging revealed that the full agonist stimulation increased the number of FPR1 large oligomers and that the oligomerized FPR1 allowed for prolonged interactions with G protein. Inhibitor treatment did not affect the FPR1-G protein interaction duration. Based on these results, I proposed a cooperative activation model for G protein signals in which ligand binding and its successive oligomerization of FPR1 regulate the efficacy for G protein activation. Combining with ensemble TIRF observation, the signal transduction events of FPR1 were tightly regulated by the ligand-induced temporal shifts in the size of FPR1 complexes from small oligomers, large oligomers, to clusters. By using the live-cell imaging systems, I revealed the heterogenous complex formation of FPR1 and thus dynamic signal transduction after the ligand stimulation in living systems. Signal transduction that is synergistically controlled by receptor

oligomerization is anticipated for use as a novel target for the development of pharmaceutical drugs with high specificity.
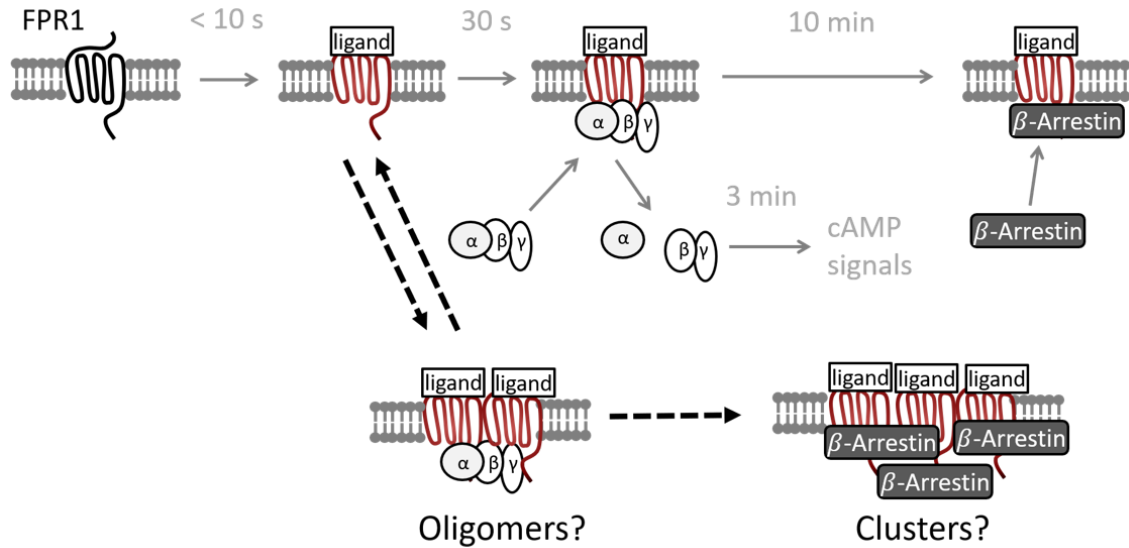

Fig. 3-1. Schematic diagram of my hypothesis on the FPR1 oligomerization and cluster formation during signal transduction. Previous reports have suggested that GPCRs are not always monomers but can form oligomers. Moreover, tens of GPCRs can form large clusters during arrestin- and cluthrin-mediated receptor endocytosis. From these reports, I hypothesized that the oligomer formation might be involved in G protein signal transduction.

3-2. Materials and Methods

3-2-1. Materials

Dulbecco's Modified Eagle Medium (DMEM) and Trypsin were purchased from Nacalai Tesque Inc. Fetal bovine serum (FBS), reduced serum medium (Opti-MEM ™), penicillin streptomycin (Pen Strep), Hank's balanced salt solution (HBSS), and FluoroBrite ™ DMEM were purchased from Gibco Inds. Inc. G418 sulfate and Zeocin™ were purchased from Invitrogen Corp. *Trans*IT®-LT1 was from Mirus Bio LLC. Formyl-methionyl-leucyl-phenylalanine (fMLP), cyclosporin H (CysH), WKYMVm trifluoroacetate salt (WKYMVm), cytochalasin D (CytoD), and pertussis toxin (PTX) were purchased from Sigma-Aldrich Corp. Methionine benzimidazole 6 (N-[1-[1-(1H-benzimidazol-2-yl)-3-methylsulfanylpropyl]-5-ethoxy-3-methyl-1-benzofuran-2-carboxamide) was purchased from Enamine Ltd. A fluorescence labeled ligand fNLFNYK-TMR was synthesized by Cosmo Bio Co., Ltd. DMSO, bovine serum albumin (BSA), HEPES, triethylamine (TEA), *N,N*-dimethylformamide (DMF), silicagel 70 TLC Plate-Wako were purchased from Fujifilm – Wako Pure Chemical Corp. BG-PEG-NH$_2$, SNAP-Surface® Alexa Fluor® 488, SNAP-Cell TMR-Star, and SNAP-Surface® Alexa Fluor® 647 were purchased from New England Biolabs, Inc. 24-well black glass bottom plates (EZVIEW®) were purchased from AGC Techno Glass Co., Ltd. HaloTag® TMR Ligand and HaloTag® R110Direct™ Ligand were purchased from Promega Corp. SeTau-647-NHS was obtained from SETA BioMedicals.

3-2-2. Preparation of a SNAP-tag SeTau ligand

SeTau-647-NHS was coupled to BG-PEG-NH$_2$ following the manufacturer's protocol for BG-PEG-NH$_2$. In brief, 2 µL of reaction mixture (5 mM SeTau-647-NHS, 7.5 mM BG-PEG-NH2 and 8 mM TEA in DMF) was incubated at 30°C overnight. The reaction mixture was separated by applying on a TLC plate using a 1:1 mixture of EtOH and MeOH as the mobile phase. The product representing a blue band was collected in a 1.5 mL tube and was eluted in 100 µL DMSO. After removing the silica gel by centrifugation, the SeTau647-PEG-BG concentration was quantified by measuring the absorbance at 675 nm ($\varepsilon = 200,000$ M^{-1} cm^{-1}). The obtained SeTau647-PEG-BG dye was diluted to be 50 µM and was stored at -30°C until use.

3-2-3. Plasmid construction

FPR1 was N-terminally fused with a SNAPf-tag and a membrane-localization signaling peptide from HTR3A. Halo-tag was inserted in the loop region between the Ras domain and the helix domain of Gαi3 (G60-S62). Earlier reports indicated that labeling at either of the ends of G protein α-subunits caused loss of its function or correct localization[17,18]. Gαi3, used in the present study, is one of the common Gαi proteins and exhibits an FPR1 binding affinity comparable to related G protein α-subunits i1 and i2[19]. The plasmids were constructed on mammalian expression vectors, pcDNA3.1

myc/His(B) and pcDNA4 V5/His(B). All the plasmids were verified using DNA sequencing (Eurofins Sequencing Service).

3-2-4. Cell culture

HEK293 cells were cultured in DMEM supplemented with 10% FBS, 100 μg/mL streptomycin and 100 U/mL penicillin at 37°C in 5% CO_2 atmosphere unless otherwise described. Stable cell lines SNAP-FPR1×Gαi3-Halo were established in HEK293 cells, which endogenously express no FPR1[20], by transfecting the two plasmids of SNAP-FPR1 and Gαi3-Halo with using *Trans*IT-LT1 (Mirus Bio LLC). The cells expressing SNAP-FPR1 and Gαi3-Halo were cultured in the medium supplemented with 0.8 mg/mL G418 and 0.05 mg/mL zeocin. The arrestin-knock out HEK293A cells have been developed by Dr. Asuka Inoue. For microscopic observation, the cells were cultured on glass-based dishes or 24-well glass-based plates, with collagen gel coating (CellMatrix-type C; Nitta Gelatin Inc.) following the manufacturer's protocol.

3-2-5. Labeling of the SNAP and Halo tag proteins

For the single molecule observations, cells at 70–80% confluency were stained in HBSS(+) supplemented with 50 nM SeTau647-PEG-BG and 1 nM HaloTag TMR Ligand for 15 min at 37°C in a CO_2 incubator. The cells were washed twice with HBSS(+) and were incubated for 15 min in the incubator. The medium was then replaced by FluoroBrite DMEM supplemented with 1% FBS. The cells were incubated at 37°C in 5% CO_2 until observation. For the ensemble TIRF measurements, the same labeling protocol was used except for 500 nM of SNAP fluorescent dyes applied to the cells.

3-2-6. Evaluation of labeling efficiency

To estimate the labeling efficiency, mean fluorescence intensities in a unit area of the cell membranes were quantified based on the TIRF images of the cells labeled with a range of concentrations of SeTau647-PEG-BG. The dose–response curve of the fluorescence intensity was fitted with a sum of a specific and nonspecific binding curve from the following equation.

$$Fluorescence\ intensity = a[Dye] + bottom + \frac{(top - bottom)}{\left(1 + \left(\frac{EC50}{[Dye]}\right)^b\right)}$$

Therein, [*Dye*] denotes the concentration of SeTau647-PEG-BG (nM); *top*, *bottom*, *a*, *b,* and *EC50* are fitting parameters to characterize the bindings. The first two components, *a[Dye]+bottom*, correspond to the nonspecific binding, whereas the last component denotes the specific binding of the dye with SNAP-FPR1.

The labeling efficiency was evaluated using the following equation.

$$Labeling\ efficiency\ =\ \frac{1}{(1 + \left(\frac{EC50}{[Dye]}\right)^{b})}$$

2-7, Western blot

The cells cultured on cell culture dishes (φ35 mm) for 48 hours at 37°C in 5% CO_2 were washed with PBS and suspended in 200 μL sampling buffer (50 mM Tris (pH 7.6), 5% glycerol, 2% SDS, 0.004% Bromophenol blue, 1% β-mercaptoethanol). The cells were transferred to 1.5 mL tubes and lysed with a sonicator (BIO RUPTOR, COSMO BIO co., ltd.) for 2 min at low intensity. After incubation for 5 min at 95°C, the sample mix was placed at 4°C and stored. The proteins were separated by SDS-PAGE on 10% acrylamide gels and transferred onto PVDF membranes. The proteins were immunolabeled by a gentle shake in ×2,000−×4,000 primary antibodies in the presence of 1% skimmed milk in TBST (50 mM Tris-HCl pH 8.0, 10 mM NaCl, 0.05% Tween 20) for 1 day at 4°C. The membranes washed with TBST buffer for three times were treated with ×10,000 secondary antibody in TBST containing 1% skimmed milk for 1 hour at room temperature. The membrane was again washed with TBST for three times and proteins were visualized with a luminescence reagent (SuperSignal WestFemto Maximum Sensitivity Substrate, Thermo Fisher Scientific Inc.). Luminescence images of the membranes were monitored with an image analyzer (ImageQuant LAS4000, General Electric Company). Protein sizes were estimated with a protein marker (Precision Plus Protein Kaleidoscope, TaKaRa Bio Inc.).

3-2-8. Confocal microscopy

Fluorescence emission from the cells was monitored with a confocal florescence microscope (IX81-FV-1000, Olympus Corporation Ltd.). Excitation wavelengths of 488, 561, and 635 nm were used for imaging EGFP, TMR and SeTau647, respectively. Images were cropped and the contrast was adjusted by using ImageJ software.

3-2-9. TIRF observation

Ensemble TIRF observation was conducted using a home-built objective-type total internal reflection fluorescence microscope (TIRFM) based on an inverted microscope (IX81; Olympus Corp.)[21]. The microscope was equipped with 488 nm (Sapphire; Coherent Inc.), 561 nm (JUNO; Showa Optronics Co. Ltd.) and 640 nm (CUBE; Coherent Inc.) diode lasers, a 405/488/561/635 band excitation filter (Semrock Inc.), a 100× oil-immersion objective (NA 1.49; Olympus Corp.), and two EMCCD cameras (ImagEM; Hamamatsu Photonics Inc.). The typical laser powers were modulated at 12 and 24 nW/μm^2, respectively, for 561 and 640 nm lasers after passing through the objective as epi-illumination. All live-cell observations were made under room temperature (23.0 ± 0.5°C). The

fluorescence signals were recorded on the two EMCCD cameras (512×512 pixel) at a frame rate of 1 Hz. All ligand solutions were prepared in FluoroBrite DMEM supplemented with 1% FBS and 0.1% DMSO.

Single-molecule observation experiments were also conducted using the same optical setups as that of ensemble TIRF microscopy. For two-color imaging, the microscope was equipped with 561 nm (JUNO; Showa Optronics Co. Ltd.) and 640 nm (CUBE; Coherent Inc.) diode lasers. The typical laser powers were adjusted at 4.8 and 9.5 $\mu W/\mu m^2$, respectively, for 561 and 640 nm lasers after passing through the objective as epi-illumination. The fluorescence emissions of TMR and SeTau647 were split by a dichroic mirror (FF662; Semrock Inc.) and were isolated with band-pass filters (Semrock Inc.), respectively, as 600/37 and 697/58, unless otherwise indicated. The fluorescence signals were recorded on the two EMCCD cameras under the subarray mode (256×256 pixel) at a frame rate of 55 Hz (18 ms/ frame). I acquired 200 frames of image sequences for each sample 2 min before and 30 s after ligand stimulation to FPR1 (10 μM). All ligand solutions were prepared in FluoroBrite DMEM supplemented with 1% FBS and 0.1% DMSO.

For three-color imaging, the microscope was equipped with 488 nm (Sapphire; Coherent Inc.), 561 nm (Sapphire; Coherent Inc.), and 647 nm (CUBE; Coherent Inc.) diode lasers, and three sCMOS cameras (two ORCA Flash 4.0v2 and one ORCA Flash 4.0v3; Hamamatsu Photonics Inc.). Typical laser powers were adjusted to 1.2, 0.8, and 1.2 $\mu W/\mu m^2$, respectively, for 488, 561, and 647 nm lasers after passing through the objective as epi-illumination. The images were recorded on center-quads of the sCMOS (512×512 pixel) at a frame rate of 30 ms/frame. A low concentration (50 nM) of a fluorescent ligand, fNLFNYK-TMR[22], was applied to identify single molecules of ligand-bound FPR1 while maintaining the background signals as sufficiently low. The fluorescence of R110, TMR, and SeTau647 were isolated respectively with band-pass filters, 525/50, 600/37, and 697/58 purchased from Semrock Inc. I acquired 200 frames of image sequences for each sample at each time point. The two time points were set to before ligand stimulation, and approximately 1 min after fluorescent ligand treatment when mobile fluorescent spots of fNLFNYK-TMR were observed on the cell membrane. To discriminate the specific binding from nonspecific adsorption of the ligand, lateral mobilities of the fluorescent spots were examined as described below. Ligand-bound FPR1 tracks were defined as those colocalized with mobile ligand tracks ($D > 1.0×10^{-2}$ $\mu m^2/s$) for longer than five frames (150 ms).

3-2-10. Single-particle detection

Optical aberrations, including positional differences of the multiple cameras and chromatic aberrations, were corrected based on bright field images of a pinhole grid array with a distance of 5 μm[23]. Individual fluorescent spots were detected and tracked automatically using an established software [24]. In brief, the image sequences were smoothed by calculating the cross-correlation of parts of the images with an ideal 2D Gaussian fluorescent spot to remove noises, including shot noises.

Fluorescent spots were detected based on fluorescence intensity (typical threshold was adjusted to background + 4σ) and spot size (threshold was 9 pixels corresponding to the size of diffraction limited spots). The spot locations were defined with sub-pixel resolution by fitting the spot images with a 2D Gaussian distribution. Fluorescence intensities of the spots were quantified after subtracting local background intensities Tracks were constructed by connecting the spots within consecutive frames. Tracks lasted for two or more than two frames were used for statistical analysis.

3-2-11. Statistical analysis

The fluorescence intensity of the spots and the colocalization time and lateral mobility of the tracks were analyzed statistically using programs written specifically for the purpose on Igor Pro. Colocalization of two fluorescent spots was defined that a spot in one channel was localized within a distance of 240 nm from a spot in the other channel. The localization accuracy of the spots was approximately 35 nm. The overlay accuracy was approximately 30 nm, suggesting that truly colocalized proteins are localized within the threshold distance of 240 nm with probability of approximately 99%[25].

2D-mean square displacement (MSD) was analyzed on tracks with 10 or more frames. 2D-MSD was calculated for each time interval $\Delta t = n\delta t$ ($\delta t = 30$ ms) along with the following equation.

$$\text{MSD}(\Delta t) = \frac{1}{N-1-n} \sum_{i=1}^{N-1-n} \{[x(i\delta t + n\delta t) - x(i\delta t)]^2 + [y(i\delta t + n\delta t) - y(i\delta t)]^2\}$$

In the equation, $x(t)$ and $y(t)$ stand for spot locations at a time t, N denotes the total number of the consecutive frames for the spot, δt represents the frame interval of the single-molecule images. The 2D diffusion coefficient D was calculated from the slope between the second and the fourth points of each MSD-Δt curve by least-square fitting to an equation: MSD = $4D\Delta t$.

The presence of ligand-induced changes in the oligomer fractions and G protein colocalization times was examined with two-tailed paired Student's t-test. The difference in the single-molecule properties depending the chemicals was examined by calculating the chemical-induced changes from before to after treatments, followed by one-way ANOVA and a post-hoc analysis with Dunnett's test. For all analyses, statistical significance was inferred for $p < 0.05$.

3-3. Results

3-3-1. Ligand-induced cluster formation of FPR1

Some GPCRs, such as β2-adrenergic receptor, form clusters after ligand stimulation, whereas some GPCRs, such as β1-adrenergic receptor, do not form clusters[26]. I first examined whether FPR1 form ligand-induced clusters in living HEK293 cells. To monitor the receptor, FPR1 was genetically fused with a self-labeling protein tag, SNAP-tag, at its N-terminus. The SNAP-FPR1 was stably expressed in HEK293 cells and labeled with a green fluorescent dye, SNAP-Alexa488. Using TIRF microscopy, SNAP-FPR1 localized on the cell membrane was monitored from 1 min before to 30 min after ligand stimulation with fMLP (**Fig. 3-2A**). Before ligand stimulation, SNAP-FPR1 exhibited a homogeneous distribution on the cell membrane. No change was observed within 2 min after ligand stimulation. After 5 min, bright immobile fluorescent dots appeared on the cell membrane, indicative of cluster formation of FPR1. The fluorescence intensity of the fluorescent dots gradually increased, whereas the number of the fluorescent dots did not change for 30 min. The cluster formation was not observed when the cells were treated with buffer solution or inhibitors (**Fig. 3-2B**), indicating that the cluster formation is dependent on active conformation of FPR1. The fluorescence intensity of the fluorescent dots revealed that, after background subtraction, the fluorescence intensity of the fluorescent dots was eight times as high as that of the other areas on the cell membrane (**Fig. 3-2C**). Previous reports have suggested that addition of fMLP to neutrophils or polymorphonuclear leukocytes caused clustering of the ligand[27,28,29]. Taken together, ligand stimulation caused the cluster formation of FPR1 independent of cell types.
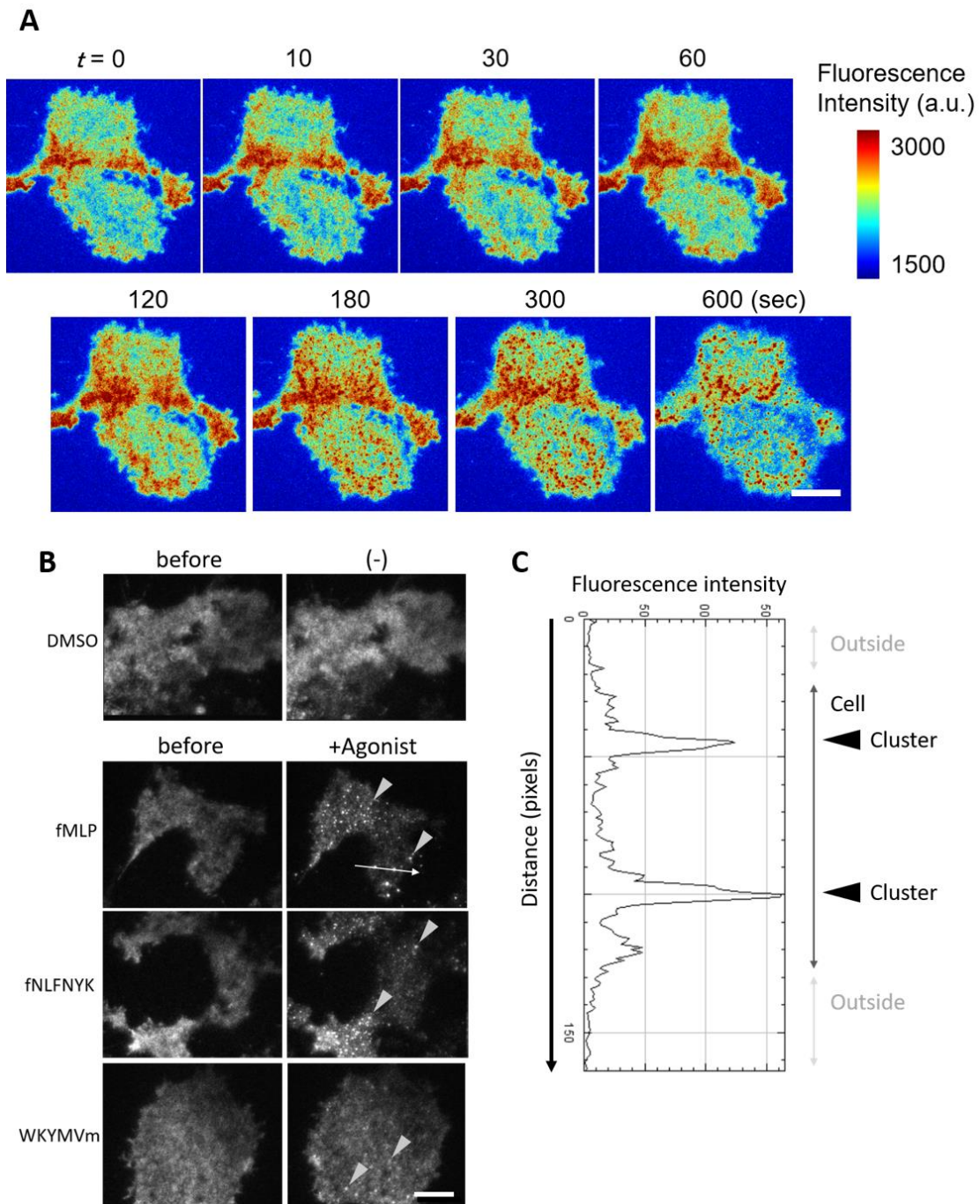
Fig. 3-2. FPR1 cluster formation detected with TIRF microscopy at the low time resolution of 1 s. (A) Pseudocolor time-lapse images of FPR1 upon ligand stimulation. Cell-membrane-localized SNAP-FPR1 was stained with a SNAP-Alexa488 dye and detected with TIRF microscopy. The ligand, fMLP, was applied at $t = 0$. FPR1 was distributed homogenously on the cell membrane, but dot-like cluster formation was observed 120 s (2 min) after ligand stimulation. The clusters were not disappeared and were immobile for more than 10 min, although fluorescence intensity was decreased due to photobleaching of the dye. Scale bar: 10 μm. (B) Cluster formation of FPR1 before and 5 min after

58

agonist treatments. Control medium (DMSO) did not induce cluster formation, whereas three agonists, fMLP, fNLFNYK, and WKYMVm, triggered cluster formation of FPR1. Scale bar: 10 μm. Arrow heads indicate representative clusters. (C) Line profile of the fluorescence intensity of the fMLP-treated cells shown in B (white arrow). The vertical axis indicates position in the fluorescence image, the horizontal axis indicates fluorescence intensity at each position.

To identify roles of the cluster formation in signal transduction, colocalization of the FPR1 clusters with signaling proteins, G protein and β-arrestin, were examined. First, G protein α-i3 subunit (Gαi3), which is one of components of heterotrimeric G proteins, was fused with a self-labeling tag, Halo-tag, to visualize in living cells. Using TIRF microscopy, I observed localizations of SNAP-FPR1 and Gαi3-Halo, which were labeled with SNAP-Alexa 488 and Halo-TMR, respectively (**Fig. 3-3A**). As observed above in **Fig. 3-2**, FPR1 formed clusters 2 min after ligand stimulation. In contrast, Gαi3 exhibited a homogenous distribution and did not form any clusters 15 min after ligand stimulation. Next, β-arrestin was fused with a green fluorescent protein, mNeonGreen, and cotransfected with the SNAP-FPR1. Under TIRF microscopy, I observed localization of β-arrestin and FPR1 (**Fig. 3-3B**). Both FPR1 and β-arrestin formed clusters 2 min after ligand stimulation. Moreover, the clusters of β-arrestin were fully overlapped with the clusters of FPR1 (**Fig. 3-3B**). Taken these results together, ligand-stimulated FPR1 formed protein clusters with β-arrestin.
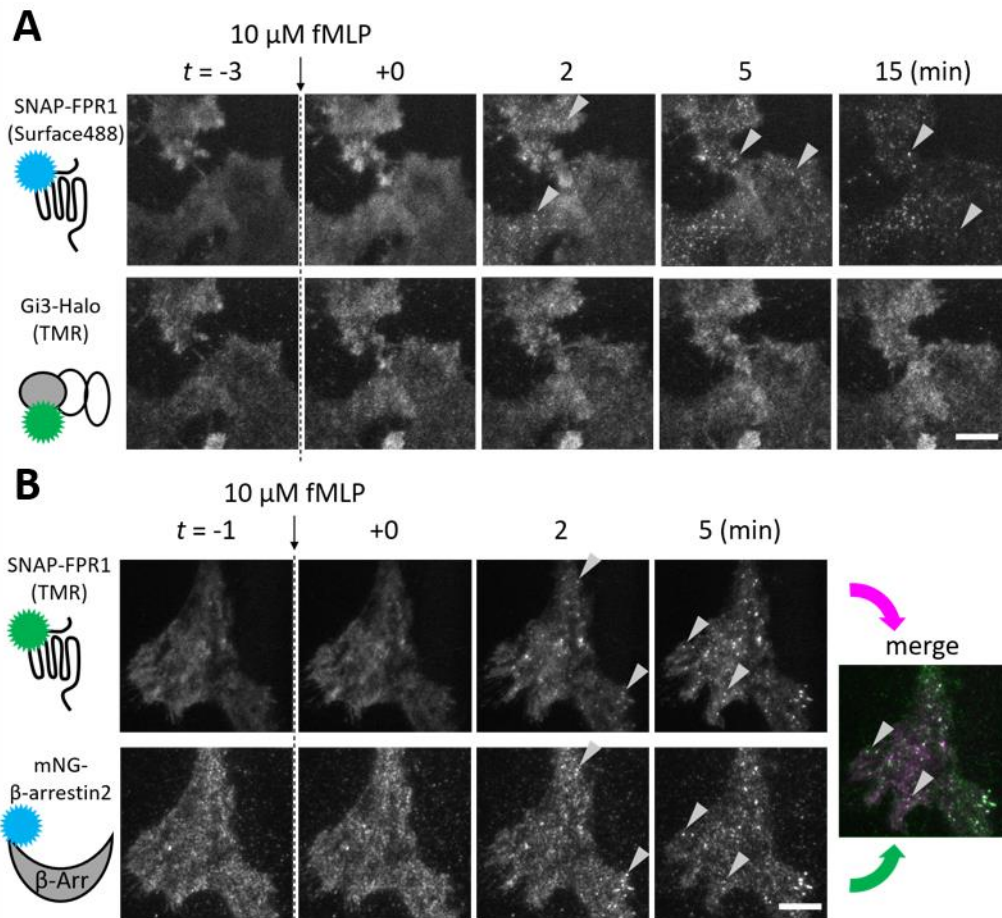
Fig. 3-3. Co-cluster formation of FPR1 with β-arrestin but not with G protein. (A) Dual-color imaging of FPR1 and Gα. Ligand stimulation induced the cluster formation of FPR1 2 min after ligand stimulation, but Gα did not form any complexes. Scale bar: 10 μm. Arrow heads indicate representative clusters. (B) Dual-color imaging of FPR1 and β-arrestin. After ligand stimulation, FPR1 formed clusters, which were fully colocalized with β-arrestin clusters. In the merge image of $t = 5$ min, FPR1 was shown in magenta, and β-arrestin was shown in green. White spots represented the colocalization of FPR1 and β-arrestin. Scale bar: 10 μm. Arrow heads indicate representative clusters.

In previous reports, importance of cholesterol and β-arrestin in the FPR1 cluster formation has been investigated[5,30]. Here, I examined the importance of cholesterol and β-arrestin expression in the ligand-induced cluster formation of FPR1. When membrane cholesterol was removed by treating the cells with methyl-β-cyclodextrin, FPR1 formed clusters 5 min after ligand stimulation in the cholesterol-depleted cells (**Fig. 3-4A**). When SNAP-FPR1 was transiently expressed in an arrestin knock-out HEK293A cells (Arr(-/-)), FPR1 did not form clusters within 5 min of ligand stimulation (**Fig. 3-4B**). Co-transfection of SNAP-FPR1 and β-arrestin-mNeonGreen into the arrestin knock-out cells revealed

60

that FPR1 formed ligand-induced clusters in the presence of β-arrestin expression (**Fig. 3-4C**). Interestingly, transiently expressed β-arrestin formed clusters even before ligand stimulation. The preformed β-arrestin clusters grew up after ligand stimulation and FPR1 clusters colocalized with the β-arrestin clusters, implying that driving force of FPR1 cluster formation might be originated from interactions with β-arrestin. Collectively, cholesterol was dispensable for FPR1 cluster formation, whereas β-arrestin expression was indispensable in HEK293 cells (**Fig. 3-4D**). Xue M. et al. have reported that arrestin-binding-deficient FPR1 mutant (ΔST FPR1) has formed ligand-induced clusters and that cholesterol-depletion has inhibited the cluster formation[5]. Wang J. et al. have reported that ligand-induced cluster formation and subsequent internalization have not been inhibited by clathrin-, caveolae-, actin-, and microtubule-inhibitors, but inhibited by cholesterol depletion[31]. Sitrin R. G. et al. have reported that FPR1 has been localized in the non-raft domain of polymorphonuclear cells and its signal transduction has not been altered after cholesterol removal[32]. These results suggest that FPR1 cluster formation was regulated by molecules and proteins on the cell membrane dependent on the cell types.
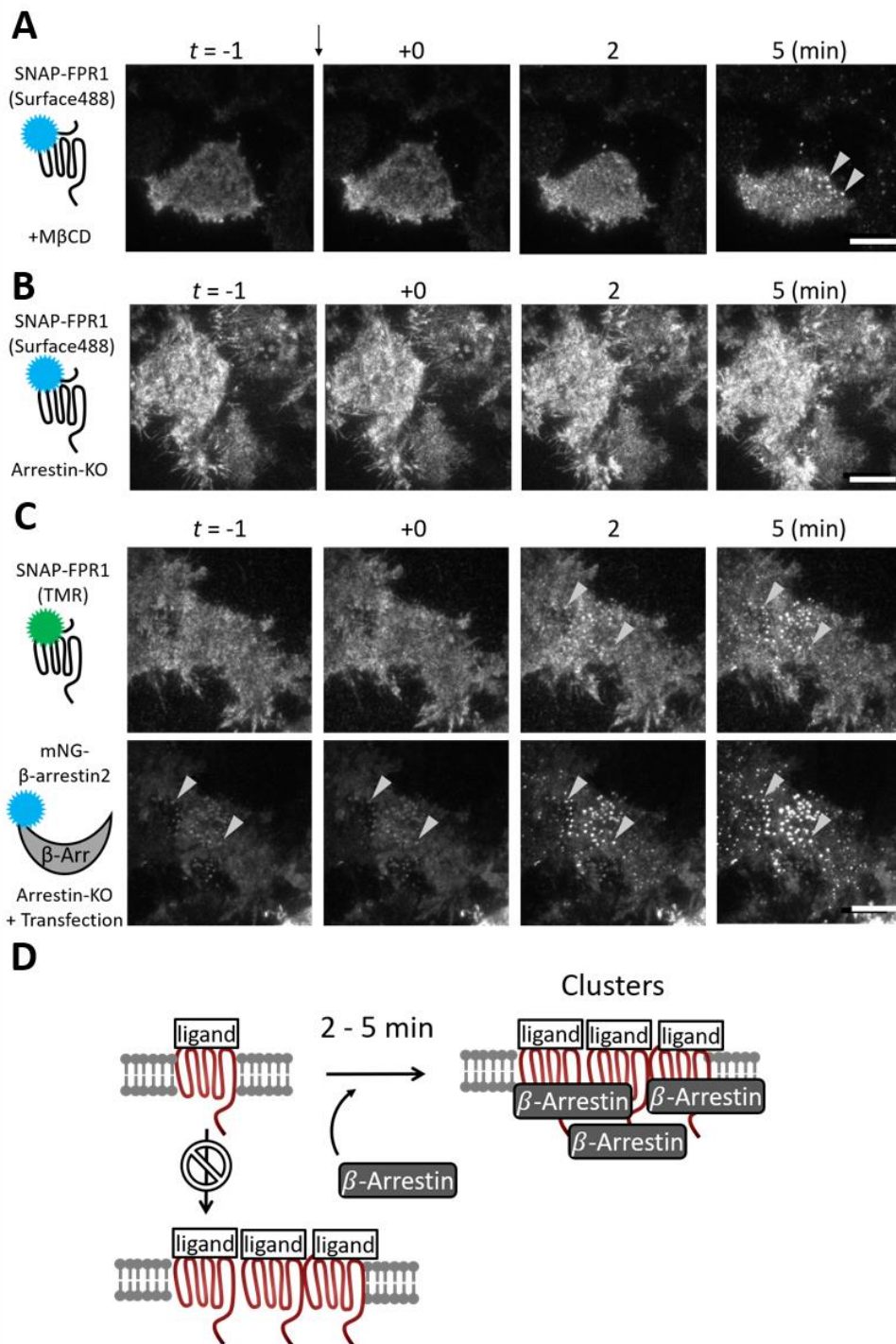
Fig. 3-4. Requirement for FPR1 cluster formation. (A) Cluster formation of FPR1 in cholesterol-depleted cells using methyl-β-cyclodextrin (MβCD). The cluster formation of FPR1 was observed 5 min after ligand stimulation. Arrow heads indicate representative FPR1 clusters. Scale bar: 10 μm. (B) No cluster formation in arrestin-knock out (KO) cells. FPR1 did not form clear clusters upon ligand stimulation. (C) Cluster formation of FPR1 in the arrestin-KO cells transiently expressing fluorescently labeled β-arrestin 2. The cluster formation of FPR1 was observed 2 min after ligand

62

stimulation. The clusters of β-arrestin were also observed and fully colocalized with the FPR1 clusters. The β-arrestin clusters were detected even before ligand stimulation. (D) Summary of the FPR1 cluster formation. FPR1 formed protein clusters that included β-arrestins a few minutes after ligand stimulation. The cluster formation required β-arrestin expression but not required cholesterol. G protein did not form any clusters during signal transduction.

3-3-2. Optimization of single molecule visualization of FPR1 and Gαi3

Ligand stimulation triggered β-arrestin-dependent cluster formation of FPR1 within 2 min, suggesting that β-arrestin-related signal transduction of FPR1 was mediated by the FPR1 clusters. In contrast, G protein did not show any enrichment in the FPR1 clusters, suggesting that G-protein-related signal transduction of FPR1 may not be mediated by the clusters. Considering that G protein signals were triggered earlier than β-arrestin signals (as shown in Section 2), I hypothesized that G protein signals were mediated by smaller FPR1 clusters (or oligomers) which may be formed within 2 min after ligand stimulation. These small FPR1 clusters, typically less than 20 receptors, cannot be identified in conventional imaging as shown in **Fig. 3-2A**. To distinguish FPR1 monomers from FPR1 oligomers, I established multi-color single molecule imaging system.
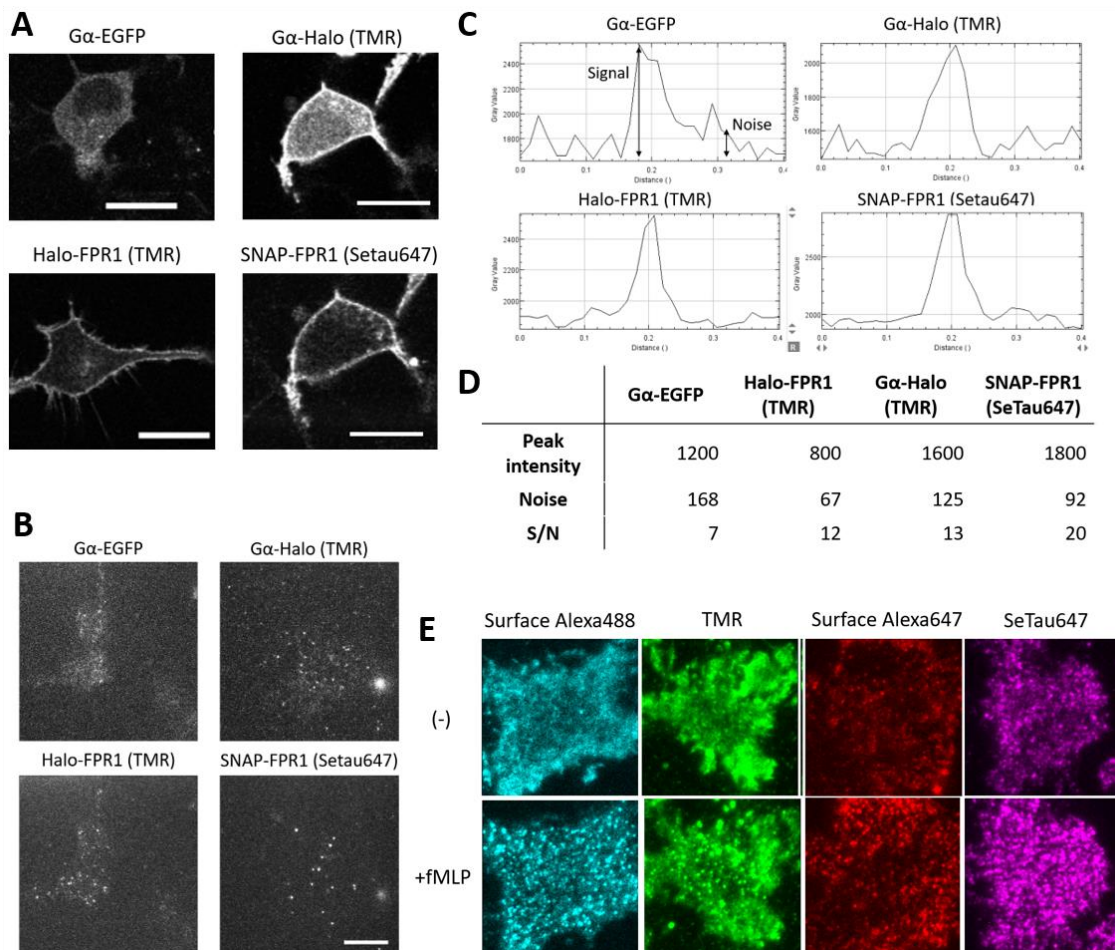
3-3-2-a. Fluorescent dyes

Fluorescent proteins and self-labeling protein tags are used for live-cell single molecule imaging. I first asked whether fluorescent proteins and protein tags are applicable to target proteins, Gαi3 and FPR1. EGFP and Halo-tag were fused in a loop region between the Ras domain and helix domain of Gαi3. Both Gαi3-EGFP and Gαi3-Halo exhibited homogenous cytosolic and membrane distribution under confocal microscopy (**Fig. 3-5A**). The result suggests that introduction of EGFP or Halo-tag did not inhibit the expression and localization of Gαi3. For FPR1, Halo-tag and SNAP-tag were fused at its N-terminus. As expected, both Halo-FPR1 and SNAP-FPR1 exhibited exclusive membrane localization (**Fig. 3-5A**), indicating that SNAP- or Halo-tag did not affect the expression and localization of FPR1.The potencies of SNAP- and Halo-FPR1 in G protein activation were indistinguishable with that of wild-type FPR1 (**Fig. 2-6E** in Chapter 2). From these results, I concluded that labeled FPR1 and Gαi3 behaved as the same as wild-type ones because localization of fluorescence-labeled Gαi3 was the same as that of wild-type Gαi3, whereas localization and function of fluorescence-labeled FPR1 was the same as that of wild-type FPR1.

Optical properties of fluorescent protein, EGFP, and protein tags, Halo-TMR and SNAP-SeTau647, were examined. Under low expression level, all the four probes, Gαi3-EGFP, Gαi3-Halo(TMR), Halo-FPR1(TMR), and SNAP-FPR1(SeTau647), were detected as individual fluorescent spots (**Fig. 3-5B**), validating single molecule detection of fluorescently labeled FPR1 and Gαi3 using TIRF microscopy. Brightness of fluorescent spots was evaluated by signal-to-noise ratio (**Fig. 3-5C**). Fluorescence signal

was defined as mean of peak intensities of the fluorescent spots, whereas background noise was defined as standard deviation of fluorescence intensity outside of the cells. The signal-to-noise ratios were quantified to 7 (EGFP), 12 (TMR), and 20 (SeTau647) (**Fig. 3-5D**). Therefore, the combination of TMR and SeTau647 is superior to the combination of EGFP and TMR. To validate the use of fluorescent dyes, the cells expressing SNAP-FPR1 were labeled with various fluorescent dyes, such as Alexa488, TMR, Alexa647, and SeTau647, and treated with an agonist (**Fig. 3-5E**). After 2 min incubation, all the cells exhibited clear cluster formation of FPR1, suggesting that fluorescent dyes did not alter protein-protein interaction among FPR1. Accordingly, FPR1 was labeled with SNAP-SeTau647, and Gαi3 was labeled with Halo-TMR in two-color single molecule imaging without affecting biophysical properties of the original proteins.

	Gα-EGFP	Halo-FPR1 (TMR)	Gα-Halo (TMR)	SNAP-FPR1 (SeTau647)
Peak intensity	1200	800	1600	1800
Noise	168	67	125	92
S/N	7	12	13	20

Fig. 3-5. Fluorescent labeling of FPR1 and G protein without affecting biophysical properties. (A) Confocal images of FPR1 and G protein fused with fluorescent proteins, EGFP, Halo-tag, or SNAP-tag. Scale bar: 20 μm. (B) Single molecule images of FPR1 and G protein fused with the fluorescent proteins, EGFP, Halo-tag, or SNAP-tag using TIRF microscopy. Scale bar: 5 μm. (C, D) Evaluation of S/N ratios of the single molecule images shown in B. Based on representative line profiles (C), the

fluorescence signals from the dye and the background noises mainly due to shot noises were quantified (D). (E) Cluster formation of SNAP-FPR1 labeled with different dyes. Ligand stimulation with fMLP induced clear cluster formation in the presence of all the four dyes tested.

3-3-2-b. Emission filters

I examined optical properties of five emission filters for SeTau647 channel to maximize fluorescence signal from SeTau647 while minimizing spectral bleed-through of TMR fluorescence. The cells expressing SNAP-FPR1 and Gαi3-Halo were stained with Halo-TMR and SNAP-Setau647, respectively. Using TIRF microscopy, the same cells were observed with five emission filters, 725/40, 732/68, 716/40, 692/40, and 697/58 (the first and second numbers indicate center wavelength and width of the band-pass of each filter, respectively) (**Fig. 3-6A**). When the cells were irradiated by 640 nm laser light, strong fluorescence signals of single molecules of FPR1 were observed for 692/40 and 697/58. When 561 nm laser light was additionally irradiated, background fluorescence intensity was increased, and signal-to-noise ratios were decreased in all the conditions. Importantly, no clear fluorescence spots were additionally detected in the SeTau647 channel after 561 nm excitation, suggesting that the increase in the background noises was caused not by the TMR fluorescence but by non-specific fluorescence from cells and medium. Based on the peak fluorescence intensity and the standard deviation of the background fluorescence intensity, signal-to-noise ratios were quantified (**Fig. 3-6B**). Under single excitation condition, 725/40, 692/40, and 697/58 showed high signal-to-noise ratios, but 725/40 showed poor signal-to-noise ratio under two excitation condition. Therefore, 692/40 and 697/58, which showed acceptable S/N ratio even under two-color excitation condition of more than 2, were suitable for two-color single molecule imaging. The emission spectrum of SeTau647 dye with the maximum fluorescence intensity at 675–710 nm (**Fig. 3-6C**) indicates that the high S/N ratio of 692/40 and 697/58 was mainly provided by high fluorescence signals collected by using the filters.

In addition to FPR1 and Gαi3, I observed ligands using fluorescence labeling in the following section. To achieve three-color single molecule imaging, I used additional dye of OregonGreen, whose excitation wavelength was 488 nm. Here, the cells expressing SNAP-FPR1 (SeTau647) were further observed under three-color excitation condition with 488/561/640 nm lasers (**Fig. 3-6D**). Three filter conditions, 725/40, 732/68, and 697/58, showed almost the same images as those under two-color excitation condition (**Fig. 3-6A**). However, the images were severely affected by the additional 488 nm laser light in the two filter conditions, 716/40 and 692/40. The phenomena would be due to an incomplete optical blockade for the incidental light. Hence, the two filters, 716/40 and 692/40, are not applicable to three-color single molecule imaging. Taken these results together, I chose 697/58 as an emission filter for SeTau647 channel throughout the two- and three-color single molecule imaging.
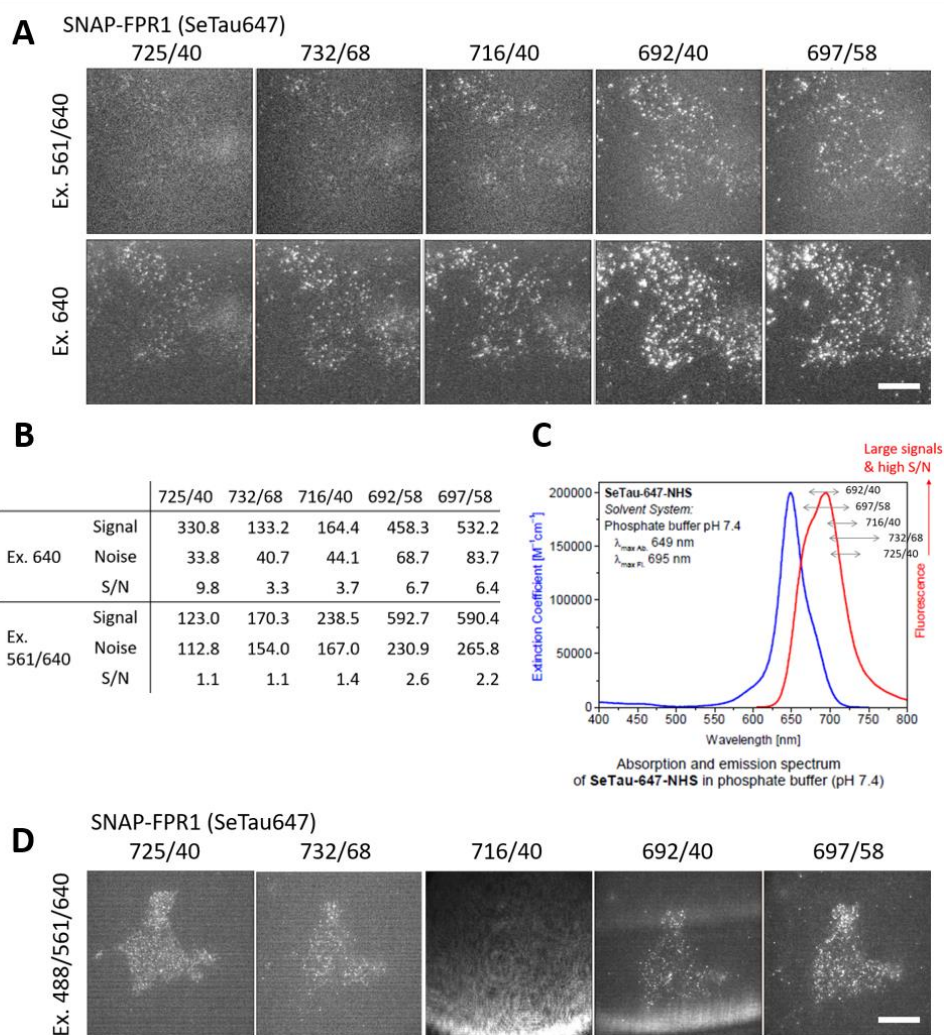
Fig. 3-6. Optimal filters that enable three-color single molecule imaging with a high S/N ratio. (A) Single molecule images of SNAP-FPR1 labeled with SeTau647 under various filters. The cells were irradiated by 560 nm and 640 nm lasers, as indicated. The fluorescence emission was split into TMR channel and SeTau647 channel with a dichroic mirror FF662. The SeTau647 fluorescence was collected with the emission filter as indicated, such as 725/40. The contrasts of the images were adjusted to make the background levels look similar. Scale bar: 10 μm. (B) Signal levels against noise levels for each emission filter. The numbers, such as 725/40, indicated the emission filters, and Ex. 640 and Ex. 561/640 indicated the excitation conditions (640 nm only and 561 + 640 nm light, respectively). (C) Emission spectrum of SeTau647 obtained from the manufacture's data sheet. The band widths of the filters were indicated on the spectrum. The large signal and the high S/N ratio were obtained with the emission filter that fully overlapped with the emission spectrum of SeTau647. (D) Single molecule images of SNAP-FPR1 labeled with SeTau647 irradiated by three lasers, 488 nm, 561 nm, and 647 nm. The fluorescence emission was first split into SeTau647 channel and the others with

66

a dichroic mirror FF662. The contrasts of the images were adjusted to make the background levels look similar. Scale bar: 15 μm.

3-3-2-c. Stable cell lines

The expression levels of the labeled G protein and FPR1 were fixed by establishing a stable expression cell line. First selection of the stable cell lines was performed by monitoring the cells under TIRF microscopy and rejecting the samples with too high or too low expression (**Fig. 3-7A**). In the second selection, the total fluorescence intensity of the TIRF images was quantified to estimate expression levels of the proteins (**Fig. 3-7B**). The cells with the membrane expression levels of 0.1–0.7 molecules/μm^2 were selected because these expression levels provide enough spatial separation between fluorescent spots. Compared to the transiently expressing cells, the variance of the numbers of detectable FPR1 fluorescent spots among the established stable cells was small (**Fig. 3-7C**). The exogenously added protein expression of Gα was further confirmed by western blotting analysis for the C-terminal epitope tag (**Fig. 3-7D**). Unfortunately, the protein expression of FPR1 could not be detected potentially because of too low expression levels for western blot analysis.
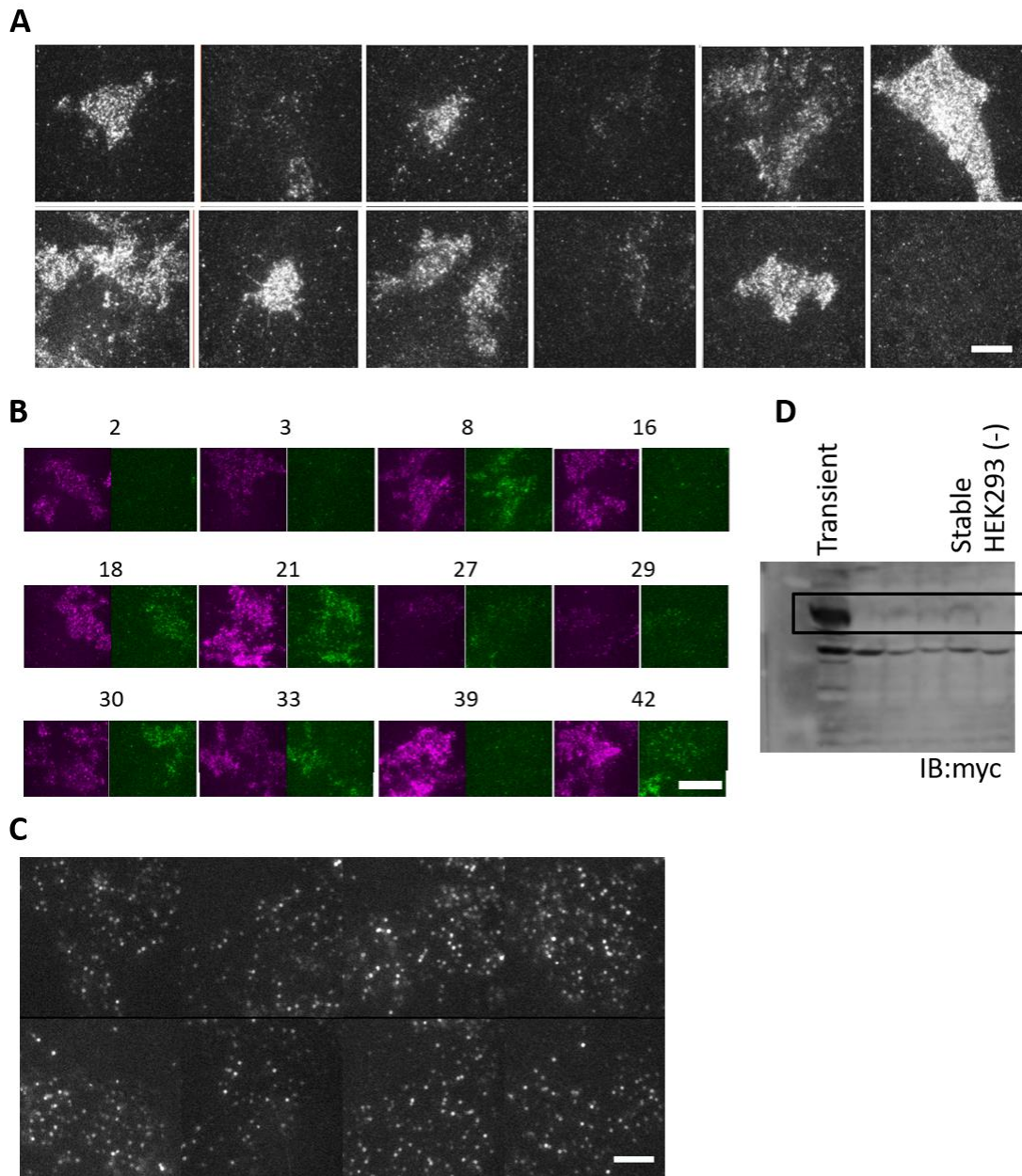
Fig. 3-7. Establishment of stable HEK293 cell line expressing SNAP-FPR1 and Gαi3-Halo. (A) Representative TIRF images of transiently expressed SNAP-FPR1. Scale bar: 10 μm,. (B) Representative TIRF images of stable cell lines. Magenta and green images, respectively, indicate the fluorescence images of SNAP-FPR1 (SeTau647) and Gαi3-Halo (TMR). Some cell lines showed too high expressions (e.g. #21, #39), some showed only limited numbers of fluorescent spots (#27, #29). The cells with appropriate expression levels of both probes (#18) were selected for the following experiments. (C) Representative TIRF images of the cells from the stable cell line #18. Scale bar: 5 μm. (D) Western blotting of Gαi3-Halo detected with the epitope-tag (myc tag). The protein bands for Gαi3-Halo were marked with a solid square. Compared to the transient expression of Gαi3-Halo, the

stable cell lines showed a faint band of Gαi3-Halo, consistent with the low expression level detected under TIRF microscopy.

3-3-2-d. Labeling efficiency

The labeling condition also affects the spot density in the single molecule images and the interpretation of the results. To estimate the labeling efficiency, the stable cells were stained with different concentrations of the fluorescent dye and the total fluorescence intensity from cell membrane was quantified (**Fig. 3-8**). At low concentration of the dye, each spot represented a single step photobleaching, indicating the single molecule detection (**Fig. 3-8A**). Dose–response curve for the labeling dye was fitted with a sum of a specific and non-specific binding curves (**Fig. 3-8B**). The fitting curve demonstrated that 16% of the SNAP-FPR1 were labeled with SeTau647 with negligible non-specific labeling at 50 nM SeTau647-PEG-BG staining. Under the low labeling efficiency, the density of the SNAP-FPR1 fluorescent spots was 0.3 spots/μm^2, indicating that the total expression level of SNAP-FPR1 in the established HEK293 cells was 1.9 molecules/μm^2, which was almost the same as the physiological condition, such as neutrophils (2.1 molecules/μm^2)[33]. The labeling efficiency of Halo-TMR was not determined and the labeling condition was simply optimized to obtain good spatial separation of the fluorescent spots. This is because quantitative evaluation of G protein stoichiometry in the assay is not possible due to a substantial amount of endogenous G proteins in HEK293 cells.
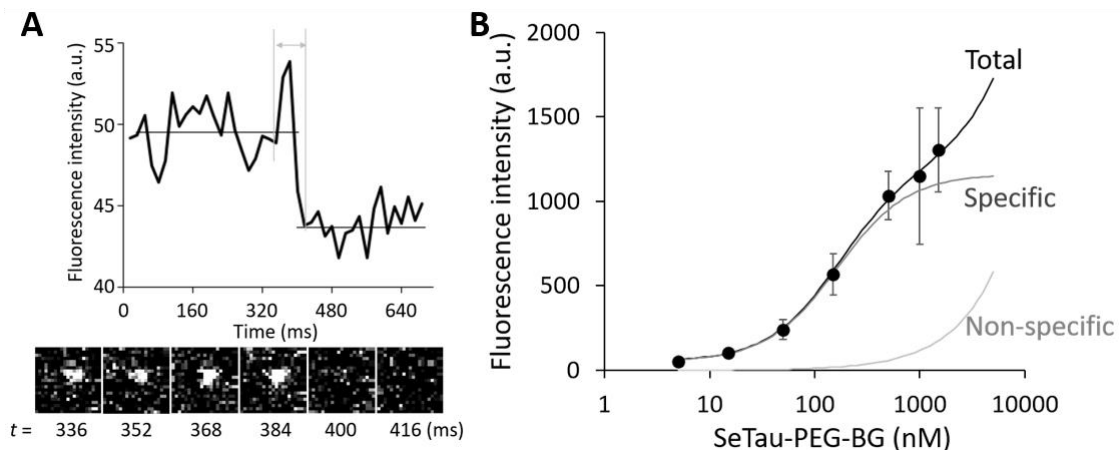

Fig. 3-8. Validation of single molecule detection using SNAP-SeTau647. (A) A typical temporal change of fluorescence intensity of a fluorescent spot. The fluorescent spot showed a constant fluorescence intensity at $t = 0$–384 (ms), and suddenly disappeared at $t = 400$ (ms). This single step photobleaching indicated the presence of single fluorescent molecule. (B) Total fluorescence intensity of cells labeled with various concentrations of SNAP-SeTau647. A rapid increase in fluorescence intensity at intermediate concentrations and a linear increase at high concentrations suggested the

presence of a specific and non-specific labeling of the cells. Specific and nonspecific components of the binding were extracted by fitting the curve with a sum of a Hill equation and a linear curve: *Fluorescence intensity = a [Dye] + bottom + (top – bottom) / (1 + (EC50 / [Dye]) ^ b)*. Details are presented in Materials and Methods. Fitted parameters were the following: $a = 0.15 \pm 0.12$, *bottom* = 54 ± 36, *top* = 1103 ± 218, *EC50* = 158 ± 45 (nM); $b = 1.42 \pm 0.40$ (mean ± s.d.). The fitting results were shown as solid lines. Data are presented as mean ± s.e.m. (n = 8, 8, 8, 8, 16, 4, and 11 cells, respectively, for concentrations of 5, 15, 50, 150, 500, 1000 and 1500 nM).

3-3-2-e. Evaluation of the size of oligomers observed by single molecule imaging

I compared the distribution of fluorescence intensity of FPR1 spots under low and high labeling efficiencies of the SNAP-tag to estimate the numbers of FPR1 in each fluorescent spot. Without ligand stimulation, the distribution was skewed with a single peak and a long tail in the higher fluorescence intensity region (**Fig. 3-9A**). The fluorescence intensity at the peak under the low labeling efficiency was practically the same as that of single fluorescent dyes adsorbed on a glass-based dish. This result indicates that one fluorescence-labeled receptor was included in each FPR1 spot with the fluorescence intensity. Under a high labeling efficiency of 80%, the distribution of fluorescence intensity of FPR1 spots demonstrated the presence of fluorescent spots with high fluorescence intensity (more than 10 times of that of the single fluorescent dye), indicating large oligomer formation of FPR1 (**Fig. 3-9A**). The numbers of FPR1 in each fluorescent spot were estimated by fitting the distribution with multiple Gaussian distributions (**Fig. 3-9B**). The distribution under the high labeling efficiency was fully described with 7 Gaussian peaks, suggesting the presence of FPR1 oligomers containing 1, 2, 3, 4, 5, 6, and 11 receptors (**Fig. 3-9C**). Accordingly, the principle components of FPR1 oligomers were dimers, trimers, tetramers, and hexamers. In earlier reports, the frequencies of incidental overlaps among fluorescent spots were small (< 15%) under the moderate spot density of 1.5 spots/μm^2 [10,13], suggesting that the estimated size of oligomers was not affected by coincidental overlaps. Next, I assumed that the fitting results at the 80% labeling efficiency represented the true oligomer compositions, and that under the low labeling efficiency of 16% FPR1 was randomly labeled with a probability of (16% / 80% = 1/5). Based on the assumptions, I estimated the numbers of total receptors in each fluorescent spot under the low labeling efficiency of 16% from the detected numbers of fluorescently labeled receptors (**Fig. 3-9D**). More than half of fluorescent spots with one fluorescently-labeled receptor under the low labeling efficiency were assigned to be "small oligomers", such as dimers, trimers, and tetramers. In contrast, more than half of fluorescent spots with two or more fluorescently-labeled receptors were "large oligomers", such as pentamers or larger oligomers. Accordingly, fluorescence intensity analysis of FPR1 spots under low labeling efficiency, such as shown in **Fig. 3-9A**, revealed an equilibrium between the small and large oligomers of FPR1.
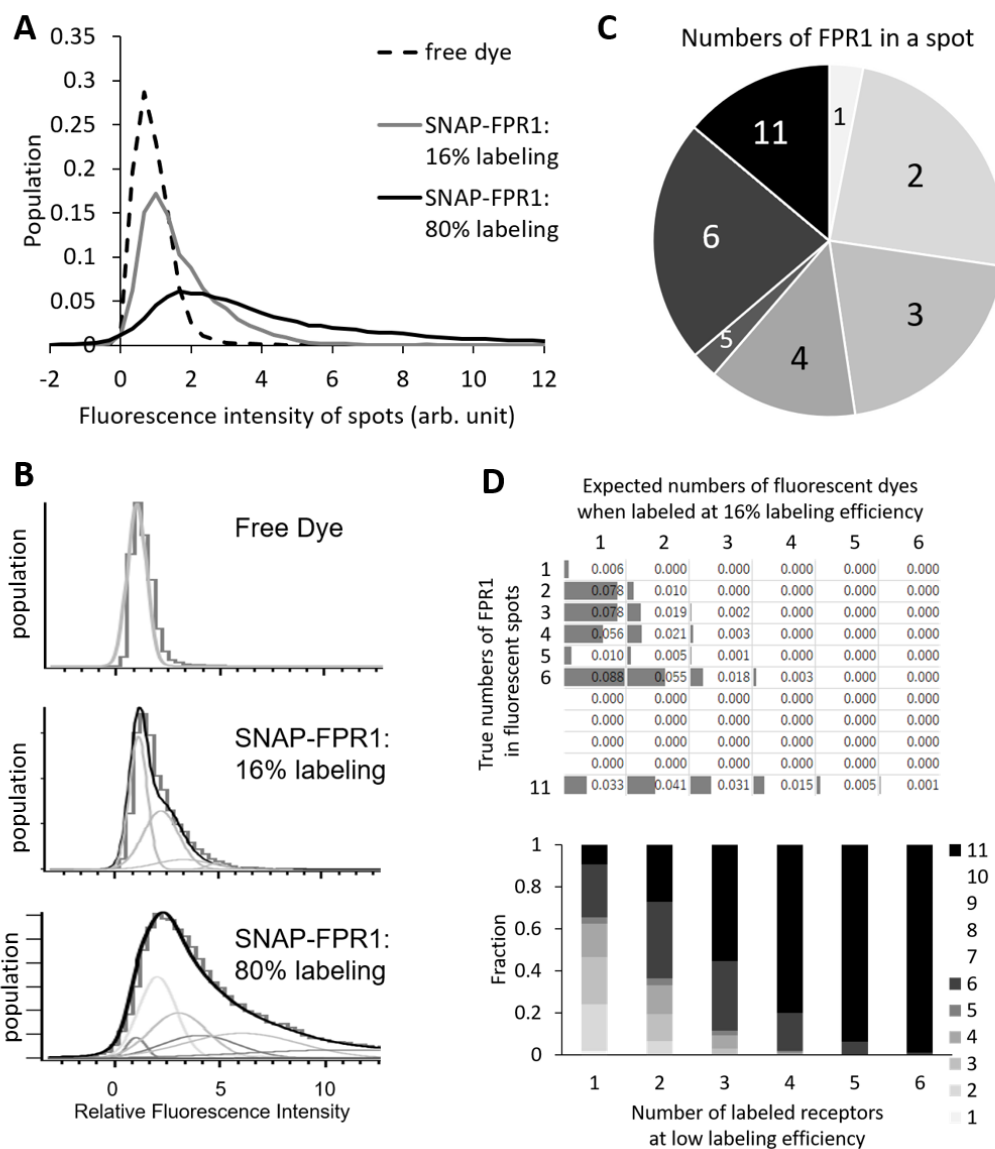
Fig. 3-9. Calibration of the size of FPR1 oligomers based on the fluorescence intensity of fluorescence spots under low labeling efficiency. (A) Fluorescence intensity histograms of SeTau647 fluorescent spots. The dye was adsorbed onto the glass dish or was specifically attached to SNAP-FPR1 in the cells with the labeling efficiency of 16% and 80%. (B) Multi-Gaussian peak fitting of the histograms in A. Free dye was simply fitted with one Gaussian peak. The histograms of SNAP-FPR1 (SeTau647) were fitted with Gaussian peaks whose mean intensity and width were n-fold of that of the free dye distribution. (C) The estimated numbers of FPR1 in each fluorescent spot under the high labeling efficiency (80%). More than half of the fluorescent spots included four or less FPR1, whereas the others included five, six, or eleven FPR1. (D) Estimation of the numbers of labeled receptors under low labeling efficiency (16%) based on the population in C. First, the numbers of labeled receptors in each FPR1 oligomer was calculated in each row by assuming that FPR1 was stochastically labeled

71

with the probability of (16%/80%) = 0.2. Next, the numbers of fluorescent spots that include the same numbers of labeled receptors were summed up in each column. After normalization in each column, I calculated the relation of the number of labeled receptors detected under low labeling efficiency with the true number of FPR1 in the fluorescent spots.

3-3-3. FPR1 Oligomers stabilized by full agonist stimulation

I evaluated changes in the size of FPR1 oligomers upon ligand stimulation (**Fig. 3-10A**). In the absence of ligands, fluorescence intensity of FPR1 spots showed a skewed distribution with a single peak and a long tail in the higher fluorescence intensity region as described above (**Figs. 3-9A, 3-10B**). This broad distribution suggested the presence of FPR1 oligomers even before ligand stimulation. A full agonist, fMLP, reduced the peak height accompanied with an increase in the fraction of the spots in the right tail region of the distribution (**Fig. 3-10B**). This change suggests the oligomerization from small oligomers to large oligomers. Based on the distribution of fluorescence intensity, the fluorescent spots were classified into small and large oligomers (**Fig. 3-10C**). The large oligomer fraction of FPR1 was increased from $65.9 \pm 1.7\% – 71.5 \pm 1.6\%$ ($p = 3 \times 10^{-7}$) within 1 min. I also applied three other ligands, including one agonist, WKYMVm, and two inhibitors, cyclosporin H (CysH), and methionine benzimidazole 6 (MB6) (**Fig. 3-10D**). All the compounds did not show significant changes, although WKYMVm and CysH treatments showed weak trends of increasing numbers of the large oligomers. Note that the size of the large oligomers (5–11 receptors) was yet smaller than clusters (approximately 20 receptors) and the time course after ligand stimulation was also distinct (<1 min vs. >5 min). Hence, this single molecule result showed a ligand-induced large oligomer formation that was different from the β-arrestin-dependent cluster formation observed above, such as in **Fig. 3-2A**.

Previously, actin filament[34], dynamin[28], and cholesterol[5,35] have been reported to be involved in the trafficking and signal transduction of FPR1[36]. I examined changes in the oligomer fraction of FPR1 in the presence of cytochalasin D, Dyngo4a, and methyl-β-cyclodextrin, which inhibit actin polymerization, dynamin-mediated endocytosis, and cholesterol enrichment, respectively. All the three compounds inhibited the fMLP-induced large FPR1 oligomer formation (**Fig. 3-10E**). In contrast, the full agonist increased the large FPR1 oligomers from $67.3 \pm 1.7\%$ to $72.6 \pm 1.6\%$ ($p = 3 \times 10^{-8}$) in the presence of a Gαi inhibitor, PTX. Based on the cytosolic cAMP concentrations, I confirmed that all the four chemicals inhibited the fMLP-induced Gαi signaling (data not shown). These results suggest that the ligand-induced large FPR1 oligomer formation required the actin network, endocytosis, and physiological lipid composition, but not the binding with Gαi. In contrast, signal transduction required all of them.
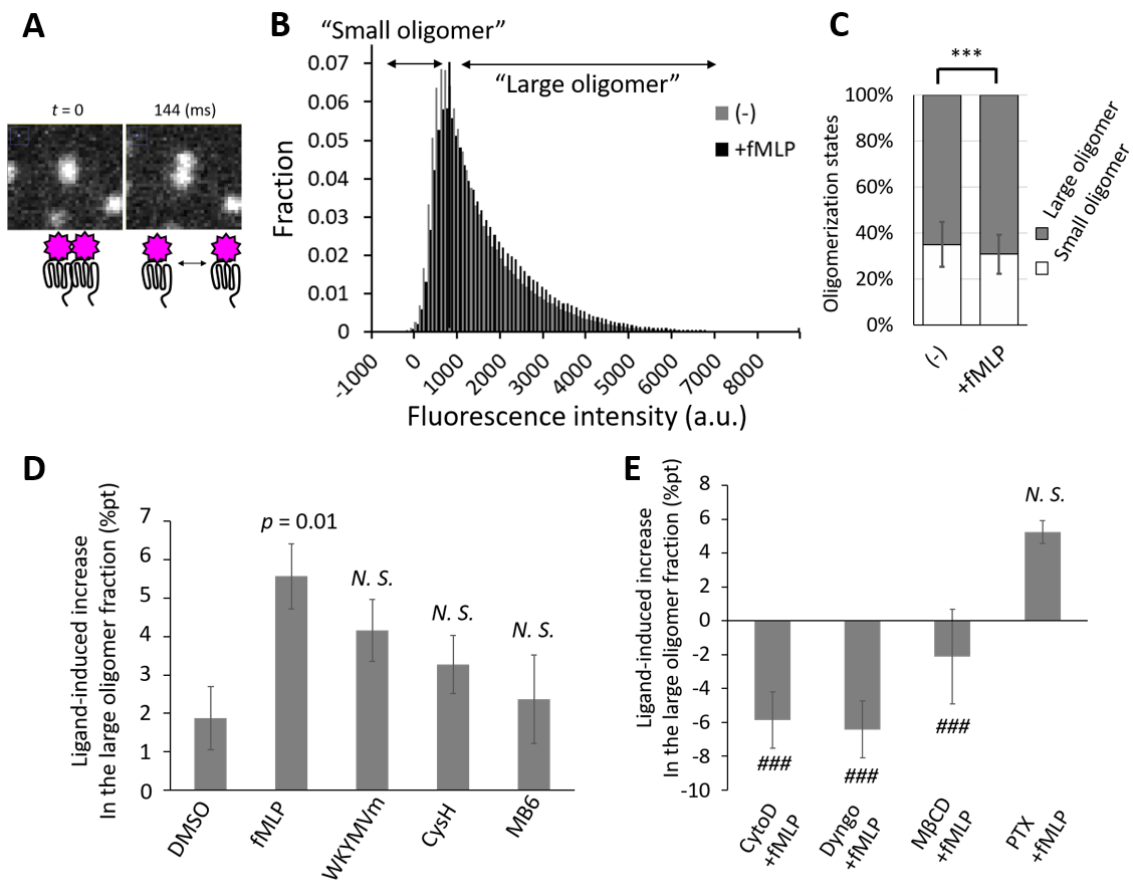
Fig. 3-10. Large oligomer formation of FPR1 after ligand stimulation. (A) Representative single molecule images of FPR1 dissociating into smaller oligomers. The numbers of fluorescent dyes in the spots can be estimated by monitoring the association and dissociation of fluorescent spots or measuring the fluorescence intensity of the spots. (B) Histograms of fluorescence intensity of the FPR1 fluorescent spots detected under single molecule imaging. Upon ligand stimulation (black), the peak height of the distribution was decreased, and population of the right tail was increased compared to that without ligand stimulation (gray). The distribution was split into two groups, small oligomers and large oligomers. The threshold fluorescence intensity at 1.5 times of the fluorescence intensity of single fluorescent dyes was shown as a vertical line. (C) Fractions of the small and large FPR1 oligomers. Mean ± s.d. $n = 29$. The presence of ligand-induced change was examined using a paired Student t-test., ***: $p < 0.001$. (D) Ligand induced changes in the large oligomer fractions in response to agonists, fMLP and WKYMVm, and inhibitors, CysH and MB6. Mean ± s.d. $n = 20$–29. The presence of ligand-induced changes against the control experiment (DMSO) was examined using Dunnett's test, $N.S.: p > 0.1$. (E) fMLP induced changes in the large oligomer fraction in the presence of signal inhibiting molecules, CytoD, Dyngo, MβCD, and PTX. Mean ± s.d. $n = 12$–27. The presence

of inhibitory effect of the added compounds against control experiment (only fMLP treatment shown in D) was examined using Dunnett's test, ###: $p < 0.001$, *N.S.*: $p > 0.1$.

3-3-4. Prolonged FPR1 oligomer-Gαi3 interaction induced by the full agonist

Next, I examined the changes in the activity of FPR1 by measuring the duration time of FPR1-Gαi3 interaction with dual-color single-molecule imaging techniques. I defined that fluorescent spot pairs of FPR1 and Gαi3, with distance located within 240 nm in the same frame, were regarded as colocalized (**Fig. 3-11A**). Typically, I found 14,000 FPR1 spot trajectories, 12,000 Gαi3 trajectories, and 700 colocalization pairs in a 3-s single molecule image. I characterized the colocalization patterns by monitoring a survival distribution of the FPR1-Gαi3 colocalization time (**Fig. 3-11B**). The distribution was fitted with a single-component exponential curve to obtain a time constant for the colocalization. The full agonist stimulation increased the colocalization duration from 34.4 ± 1.1 ms to 38.4 ± 1.0 ms ($p = 0.005$) (**Fig. 3-11C**). The result indicates that the FPR1-Gαi3 interaction was at least partially stabilized by the full agonist. In contrast, no change was observed in the FPR1-Gαi3 interaction time with other chemical treatments such as WKYMVm, CysH, or MB6 (**Fig. 3-11D**). FPR1 possessed a high affinity to Gαi3 after the full agonist treatment.

In the presence of the signal inhibiting chemicals such as cytochalasin D, Dyngo4a, and PTX, fMLP-induced increase in the Gαi3 colocalization duration was reduced to less than 1.5 ms (**Fig. 3-11E**), although methyl-β-cyclodextrin did not reduce it. Previous reports have demonstrated that PTX treatment caused the inhibition of GPCR signal transduction by inhibiting the binding of G proteins to GPCRs[37], supporting our observations. These results imply that FPR1-Gαi3 interaction time increased only when FPR1 formed a signaling-competent structure.

Here, I examined incidental colocalizations by monitoring colocalization events of FPR1 spots with Gαi3 spots shifted horizontally[23]. I observed an abrupt decrease in the number of colocalization events when the spots were shifted by larger than 3 pixels (240 nm), indicative of the detection of the specific interactions between FPR1 and Gαi3 (data not shown). The specific binding events of FPR1 with Gαi3 occurred even before ligand stimulation. After ligand stimulation, the number of FPR1 spots was not increased (**Fig. 3-11F**), whereas the number of Gαi3 spots and colocalization events were increased (**Figs. 3-11G, H**), suggesting that FPR1 activation triggered the membrane localization of Gαi3. I also examined the on-rate of FPR1-Gαi3 interaction, but there were no significant changes upon ligand treatments (**Fig. 3-11I**). These results indicated that the FPR1 activation reduced the dissociation rates and increased the residency times of Gαi3 to FPR1 and the cell membrane.
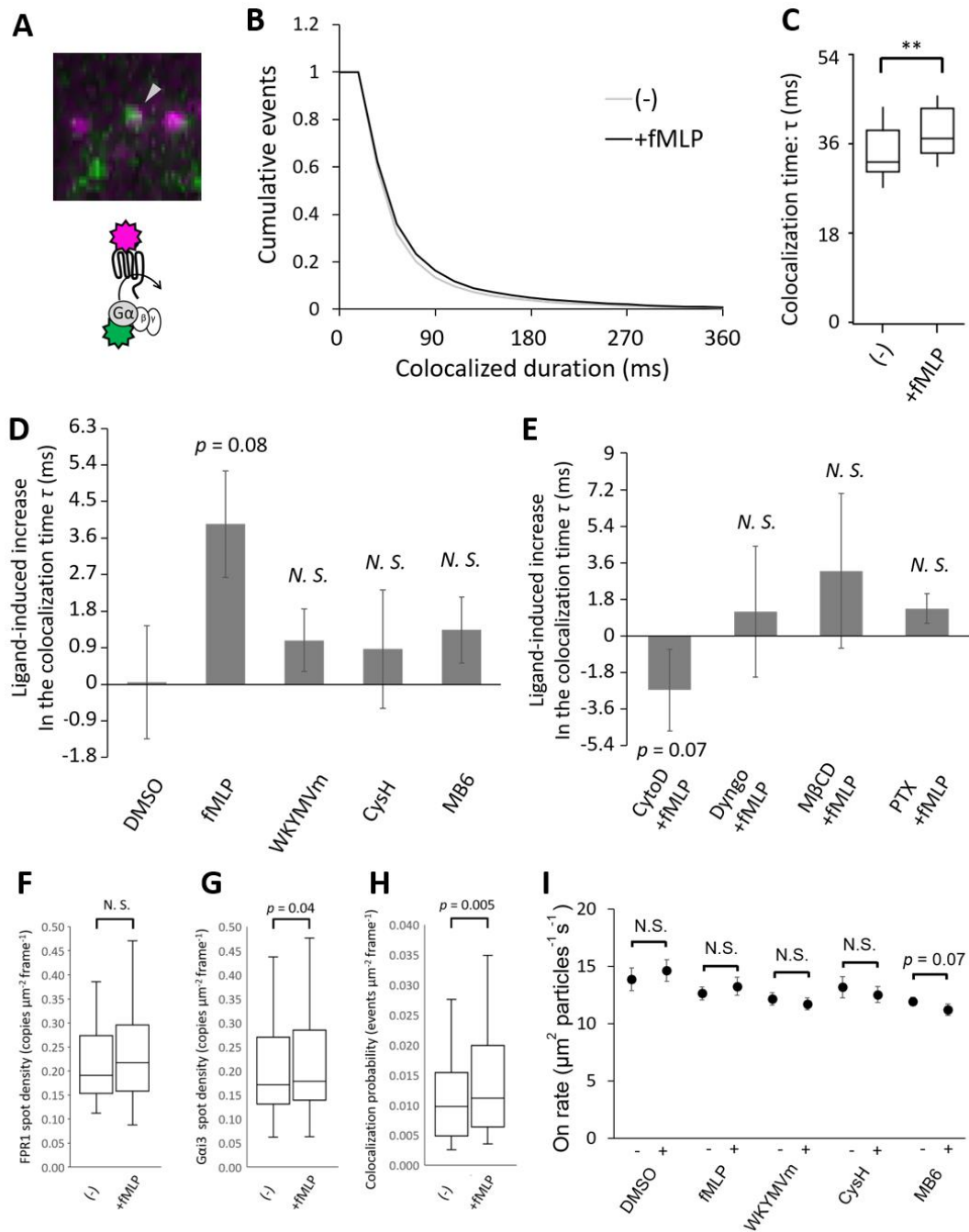
Fig. 3-11. Elongation of colocalization duration of FPR1 with Gαi3 after ligand stimulation. (A) Typical colocalization events of FPR1 (magenta) with Gαi3 (green). (B) Survival distributions of the Gαi3 colocalization time. (C) Colocalization durations calculated by fitting the survival distributions shown in B with single-component exponential curves. The colocalization durations are shown as box plots (whisker, 10–90%; box, 25–75%; bar, 50%). $n = 29$. The presence of ligand-induced change was examined using a paired Student t-test, **: $p < 0.01$. (D) Ligand-induced changes in colocalization durations. Mean ± s.d. $n = 20$–29. The presence of ligand-induced changes against the control

75

experiment (DMSO) was examined using Dunnett's test, *N.S.*: $p > 0.1$. (E) fMLP induced changes in the colocalization duration in the presence of signal inhibiting molecules, CytoD, Dyngo, MβCD, and PTX. Mean ± s.d. $n = 12$–27. The presence of inhibitory effect of the added compounds against control experiment (only fMLP treatment shown in D) was examined using Dunnett's test, *N.S.*: $p > 0.1$. (F) The numbers of membrane localized FPR1 spots in 3-s single molecule movies shown as box plots (whisker, 10–90%; box, 25–75%; bar, 50%). $n = 29$ (cells). (G) The numbers of membrane localized Gαi3 spots in 3-s single molecule movies shown as box plots (whisker, 10–90%; box, 25–75%; bar, 50%). $n = 29$. (H) The numbers of the colocalization events of Gαi3 with FPR1 in 3-s single molecule movies shown as box plots (whisker, 10–90%; box, 25–75%; bar, 50%). $n = 29$. (I) On rates of the FPR1-Gαi3 interaction in the presence of agonists and inhibitors. The on rates were calculated by following the equation: [on rate] = [colocalization events] / ([non-colocalized FPR1 spots] × [non-colocalized Gαi3 spots]). All the numbers were normalized by the area of the cells and the duration of the observations. Mean ± s.e.m. $n = 20$–29. The presence of ligand-induced change was examined using a paired Student *t*-test, *N.S.*: $p > 0.1$.

I further investigated the FPR1-Gαi3 interaction with regards to the FPR1 small and large oligomer states. The Gαi3 interactions with the small FPR1 oligomers were distinguished from those with the large FPR1 oligomers based on the fluorescence intensities of the FPR1 spots (**Figs. 3-12A, D**). The full agonist stimulation increased the small FPR1 oligomer-Gαi3 colocalization time by 2.4 ms (**Figs. 3-12B, C**) and the large FPR1 oligomer-Gαi3 colocalization time by 3.9 ms (**Figs. 3-12E, F**). The inhibitors did not induce any changes (**Fig. 3-12G**). From the results, the full agonist treated FPR1 might have high affinity for Gαi3, especially for the large FPR1 oligomers. However, these agonist-induced increases were not significantly different from that of vehicle treatment. Ligand-free FPR1 coexisting with ligand-bound FPR1 in the full agonist-treated cells might blunt any differences between ligand-bound and ligand-free FPR1 in their binding affinity toward Gαi3.
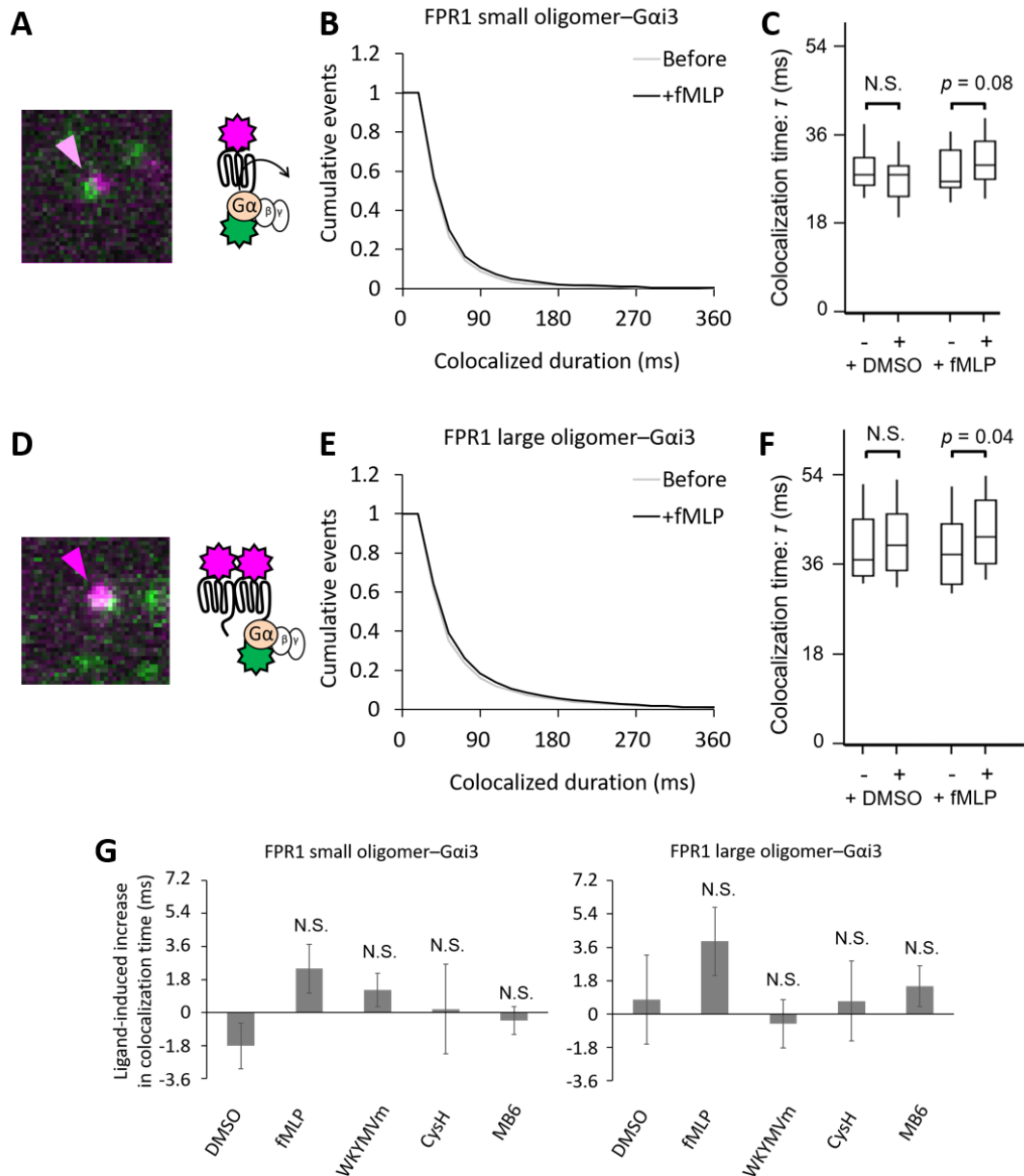
Fig. 3-12. Colocalization times of Gαi3 with small FPR1 oligomers and large FPR1 oligomers. (A) Typical colocalization event of Gαi3 (green) with a small FPR1 oligomer (magenta). (B) Survival distributions of the Gαi3 colocalization time with small FPR1 oligomers. (C) Colocalization durations calculated by fitting the survival distributions shown in B with single-component exponential curves. The colocalization durations are shown as box plots (whisker, 10–90%; box, 25–75%; bar, 50%). n = 20, 29. The presence of ligand-induced change was examined using a paired Student t-test. (D) Typical colocalization event of Gαi3 with a large FPR1 oligomer. (E) Survival distributions of the Gαi3 colocalization time with large FPR1 oligomers. (F) Colocalization durations calculated by fitting the survival distributions shown in E with single-component exponential curves. The colocalization durations are shown as box plots (whisker, 10–90%; box, 25–75%; bar, 50%). n = 20, 29. The presence

of ligand-induced change was examined using a paired Student *t*-test. (G) Ligand-induced changes in colocalization durations for the small and large FPR1 oligomers. Mean ± s.d. *n* = 20–29. The presence of ligand-induced changes against the control experiment (DMSO) was examined using Dunnett's test.

3-3-5. Ligand effects on the stabilization of FPR1-Gαi3 interaction

Even in the full agonist-treated cells, ligand-bound FPR1 coexisted with ligand-free FPR1. Here, the cells were treated with a fluorescently-labeled agonist, fNLFNYK-TMR, to identify ligand-bound FPR1 (**Fig. 3-13A**). Gαi3-Halo was labeled with another organic dye, Halo-R110, to avoid spectral overlap. SNAP-FPR1 was labeled with SeTau647-PEG-BG at a higher labeling efficiency of 48 ± 10% to increase the number of colocalization events detected under TIRF microscopy (**Fig. 3-8B**). Under such modified conditions, SNAP-FPR1, Gαi3-Halo, and fNLFNYK-TMR were detected simultaneously as fluorescent spots diffusing on the cell membrane. The ligand, fNLFNYK-TMR, may be nonspecifically bound on the glass surface. I found that those nonspecifically-bound fNLFNYK-TMR showed low (or practically no) mobility during the observation. Hence, FPR1-bound ligands were identified based on lateral mobility of the fluorescent spots. I defined that FPR1 colocalizing with fNLFNYK-TMR for 150 ms or longer was ligand-bound FPR1. The agonist binding would be irreversible during the observation period of 3 s because of the slow dissociation time constant of the agonist from FPR1 (10–100 s)[38]. Distribution of fluorescence intensity of the ligand-bound FPR1 spots was again skewed with a single peak and a right tail (**Fig. 3-13B**). Quantitative analysis of the fluorescence intensity revealed that the ligand binding slightly shifted the small–large oligomer equilibrium toward the large oligomer state (**Fig. 3-13C**). As for FPR1-Gαi3 interaction, ligand binding prolonged the colocalization time from 47.5 ± 0.9 ms to 61.7 ± 2.6 ms on average (by 14 ms, *p* = 0.0003, **Figs. 3-13D, E**). Importantly, ligand binding to large FPR1 oligomers increased colocalization time by 18 ms (49.4 ± 1.3 vs. 67.6 ± 5.1 ms, *p* = 0.005, **Fig. 3-13G**), whereas ligand binding to small FPR1 oligomers did not cause significant elongation of colocalization duration (45.6 ± 0.9 vs. 55.4 ± 4.4 ms, *p* = 0.052, **Fig. 3-13F**) (**Fig. 3-13H**). Considering these results, I concluded that, among all the four FPR1 states (ligand-free small oligomers, ligand-free large oligomers, ligand-bound small oligomers, ligand-bound large oligomers), the ligand-bound FPR1 large oligomers were the most potent activator of Gαi3 by interacting stably with Gαi3.
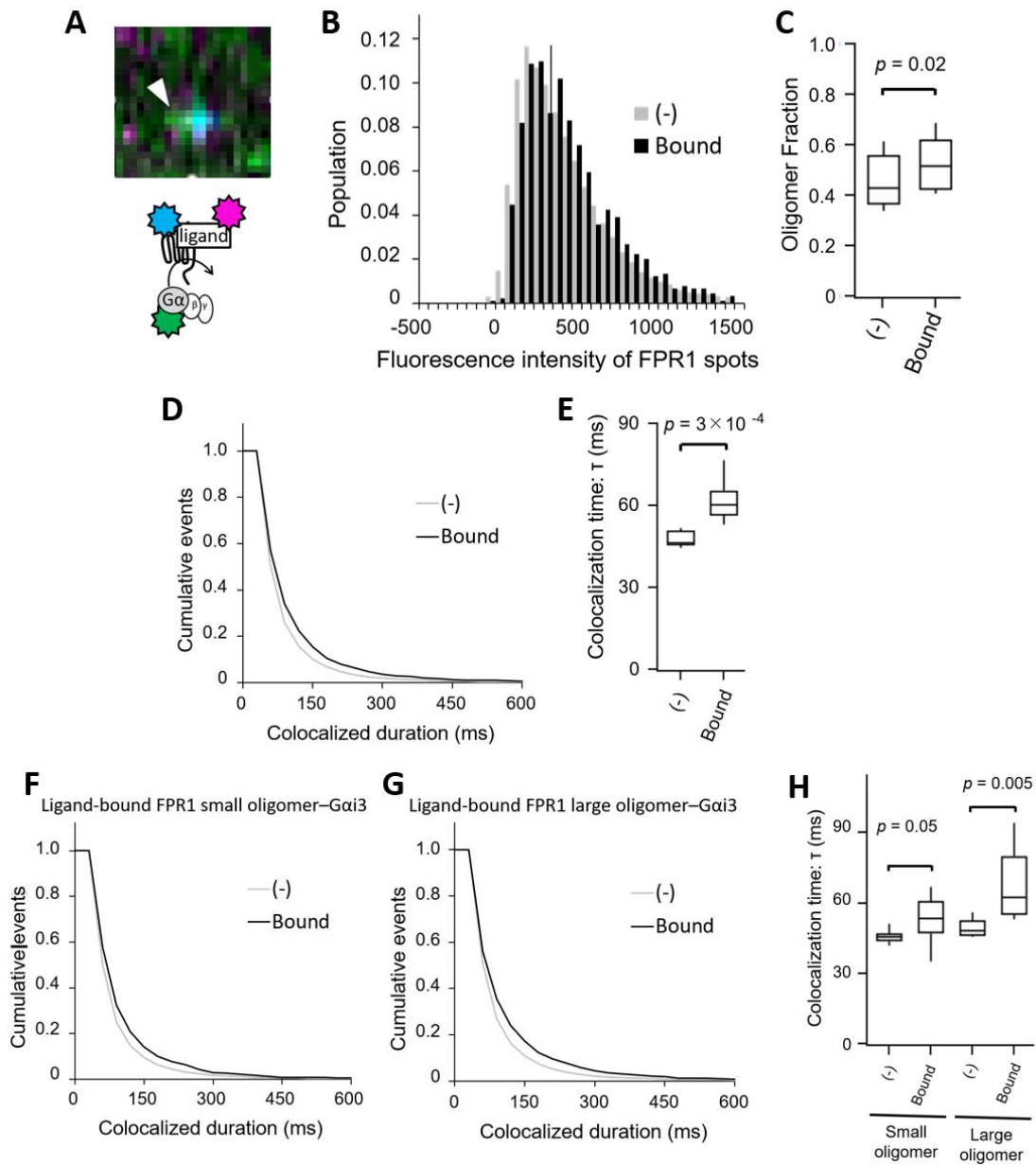
Fig. 3-13. Prolonged Gαi3-interaction at the ligand-bound large FPR1 oligomers. (A) Typical colocalization events of Gαi3 (green) with ligand-bound (magenta) FPR1 (cyan). (B) Histograms of fluorescence intensity of the FPR1 fluorescent spots. (C) Fractions of the large FPR1 oligomers shown as box plots (whisker, 10–90%; box, 25–75%; bar, 50%). $n = 8$ (batches). The presence of ligand-induced change was examined using a paired Student t-test. (D) Survival distributions of the Gαi3 colocalization time with ligand-bound and ligand-free FPR1. (E) Colocalization durations calculated by fitting the survival distributions shown in D with single-component exponential curves. The colocalization durations are shown as box plots (whisker, 10–90%; box, 25–75%; bar, 50%). $n = 8$. The presence of ligand-induced change was examined using a paired Student t-test. (F, G) Survival

distributions of the Gαi3 colocalization time with ligand bound small (F) and large (G) FPR1 oligomers. (H) Colocalization durations calculated by fitting the survival distributions shown in F and G with single-component exponential curves. The colocalization durations are shown as box plots (whisker, 10–90%; box, 25–75%; bar, 50%). $n = 8$. The presence of ligand-induced change was examined using a paired Student t-test.

3-4. Discussion

I demonstrated that FPR1 on the plasma membrane of HEK293 cells was equilibrated between small and large oligomers (**Fig. 3-10B**), which were estimated to contain 2–4 and 5–11 FPR1, respectively (**Fig. 3-9D**). FPR1 clusters were only detected 5 min after ligand stimulation (**Fig. 3-2A**). The large oligomer fraction detected with the single molecule imaging were different from the clusters detected with the bulk TIRF microscopy because of their temporal pattern and lateral mobility. In previous single molecule reports, protein expression levels of GPCRs were kept low because single-molecule tracking was generally applicable to a spot density of less than 1 particle/μm^2. But, this experimental condition might result in potential limitation for the oligomer formation[39]. In this study, I expressed a physiological amount of FPR1 and reduced a spot density in the fluorescence images by lowering the fluorescence labeling efficiency of FPR1. This protocol enabled the single molecule analysis on physiologically-formed mesoscale FPR1 oligomers, such as tetramers and hexamers. My finding indicates substantial large oligomer formation of FPR1 both before and after ligand stimulation under the physiological expression level of FPR1.

The single molecule results demonstrated that FPR1 formed dimers, trimers, tetramers, and hexamer under basal condition (**Fig. 3-9**), and the bulk TIRF results demonstrated that the clusters contain eight times as many FPR1 as the other FPR1 complexes (**Fig. 3-2C**), suggesting that the clusters were estimated to contain 16–48 molecules of FPR1. The number of visible clusters varied among cells around 70 clusters on the bottom half of the cell membrane of each cell (**Figs. 3-2A, B**). Considering the typical FPR1 expression level of 6,000 copies in a cell[33], each cluster contained 42 molecules of FPR1 if I assumed that all the FPR1 participated in the cluster formation. These estimations consistently suggested that ligand stimulation triggered FPR1 clusters composed of a few tens of receptors.

Formation of the FPR1 oligomers and their interaction with signaling proteins were evaluated using single-molecule fluorescence imaging. Single molecule results showed that the full agonist stimulation enhanced the formation of the large FPR1 oligomers, and that the agonist treated FPR1 had a high affinity to G protein. I also revealed that the ligand-bound large FPR1 oligomers had a higher G protein affinity than either the ligand-bound small FPR1 oligomers or the ligand-free large FPR1 oligomers. From these results, I concluded that the large FPR1 oligomer formation was related to G protein signal transduction and the ligand-bound large FPR1 oligomers would serve as a potent activator of G protein. I propose a G protein activation model of FPR1 in living cells (**Fig. 3-14**). Without stimulation, FPR1 is in a dynamic equilibrium between the small and large oligomers, both of which transiently interact with G protein. After ligand binding, the oligomerization equilibrium shifted from the ligand-bound small FPR1 oligomers to the ligand-bound large FPR1 oligomers. The ligand-bound large FPR1 oligomers increased its affinity towards G protein potentially to transduce the signals. Importantly, the FPR1 oligomers were stochastically formed and disrupted, resulting in a heterogeneous distribution

of the FPR1 oligomers on the cell membrane. The transiently formed ligand-bound large FPR1 oligomers will induce a spatially heterogeneous activation of G protein. The present research is the first report to show the heterogenous distribution of oligomeric GPCRs and In previous reports, the signal transduction efficacy of particular GPCRs, such as α_{2A} adrenergic receptor, was increased by local entrapment of the GPCRs with G protein at membrane "hot spots" that were structured by the cytoskeleton[40]. Combining with my model, the results consistently suggests that G protein activation might be controlled more dynamically and heterogeneously by various membrane molecules and local GPCR large oligomer formations. Considering these findings together, I conclude that the signal transduction of FPR1 is induced strongly by the ligand binding and that it is regulated dynamically by the oligomer formation of FPR1.
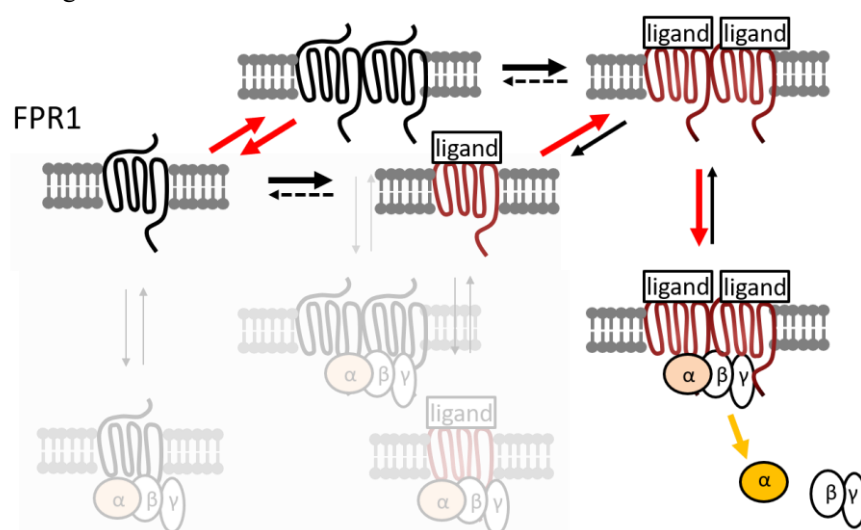

Fig. 3-14. Signal transduction mechanism revealed by triple-color single molecule imaging. FPR1 is in a dynamic equilibrium between small and large oligomers at any time. Ligand binding shifts the equilibrium towards the large oligomers, which have an increased affinity to G protein. This G protein high affinity state, ligand-bound large FPR1 oligomers, would be a potential activator of G protein signaling.

The fraction of large FPR1 oligomers increased from $65.9 \pm 1.7\% - 71.5 \pm 1.6\%$ upon the full agonist stimulation (**Fig. 3-10C**). The equilibrium shift was originated from the shifts in the association rate and/or dissociation rate. I estimated ligand-induced relative changes in the association rate under following two assumptions: (i) The equilibrium between the small and large oligomers is governed by a simple two-state interconversion following the equation: $K_{eq} = k_a/k_d = $ [Large oligomer]/[Small oligomer]^2, where K_{eq} denotes the equilibrium constant and where k_a and k_d represent the association and dissociation rates, respectively. (ii) The dissociation rate (k_d) is decreased by a factor of 0.66 by the full agonist, which is a typical ligand-induced change in the dissociation rate of GPCR dimers, such as D2 dopamine receptor dimers[15]. By substituting the measured values of the small oligomer

fractions (34.1%) and the large oligomer fractions (65.9%) for the equation of K_{eq} = [Large oligomer]/[Small oligomer]^2, the equilibrium constant of FPR1 oligomerization is calculated to K_{eq}(before) = 5.68 before ligand stimulation. After the full agonist treatment, the values of the large oligomer fraction (71.5%) and the small oligomer fraction (38.5%) gives K_{eq}(after) = 8.80. Because K_{eq} change of K_{eq}(after)/K_{eq}(before) = 1.55 and the given k_d change of k_d(after)/k_d(before) = 0.66, the relative change in the k_a values before and after the ligand stimulation, k_a(after)/k_a(before), is estimated to be 1.02. This absence of changes in the association rate suggests that the agonist-induced change in the association rate of small FPR1 oligomers is negligible in the small–large oligomer equilibrium shift. Therefore, the increase in the large oligomer fraction of FPR1 mostly originates from the decreased dissociation rate of the large oligomers, suggesting stabilization of the large FPR1 oligomers upon full agonist stimulation.

FPR1 exhibited a transient interaction with G protein with a time constant of approximately 50 ms. The full agonist prolonged the time constant by 14 ms on average (**Fig. 3-13E**). The agonist-induced change in the interaction duration suggests that the interaction duration is correlated with the magnitude of the downstream signal transductions such as the activation of G protein. The signal transduction mechanism of GPCRs towards G protein has remained controversial. Particularly the function of transient GPCR-G protein interactions has varied in different activation models such as a precoupled model and a random collision model[41]. In the precoupled model, GPCR-G protein interactions are already formed before ligand stimulation, and agonist stimulation immediately activates and liberates the precoupled G protein. By contrast, in the random collision model, a GPCR and G protein freely diffuse on cell membrane before ligand stimulation, amd the ligand binding to GPCR induces transient interaction and activation of G protein. In this study, the FPR1 transiently interact with G protein with the lifetime of 2–20 ms at any moment, and a large fraction of FPR1 and G protein was seeking for new binding partners even after ligand stimulation. The ligand bound FPR1 exhibited an increased affinity with G protein by a factor of 1.3 (**Fig. 3-13E**). These results suggest that both precoupled model and randam collision model hold true. Rapid interconversion of precoupling and random collision would provide a quite robust system for GPCR-G protein signal transduction system under a dynamic and noisy environment.

The signal control associated with the FPR1 oligomer formation might provide a novel concept for the development of new drugs with high specificities. Our present results suggest that G protein signals were mediated by the large FPR1 oligomerization whereas β-arrestin recruitment triggered the FPR1 cluster formation. Hence, the size of the FPR1 complexes might be strictly correlated with the downstream signal transductions when activated with the full (unbiased) ligand. This finding suggests that chemical compounds that induce or inhibit the oligomer formation may act as an allosteric modulator of GPCRs in signal transduction. Bivalent ligands containing two agonists with a chemical linker have been designed for some GPCRs, including melanocortin 4 receptor[42] and dopamine D2

receptor[43]. Both compounds exhibited an enhanced signal transduction efficacy for GPCRs by binding to homodimers of GPCRs. In contrast, dimer disrupting peptides designed by mimicking the transmembrane domains of GPCRs, such as secretin receptor, allosterically inhibited the GPCR activation[44]. More interestingly, reports have described that a pharmacologically biased orthosteric ligand increased the amount of β2 adrenergic receptor dimers in contrast to no dimerization trends with unbiased full ligands[14]. These reports support the possible control of GPCR signal efficacy by allosterically or orthosterically regulating the oligomer and cluster formations. The oligomerization-dependent signal control is attractive for cell-specific signal control because the oligomer formation of GPCRs are strongly dependent on cell types, including the expression level of GPCRs[10,16] and lipid compositions of cell membranes[45]. Taken together, evaluation of ligand-induced changes in the oligomer sizes of GPCRs will benefit new drug discovery to achieve high specificity.

3-5. Conclusion

I visualized the ligand-binding and oligomerization states of individual FPR1 in living cells to demonstrate the dynamic control of the signal transduction efficacy through the FPR1-G protein interaction (**Fig. 3-15**). Using the benefits of three-color single-molecule imaging, I categorized for the first time the four states of FPR1: ligand-bound small oligomers, ligand-bound large oligomers, ligand free small oligomers, and ligand free large oligomers. Of those different states, the ligand-bound large FPR1 oligomers exhibited the highest affinity with G protein, potentially inducing an efficient signal transduction. The results illustrate the importance of ligand-induced FPR1 oligomerization for signal transduction. In addition, I also visualized β-arrestin dependent cluster formation of FPR1 (**Fig. 3-15**). Its physical properties, such as the size, temporal pattern, and lateral mobility, were distinct from those of the large oligomers. Combining the result, the distinct binding behaviors with signal transducing proteins suggest that the signal transduction of FPR1 was correlated with the size of FPR1 complex. Therefore, the signal transduction patterns of FPR1 may be synergistically regulated by the ligand binding and FPR1 oligomer and cluster formation in living systems. Cooperative and dynamic activation of GPCRs is expected to be crucially important for the development of pharmacologically attractive biased ligands.
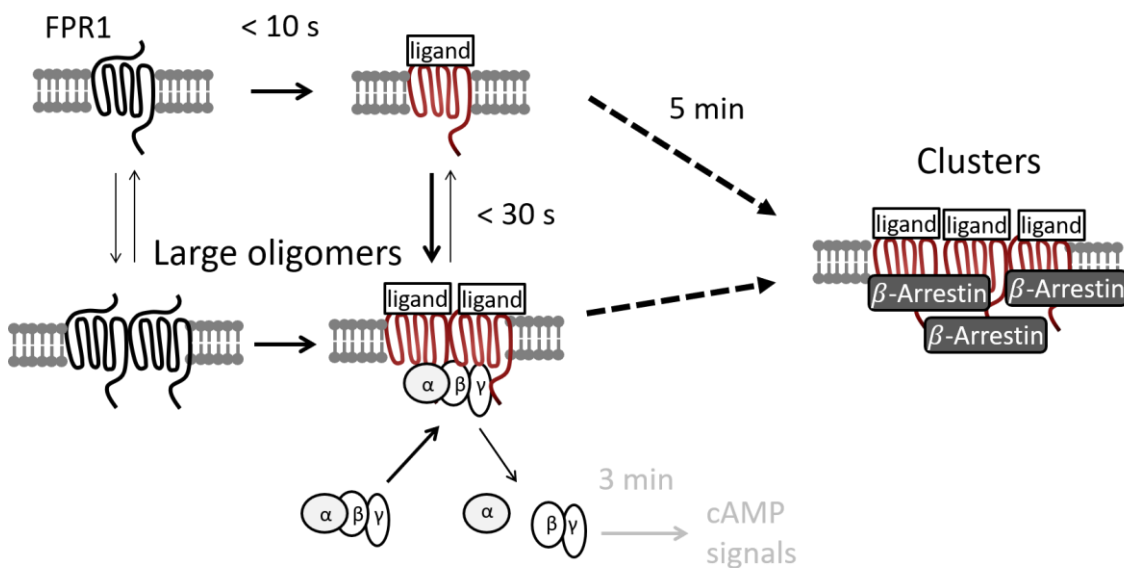

Fig. 3-15. Summary of the finding in the study. FPR1 formed large oligomers consist of 5–11 receptors in the early time point after ligand binding to induce G protein interactions. At the late time point, FPR1 formed clusters composed of 20–40 receptors dependent on the β-arrestin interactions. These results indicate that the signal transduction of FPR1 is synergistically regulated by ligand binding and oligomer or cluster formation.

3-6. References

(1)   Santini, F.; Gaidarov, I.; Keen, J. H. G Protein-Coupled Receptor/Arrestin3 Modulation of the
        Endocytic Machinery. *J. Cell Biol.* **2002**, *156* (4), 665–676.
        https://doi.org/10.1083/jcb.200110132.

(2)   Laporte, S. A.; Oakley, R. H.; Holt, J. A.; Barak, L. S.; Caron, M. G. The Interaction of Beta-
        Arrestin with the AP-2 Adaptor Is Required for the Clustering of Beta 2-Adrenergic Receptor into
        Clathrin-Coated Pits. *J. Biol. Chem.* **2000**, *275* (30), 23120–23126.
        https://doi.org/10.1074/jbc.M002581200.

(3)   Hayashi, F.; Saito, N.; Tanimoto, Y.; Okada, K.; Morigaki, K.; Seno, K.; Maekawa, S.
        Raftophilic Rhodopsin-Clusters Offer Stochastic Platforms for G Protein Signalling in Retinal
        Discs. *Commun. Biol.* **2019**, *2*, 209. https://doi.org/10.1038/s42003-019-0459-6.

(4)   Gripentrog, J. M.; Kantele, K. P.; Jesaitis, A. J.; Miettinen, H. M. Experimental Evidence for
        Lack of Homodimerization of the G Protein-Coupled Human N -Formyl Peptide Receptor. *J.
        Immunol.* **2003**, *171* (6), 3187–3193. https://doi.org/10.4049/jimmunol.171.6.3187.

(5)   Xue, M.; Vines, C. M.; Buranda, T.; Cimino, D. F.; Bennett, T. A.; Prossnitz, E. R. N-Formyl
        Peptide Receptors Cluster in an Active Raft-Associated State Prior to Phosphorylation. *J. Biol.
        Chem.* **2004**, *279* (43), 45175–45184. https://doi.org/10.1074/jbc.M407053200.

(6)   Cooray, S. N.; Gobbetti, T.; Montero-Melendez, T.; McArthur, S.; Thompson, D.; Clark, A. J. L.;
        Flower, R. J.; Perretti, M. Ligand-Specific Conformational Change of the G-Protein-Coupled
        Receptor ALX/FPR2 Determines Proresolving Functional Responses. *Proc. Natl. Acad. Sci. U. S.
        A.* **2013**, *110* (45), 18232–18237. https://doi.org/10.1073/pnas.1308253110.

(7)   Guo, H.; An, S.; Ward, R.; Yang, Y.; Liu, Y.; Guo, X.-X.; Hao, Q.; Xu, T.-R. Methods Used to
        Study the Oligomeric Structure of G-Protein-Coupled Receptors. *Biosci. Rep.* **2017**, *37* (2),
        BSR20160547. https://doi.org/10.1042/bsr20160547.

(8)   Ferre, S.; Casado, V.; Devi, L. A.; Filizola, M.; Jockers, R.; Lohse, M. J.; Milligan, G.; Pin, J.-P.;
        Guitart, X. G Protein-Coupled Receptor Oligomerization Revisited: Functional and
        Pharmacological Perspectives. *Pharmacol. Rev.* **2014**, *66* (2), 413–434.
        https://doi.org/10.1124/pr.113.008052.

(9)   Whorton, M. R.; Bokoch, M. P.; Rasmussen, S. G. F.; Huang, B.; Zare, R. N.; Kobilka, B.;
        Sunahara, R. K. A Monomeric G Protein-Coupled Receptor Isolated in a High-Density
        Lipoprotein Particle Efficiently Activates Its G Protein. *Proc. Natl. Acad. Sci.* **2007**, *104* (18),
        7682–7687.

(10)   Calebiro, D.; Rieken, F.; Wagner, J.; Sungkaworn, T.; Zabel, U.; Borzi, A.; Cocucci, E.; Zurn, A.;
        Lohse, M. J. Single-Molecule Analysis of Fluorescently Labeled G-Protein-Coupled Receptors
        Reveals Complexes with Distinct Dynamics and Organization. *Proc. Natl. Acad. Sci.* **2013**, *110*
        (2), 743–748. https://doi.org/10.1073/pnas.1205798110.

(11)   Navarro, G.; Cordomí, A.; Zelman-Femiak, M.; Brugarolas, M.; Moreno, E.; Aguinaga, D.; Perez-Benito, L.; Cortés, A.; Casadó, V.; Mallol, J.; et al. Quaternary Structure of a G-Protein-Coupled Receptor Heterotetramer in Complex with Gi and Gs. *BMC Biol.* **2016**, *14* (1), 26. https://doi.org/10.1186/s12915-016-0247-4.

(12)   Hern, J. A.; Baig, A. H.; Mashanov, G. I.; Birdsall, B.; Corrie, J. E. T.; Lazareno, S.; Molloy, J. E.; Birdsall, N. J. M. Formation and Dissociation of M1 Muscarinic Receptor Dimers Seen by Total Internal Reflection Fluorescence Imaging of Single Molecules. *Proc. Natl. Acad. Sci.* **2010**, *107* (6), 2693–2698. https://doi.org/10.1073/pnas.0907915107.

(13)   Kasai, R. S.; Suzuki, K. G. N.; Prossnitz, E. R.; Koyama-Honda, I.; Nakada, C.; Fujiwara, T. K.; Kusumi, A. Full Characterization of GPCR Monomer-Dimer Dynamic Equilibrium by Single Molecule Imaging. *J. Cell Biol.* **2011**, *192* (3), 463–480. https://doi.org/10.1083/jcb.201009128.

(14)   Sun, Y.; Li, N.; Zhang, M.; Zhou, W.; Yuan, J.; Zhao, R.; Wu, J.; Li, Z.; Zhang, Y.; Fang, X. Single-Molecule Imaging Reveals the Stoichiometry Change of B2-Adrenergic Receptors by a Pharmacological Biased Ligand. *Chem. Commun.* **2016**, *52* (44), 7086–7089. https://doi.org/10.1039/c6cc00628k.

(15)   Kasai, R. S.; Ito, S. V.; Awane, R. M.; Fujiwara, T. K.; Kusumi, A. The Class-A GPCR Dopamine D2 Receptor Forms Transient Dimers Stabilized by Agonists: Detection by Single-Molecule Tracking. *Cell Biochem. Biophys.* **2018**, *76* (1–2), 29–37. https://doi.org/10.1007/s12013-017-0829-y.

(16)   Tabor, A.; Weisenburger, S.; Banerjee, A.; Purkayastha, N.; Kaindl, J. M.; Hübner, H.; Wei, L.; Grömer, T. W.; Kornhuber, J.; Tschammer, N.; et al. Visualization and Ligand-Induced Modulation of Dopamine Receptor Dimerization at the Single Molecule Level. *Sci. Rep.* **2016**, *6* (June), 33233. https://doi.org/10.1038/srep33233.

(17)   Bunemann, M.; Frank, M.; Lohse, M. J. Gi Protein Activation in Intact Cells Involves Subunit Rearrangement Rather than Dissociation. *Proc. Natl. Acad. Sci.* **2003**, *100* (26), 16077–16082. https://doi.org/10.1073/pnas.2536719100.

(18)   Miyanaga, Y.; Kamimura, Y.; Kuwayama, H.; Devreotes, P. N.; Ueda, M. Chemoattractant Receptors Activate, Recruit and Capture G Proteins for Wide Range Chemotaxis. *Biochem. Biophys. Res. Commun.* **2018**, *507* (1–4), 304–310. https://doi.org/10.1016/j.bbrc.2018.11.029.

(19)   Wenzel-Seifert, K.; Arthur, J. M.; Liu, H. Y.; Seifert, R. Quantitative Analysis of Formyl Peptide Receptor Coupling to G(i)A1, G(i)A2, and G(i)A3. *J. Biol. Chem.* **1999**, *274* (47), 33259–33266. https://doi.org/10.1074/jbc.274.47.33259.

(20)   Atwood, B. K.; Lopez, J.; Wager-Miller, J.; Mackie, K.; Straiker, A. Expression of G Protein-Coupled Receptors and Related Proteins in HEK293, AtT20, BV2, and N18 Cell Lines as Revealed by Microarray Analysis. *BMC Genomics* **2011**, *12* (14), 14. https://doi.org/10.1186/1471-2164-12-14.

(21)   Yamada, T.; Yoshimura, H.; Shimada, R.; Hattori, M.; Eguchi, M.; Fujiwara, T. K.; Kusumi, A.; Ozawa, T. Spatiotemporal Analysis with a Genetically Encoded Fluorescent RNA Probe Reveals TERRA Function around Telomeres. *Sci. Rep.* **2016**, *6* (August), 38910. https://doi.org/10.1038/srep38910.

(22)   Waller, A.; Pipkorn, D.; Sutton, K. L.; Linderman, J. J.; Omann, G. M. Validation of Flow Cytometric Competitive Binding Protocols and Characterization of Fluorescently Labeled Ligands. *Cytometry* **2001**, *45* (2), 102–114. https://doi.org/10.1002/1097-0320(20011001)45:2<102::AID-CYTO1152>3.0.CO;2-Z.

(23)   Koyama-Honda, I.; Ritchie, K.; Fujiwara, T.; Iino, R.; Murakoshi, H.; Kasai, R. S.; Kusumi, A. Fluorescence Imaging for Monitoring the Colocalization of Two Single Molecules in Living Cells. *Biophys. J.* **2005**, *88* (3), 2126–2136. https://doi.org/10.1529/biophysj.104.048967.

(24)   Fujiwara, T.; Ritchie, K.; Murakoshi, H.; Jacobson, K.; Kusumi, A. Phospholipids Undergo Hop Diffusion in Compartmentalized Cell Membrane. *J. Cell Biol.* **2002**, *157* (6), 1071–1081. https://doi.org/10.1083/jcb.200202050.

(25)   Latty, S. L.; Felce, J. H.; Weimann, L.; Lee, S. F.; Davis, S. J.; Klenerman, D. Referenced Single-Molecule Measurements Differentiate between GPCR Oligomerization States. *Biophys. J.* **2015**, *109* (9), 1798–1806. https://doi.org/10.1016/j.bpj.2015.09.004.

(26)   Eichel, K.; Jullié, D.; Barsi-Rhyne, B.; Latorraca, N. R.; Masureel, M.; Sibarita, J.-B.; Dror, R. O.; von Zastrow, M. Catalytic Activation of β-Arrestin by GPCRs. *Nature* **2018**, *557* (7705), 381–386. https://doi.org/10.1038/s41586-018-0079-1.

(27)   Loitto, V. M.; Rasmusson, B.; Magnusson, K. E. Assessment of Neutrophil N-Formyl Peptide Receptors by Using Antibodies and Fluorescent Peptides. *J. Leukoc. Biol.* **2001**, *69* (5), 762–771.

(28)   Tan, X.; Luo, M.; Liu, A. P. Clathrin-Mediated Endocytosis Regulates FMLP-Mediated Neutrophil Polarization. *Heliyon* **2018**, *4* (9), e00819. https://doi.org/10.1016/j.heliyon.2018.e00819.

(29)   Subramanian, B. C.; Moissoglu, K.; Parent, C. A. The LTB(4)-BLT1 Axis Regulates the Polarized Trafficking of Chemoattractant GPCRs during Neutrophil Chemotaxis. *J. Cell Sci.* **2018**, *131* (18). https://doi.org/10.1242/jcs.217422.

(30)   Gilbert, T. L.; Bennett, T. A.; Maestas, D. C.; Cimino, D. F.; Prossnitz, E. R. Internalization of the Human N-Formyl Peptide and C5a Chemoattractant Receptors Occurs via Clathrin-Independent Mechanisms. *Biochemistry* **2001**, *40* (12), 3467–3475. https://doi.org/10.1021/bi001320y.

(31)   Wang, J.; Chen, M.; Li, S.; Ye, R. D. Targeted Delivery of a Ligand-Drug Conjugate via Formyl Peptide Receptor 1 through Cholesterol-Dependent Endocytosis. *Mol. Pharm.* **2019**, *16* (6), 2636–2647. https://doi.org/10.1021/acs.molpharmaceut.9b00188.

(32)   Sitrin, R. G.; Emery, S. L.; Sassanella, T. M.; Blackwood, R. A.; Petty, H. R. Selective

Localization of Recognition Complexes for Leukotriene B4 and Formyl-Met-Leu-Phe within Lipid Raft Microdomains of Human Polymorphonuclear Neutrophils. *J. Immunol.* **2006**, *177* (11), 8177–8184. https://doi.org/10.4049/jimmunol.177.11.8177.

(33) Tennenberg, S. D.; Zemlan, F. P.; Solomkin, J. S. Characterization of Receptors on Human Neutrophils . Effects of Isolation and Temperature on Receptor Expression and Functional Activity . *J. Immunol.* **1988**, *141* (11), 3937–3944.

(34) Sneha A Deshpande, Aiswarya B Pawar, Anish Dighe, Chaitanya A Athale, D. S. Role of Spatial Inhomogenity in GPCR Dimerisation Predicted by Receptor Association-Diffusion Models. *Phys. Biol.* **2017**, *14* (3), 036002.

(35) Rose, J. J.; Foley, J. F.; Yi, L.; Herren, G.; Venkatesan, S. Cholesterol Is Obligatory for Polarization and Chemotaxis but Not for Endocytosis and Associated Signaling from Chemoattractant Receptors in Human Neutrophils. *J. Biomed. Sci.* **2008**, *15* (4), 441–461. https://doi.org/10.1007/s11373-008-9239-x.

(36) Dahlgren, C.; Gabl, M.; Holdfeldt, A.; Winther, M.; Forsman, H. Basic Characteristics of the Neutrophil Receptors That Recognize Formylated Peptides, a Danger-Associated Molecular Pattern Generated by Bacteria and Mitochondria. *Biochem. Pharmacol.* **2016**, *114*, 22–39. https://doi.org/10.1016/j.bcp.2016.04.014.

(37) Bommakanti, R. K.; Bokoch, G. M.; Tolley, J. O.; Schreiber, R. E.; Siemsen, D. W.; Klotz, K. N.; Jesaitis, A. J. Reconstitution of a Physical Complex between the N-Formyl Chemotactic Peptide Receptor and G Protein. Inhibition by Pertussis Toxin-Catalyzed ADP Ribosylation. *J. Biol. Chem.* **1992**, *267* (11), 7576–7581.

(38) Hoffman, J. F.; Linderman, J. J.; Omann, G. M. Receptor Up-Regulation, Internalization, and Interconverting Receptor States. *J. Biol. Chem.* **1996**, *271* (31), 18394–18404. https://doi.org/10.1074/jbc.271.31.18394.

(39) Gurevich, V. V.; Gurevich, E. V. GPCRs and Signal Transducers: Interaction Stoichiometry. *Trends Pharmacol. Sci.* **2018**, *39* (7), 672–684. https://doi.org/10.1016/j.tips.2018.04.002.

(40) Sungkaworn, T.; Jobin, M. L.; Burnecki, K.; Weron, A.; Lohse, M. J.; Calebiro, D. Single-Molecule Imaging Reveals Receptor-G Protein Interactions at Cell Surface Hot Spots. *Nature* **2017**, *550* (7677), 543–547. https://doi.org/10.1038/nature24264.

(41) Bondar, A.; Lazar, J. The G Protein Gi1 Exhibits Basal Coupling but Not Preassembly with G Protein-Coupled Receptors. *J. Biol. Chem.* **2017**, *292* (23), 9690–9698. https://doi.org/10.1074/jbc.M116.768127.

(42) Lensing, C. J.; Freeman, K. T.; Schnell, S. M.; Adank, D. N.; Speth, R. C.; Haskell-Luevano, C. An in Vitro and in Vivo Investigation of Bivalent Ligands That Display Preferential Binding and Functional Activity for Different Melanocortin Receptor Homodimers. *J. Med. Chem.* **2016**, *59* (7), 3112–3128. https://doi.org/10.1021/acs.jmedchem.5b01894.

(43)   Pulido, D.; Casadó-Anguera, V.; Pérez-Benito, L.; Moreno, E.; Cordomí, A.; López, L.; Cortés, A.; Ferré, S.; Pardo, L.; Casadó, V.; et al. Design of a True Bivalent Ligand with Picomolar Binding Affinity for a G Protein-Coupled Receptor Homodimer. *J. Med. Chem.* **2018**, *61* (20), 9335–9346. https://doi.org/10.1021/acs.jmedchem.8b01249.

(44)   Harikumar, K. G.; Pinon, D. I.; Miller, L. J. Transmembrane Segment IV Contributes a Functionally Important Interface for Oligomerization of the Class II G Protein-Coupled Secretin Receptor. *J. Biol. Chem.* **2007**, *282* (42), 30363–30372. https://doi.org/10.1074/jbc.M702325200.

(45)   Fallahi-Sichani, M.; Linderman, J. J. Lipid Raft-Mediated Regulation of G-Protein Coupled Receptor Signaling by Ligands Which Influence Receptor Dimerization: A Computational Study. *PLoS One* **2009**, *4* (8), e6604. https://doi.org/10.1371/journal.pone.0006604.

Chapter 4

General Conclusion

GPCRs are involved in a wide range of diseases. Growing evidence has suggested the pluridimensional signal controls of GPCRs by many factors, including ligand-induced unique structural changes and transient GPCR-GPCR interactions. However, temporally dynamic changes in signal transductions of GPCRs have not been fully investigated for drug discovery.

In Chapter 2, I established four assay systems to measure the signal transduction efficiency quantitatively with temporal information. In the conventional drug discovery, the efficacy of signal transduction has been evaluated mainly by ligand binding and second messengers only at a fixed time point. The present study added two assay systems to monitor directly the G protein activation and the β-arrestin recruitment to evaluate ligand bias. All the assays were designed to be performed in the same cell type and under the same temperature, enabling the unbiased measurements of the efficiency and the kinetics of signal transduction events. At the equilibrated states, an FPR1 agonist, fMLP, displayed different dose–response curves among signal transduction events, suggesting an originally biased signal transduction of FPR1. In addition, I monitored the temporal changes in the dose–response of β-arrestin recruitment. The effective concentrations of the agonist for β-arrestin recruitment were decreased over time, suggesting that relative signal strengths among signal pathways might change dependent on the time point after ligand stimulation. Therefore, the present results demonstrated the importance of measuring the ligand bias with the temporal information.

In Chapter 3, I visualized oligomer formations of FPR1 in living cells and revealed its roles in signal transduction. The cluster formation of FPR1 has been widely accepted due to the relatively large size of the clusters, being visible under conventional microscopy. Recent studies have investigated the 3D structures of GPCRs using cryo-EM and the monomer–dimer equilibrium of FPR1 using single molecule microscopy, but the presence and the roles of FPR1 oligomers with intermediate sizes have not been elucidated. In the present study, by controlling the labeling efficiency of FPR1, both the clusters and oligomers have been detected in the cells with the same expression levels of FPR1. I demonstrated that FPR1 on the plasma membrane of HEK293 cells was equilibrated between small oligomers (2–4 FPR1) and large oligomers (5–11 FPR1) at the physiological expression level of 2 molecules/μm^2. The agonist stimulation induced the equilibrium shift toward the large oligomers to induce G protein binding within 2 min, and induced FPR1 cluster formation (20–40 FPR1) triggered by β-arrestin recruitment in 5 min. The temporally dynamic complex formation of FPR1 would provide a robust signal transduction under noisy physiological conditions. The oligomerization-induced signal transduction may be a novel target for signal specific drug discovery.

I established ligand binding assay, β-arrestin split luciferase assay, bioluminescence cAMP assay, and G protein FRET assay system for quantitative evaluation of signaling patterns of FPR1 in living HEK293 cells. Using single molecule and ensemble TIRF imaging, I clarified the size distributions of FPR1 and their roles in signal transductions under the physiological expression level. The presently

established methods enable the detection of signal biases and provide a deep insight into the effects on dynamic signal control mediated by FPR1 oligomer formation in living systems.

Acknowledgments